AUTOMATED DESIGN OF COMPOSITE PLATES FOR IMPROVED DAMAGE
TOLERANCE

by

Zafer Gürdal

Dissertation submitted to the Faculty of the

Virginia Polytechnic Institute and State University

in partial fulfillment of the requirements for the degree of

DOCTOR OF PHILOSOPHY

in

Aerospace Engineering

APPROVED:

_____
Raphael T. Haftka

_____   _____
William L. Hallauer   Eric R. Johnson

_____   _____
Robert M. Jones   Henry J. Kelley

January, 1985
Blacksburg, Virginia

ACKNOWLEDGEMENTS

NOMENCLATURE

a   half crack length

a_{ij} coefficients of laminate compliance matrix

b   stiffener blade width

c   half thickness of matrix between adjacent fibers

d   stiffener flange width

e   stiffener spacing

g   a typical constraint

g_{SIF} stress intensity factor constraint

g_σ lamina stress constraint

h   fiber thickness

k_1, k_2 defined in Eqs. (15), and (17) respectively

ℓ fiber length for the microbuckling model

q   ratio of the fiber shear force to the fiber axial load

r   radial distance ahead of the crack tip

s   load scaling factor

s_i complex roots of the characteristic equation, Eq. (11)

t_b stiffener blade height

t_f stiffener flange thickness

t_p panel section thickness

u   longitudinal end displacement under loading

v   transverse fiber displacement

w   plate out-of-plane deflection

x   longitudinal coordinate axis

y	transverse coordinate axis
A	cross sectional area of the plate
E_f	fiber Young's modulus
E_m	matrix Young's modulus
E_x	laminate longitudinal modulus
E_y	laminate transverse modulus
G_m	matrix shear modulus
G_{xy}	laminate shear modulus
I	unit boundary displacement vector
I_f	fiber area moment of inertia
K_I	crack opening mode stress intensity factor
K_{II}	in-plane shearing mode stress intensity factor
$\left. \begin{array}{c} K_{aa} \\ K_{ad} \\ K_{dd} \end{array} \right\}$	submatrices of the partitioned form of the stiffness matrix
K_c	critical value of the opening mode stress intensity factor
L	plate length
P	applied longitudinal load
P_f	axial force on the fiber for microbuckling model
$P_{f,C}$	critical fiber load
P_{CR}	buckling load of plate
P_I	load achieved under unit displacement at the boundary
Q_c	general fracture toughness parameter
R_I	force vector under unit boundary displacement condition
S_f	shearing force on the fiber

$[T]$	transformation matrix, Eq. (3)
U	vector of nodal displacements under actual loading
U_I	vector of nodal displacements under unit boundary displ.
V_f	fiber volume fraction
W	total plate width
W_g	total plate weight
X	vector of design variables
X_L, X_U	vector of lower and upper bounds on design variables
Z	adjoint variable vector
Z_i	-see Eqs. (10)
α	orientation of the principal load carrying ply
$[\beta]$	matrix of constitutive properties, Eq. (2)
$\left.\begin{array}{c}\varepsilon_1 \\ \varepsilon_2 \\ \gamma_{12}\end{array}\right\}$	engineering strains in the principal material directions
ε_{utf}	ultimate tensile strain of fibers
ε_x	far field failure strain
ε_{CR}	local strain at buckling
θ	orientation of the plies from the x axis
ν_{xy}	laminate Poisson's ratio
σ	normal stress
σ_f	fiber axial stress
$\sigma_{f,max}$	maximum fiber stress under bending and compression
$\sigma_{f,C}$	critical fiber stress

$$\left.\begin{array}{c} \sigma_x \\ \sigma_y \\ \tau_{xy} \end{array}\right\} \quad \text{crack tip stresses}$$

τ shear stress

ψ rotational coordinate at the crack tip

Λ adjoint variable vector, Eq. (33)

$(\ )'$ $d(\ )/dx$

TABLE OF CONTENTS

LIST OF TABLES

LIST OF FIGURES

Chapter I

INTRODUCTION

Laminated composite materials are recognized as an attractive replacement for metallic materials for aeronautical applications because of their high strength-to-weight and stiffness-to-weight ratios. If composite materials are to be used in aircraft structural components, they must be designed to satisfy several structural requirements. For example, fuselage and skin panels must be designed to include geometric discontinuities in the form of cutouts (cabin windows, doors, access holes, etc.), and certain provisions must be made for sufficient damage tolerance (see, for example, Refs. [1,2]).

Damage tolerance is actually one of the most important performance constraints that must be considered in the design of modern aircraft. Airworthiness regulations require that catastrophic structural failure due to damage must be avoided throughout the operational life of an airplane. One form of damage which is a serious threat for survivability of metallic aircraft structures is cracks. Cracks often initiate from material defects or existing holes and cutouts under cyclic loadings. Advanced fibrous composite materials, which are prime candidates for aircraft

applications, exhibit good fatigue properties and have been shown to be resistant to fatigue crack growth. However, they present other problem areas that are not common to conventional materials. Experimental studies have shown that holes and cutouts can cause a severe reduction in tensile strength of composites. The lack of ductile behavior of composites at the points of high strain concentrations around cutouts results in localized failures. Unlike metals, composites have also been shown to be extremely notch sensitive under compressive loadings. Manufacturing defects and accidental damage during maintenance are also problem areas that can degrade the performance of the structure. Low-velocity impacts such as tool drops or runway debris have been shown to result in serious damage in composites [3,4], and degrade both compression and tension strength of a composite plate. In contrast, in homogeneous metallic plates no strength reduction occur due to such effects.

1.1 DESIGNING FOR DAMAGE TOLERANCE

Damage tolerance can be studied at two levels, global and local damage tolerance. Global damage tolerance implies that catastrophic failure or excessive structural deformations are not probable after partial or total failure

of a single principal structural component. Examples of the global approach are Refs. [5-7] in which structures are designed to be capable of carrying redistributed loads following failure of a single component or multiple components. Local damage tolerance, on the other hand, implies that the structural component can carry the design loads in the presence of local failures such as cracks that may develop during the service life of the component. The present study is concerned with design for local damage tolerance of composite plates.

Early work on structures tolerant to local damage was on metallic panels with cracks. For example, the design philosophy for a fuselage shell with crack-stopping straps was considered in Ref. [8]. Developments in cracked structure analytical methodology resulted in rigorous damage tolerance design procedures for metallic structures. Linear elastic fracture mechanics has been judged to be a useful tool in predicting residual strength and crack growth behavior of damaged metal aircraft panels [9], and several researchers have incorporated it into the design of minimum weight, damage tolerant stiffened panels.

Design charts developed for stress intensity factors for panels with riveted stiffeners [10] were used, for example, by Kruse [11] to perform detail design of box beam

structures. A nonlinear programming technique was used for finding efficient panel designs with various stiffener geometries under multiple constraints including fatigue life and static strength. Similarly, Davis [12] designed integrally stiffened two-panel box beams by using available analytical solutions. An optimality criteria method was used by Dobbs and Nelson [13] for designing cracked metal panels for which analytical solutions for stress intensity factors are not available. Strain energy release rates, obtained by a finite element analysis, were used to obtain the stress intensity factors. An analytical approach was used for response gradient calculations.

1.2 DAMAGE TOLERANCE AND COMPOSITES

In contrast to metal plates where local damage can successfully be represented by cracks, damage definition for composite materials is complicated. The number of possible modes of local failure is large, and they are usually micromechanically governed and complex. Fiber breaking, matrix cracking, fiber matrix debonding, and separation of individual layers can result in cracks, splits and delamination that can degrade the load-carrying capacity of a composite plate. Microbuckling and shear failures are also common types of failures under compressive loadings. A

local damage condition may be due to accumulation of these failures, and the final failure may be governed by several of them. Furthermore, the response of the plate can be different to the above local damage conditions depending on the physical properties of each constituent (fiber and matrix properties) in a lamina and depending on the layup (i.e., orientation and stacking sequence of the laminae) of the laminate.

The complexity of the problem also offers a variety of research areas. Damage tolerance concepts that can be pursued, for example, against impact damage are categorized under two main approaches [14]. The first approach, called the materials approach, is aimed at understanding the damage mechanism and improving the material response to achieve damage tolerance. For example, using graphite fabric material instead of unidirectional tape material improved the impact damage behavior through mechanical linking of the cross plies and reduced the delaminations. Similarly, transverse reinforcement in the form of through-the-thickness stitching suppresses delaminations and causes the plate to fail in a higher energy failure mode. It is also found that impact damage tolerance can be improved by matrix material modifications. For example, the use of higher fracture energy matrix material leads to a better response to impact damage.

The second approach, which is widely used for early metallic plate designs, is to achieve efficient structural configurations which are capable of arresting or limiting the growth of local damage and redistributing the applied loads. Structural configurations considered in Ref. [14] are shown in Fig. 1. Mechanically fastened plate configurations, see Fig. 1-a, proved to be effective in containing the damage in a controlled region and redistributing the loads, but with a penalty of increased weight, and cost of fabrication and assembly. The concept of arresting compression failure by introducing discontinuities in the form of bonded plate sections as shown in Fig. 1-b was partially effective to contain delaminations. However, this configuration failed to prevent the damage propagation by transverse shear failure mode which caused crippling of the load carrying $0°$ plies.

One of the promising structural concepts that are considered in Ref. [14] is to isolate the portions of the plate to high and low axial stiffness regions, see Fig. 1-c. Preliminary experimental investigations cited in Ref. [14] indicated that the low stiffness regions of the plates are tolerant to impact damages. It has also been shown that in some cases low stiffness regions are capable of arresting the damage propagation due to impact inflicted

on the high stiffness region. Although the idea is somewhat different, similar geometries obtained by using buffer strips have been shown to arrest and increase the residual strength of plates with cracks under tension loadings [15]. The buffer strips in Ref. [15] are made by interrupting and replacing strips of certain plies in the laminate by another material or layup.

1.3   SCOPE OF THIS INVESTIGATION

The nature of most of the design approaches mentioned in the previous section are experimental (except for a limited application of analysis techniques in case of tension loaded plates). A more rational approach to design requires sound analysis techniques which can be applied under both tensile and compressive loadings. However, the definition of a single damage condition that can be used under both compressive and tensile loading is difficult, and at present there is no single criterion for the failure of composites to account for all different damage conditions. Therefore, as a first step in an effort to automate the design process, the present work is limited to only one aspect of failure, simulating the local damage condition by a central through-the-thickness crack. Failure is characterized by the propagation of the crack with fiber failures under loading.

Through-the-thickness cracks are not a common type of damage in fibrous composite materials. Nevertheless, cracks are often used to estimate the residual strength of damaged structures [16]. Designing for crack damage can provide useful information because aircraft composite structures usually contain notches and holes. Common experience with composites indicates that holes have the same effects as equal size cracks. Moreover, a method frequently applied to the analysis of cracked composite components, namely linear elastic fracture mechanics is found to be useful to simulate impact damage [17-20] and may be used for designing for such a damage condition.

The next two chapters are devoted to establishing a failure criterion that can be used in an automated design procedure. Because of the significant differences in failure modes, the tension and compression cases are treated in separate chapters. Failure of plates with a central crack under tensile loading is considered first, because of a substantial body of previous research in that area. Seeking a failure criterion for cracked plates under compression, on the other hand, presents difficulties due to the paucity of both experimental and analytical information. The first part of Chapter 3 describes an experimental work intended to provide better understanding

of compressive behavior of composite plates with simulated cracks. In the second part of the chapter, the literature is reviewed and an analytical failure criterion is formulated that can be used for cracked plates under compression.

An automated design procedure requires the integration of an analysis procedure with an optimizer. In the present work, analyses of cracked plates are performed with a finite element program. The first section of Chapter 4 describes the crack finite element program. Integration of the finite element program with the optimizer requires automatic mesh generation which is the subject of the second section. The formulation of the design problem and the optimization package is explained in the third section. The efficiency of the design optimization is enhanced by using analytical sensitivity derivatives which are derived in the last section of the chapter.

The design procedure is demonstrated in chapter 5. Various examples are presented for both compression and tension loaded unstiffened and stiffened plates for the purpose of gaining insight into the process of designing with damage tolerance constraints.

Chapter II

FAILURE CRITERION FOR CRACKED PLATES IN TENSION

2.1   REVIEW OF LITERATURE

Even though the damage condition is simplified by
assuming that a through the thickness crack represents the
damage, the direct application of available tools, such as
linear elastic fracture mechanics, to the analyses of
cracked structural plates made of composites is limited.
The two main factors that contribute to the limited use are
the anisotropy and inhomogeneity of composites.

For certain configurations of a crack in a
unidirectional composite material, it was experimentally
shown by Wu [21] that the effect of anisotropy can be
eliminated and the fracture problem can be treated by the
theory of classical fracture mechanics for isotropic
materials. Waddoups et al. [22] extended the application to
notched laminated composites using a material model which is
macroscopically homogeneous but anisotropic. They
incorporated the effect of the plastic zone at the crack tip
into a fracture toughness model and predicted the notch size
dependence of failure strength.

Whitney and Nuismer [23] did not use fracture
mechanics, but developed their well-known point-stress and

average-stress criteria. The point-stress criterion stipulates failure when the stress at some distance away from the notch exceeds the strength of the unnotched laminate. The average-stress criterion, on the other hand, predicts failure when the average stress over some distance ahead of the notch equals the unnotched laminate strength. Good correlation of the flaw-size dependence of the laminate strength with experimental values was observed for both criteria.

The direct use of the point-stress and average-stress criteria in a design process is, however, limited. In order to use the point-stress criterion one needs the values of two independent parameters, namely the ultimate strength of the material and the value of the distance ahead of the notch where the stress level is compared with the ultimate strength of the unnotched laminate. Two approaches are used in the literature. The first one is to consider the distance ahead of the notch as a material constant while varying the material strength with the laminate layup, Ref. [23]. The second approach is to vary the distance ahead of the notch and hold the ultimate strain of the material constant. Whichever approach is used, the designer faces the problem of determining a variable parameter as the layup of his laminate changes during the design process.

The material modeling approach was developed by Zweben [24] and Rosen et al. [25], where the region around the notch tip was characterized by discrete regions of different behavior. The advantage of their model was the capability of predicting damage for more than one failure mechanism. Local stress distributions on individual fibers were considered by Hedgepeth and Van Dyke [26] in a microscopic approach. Fracture was assumed to be controlled by fiber stresses and fiber fracture. In-depth reviews of various approaches and their ranges of applicability are given in Refs. [27-30].

In the present work, a model that uses an extension of linear elastic fracture mechanics to composites under tensile loads is utilized [31,32]. The stress field around the crack tip, based on fracture mechanics, was used by Poe [31] together with classical lamination theory to obtain strains in the principal load-carrying ply. Fiber strains at failure were then correlated with experimental results, and the fracture toughness of a laminate was related to a basic fiber property and layup of the laminate.

The two key phases of the application of the Poe's [32] criterion are the calculation of the stress intensity factor (SIF) which indicates the distribution of the stress field around the crack tip, and the critical value of the SIF

which is the resistance of a material to crack growth. A linear finite element code [33], which utilizes a special anisotropic crack-tip element, is used to determine the stress intensity level in a tension loaded panel containing a crack. The details of the code are given in Chapter 4. The procedure for the evaluation of the fracture toughness [31] is presented in the next section.

2.2   FRACTURE TOUGHNESS

The measure of fracture toughness of composite laminates used in the present work is the maximum allowable value of the SIF (SIF is defined for the laminate by assuming the material to be homogeneous and anisotropic). The fracture toughness of a composite laminate is a strong function of the layup [29]. For a laminate with a given layup, it is possible to determine the fracture toughness experimentally for a given crack length, and use it for the design of panels with different allowable crack lengths. However, the design of a minimum weight panel with ply thickness design variables requires the consideration of panels with many different layups, and testing to determine the fracture toughness of each layup would be prohibitively expensive.

A recent analytical procedure developed by Poe and Sova [31,32] was employed to overcome the above difficulty. Experimental observations [31] showed that, for specimens with slits, tensile failure of fibers ahead of the slits is responsible for the final fracture. Furthermore, fiber failures occur mostly in 0° plies for laminates with both 0° and ±45° plies. A radiograph of the slit tip area is shown in Fig. 2 under two load levels for a Boron-Epoxy laminate tested in Ref. [31]. Broken 0° fibers are indicated by black circles. It is clear from the figure that just prior to the failure there is an increase in the number of fiber failures ahead of the crack tip collinear with the crack. In laminates with both 0° and ±45° plies the 0° plies carry more of the applied longitudinal load per ply than the ±45° plies, and hence are referred to as the principal load-carrying plies. For laminates with only ±45° plies, the number of broken fibers ahead of the slit ends was as large as the number of broken 0° fibers in laminates with 0° and ±45° plies. For any angle-ply laminates, the ±θ° plies with the smallest angle would be the principal load-carrying plies, and would sustain most of the broken fibers. It was concluded, therefore, that the laminates with a crack-like slit fail near the ends of the slit when the principal load-carrying plies reach their ultimate strain.

It is possible to get strains in the principal material directions for each ply by using the linear elastic fracture mechanics approach together with classical lamination theory. From Ref. [31], the engineering strains in the principal material directions for the ith ply of a symmetric laminate along the y axis ($\psi=0$ in Fig. 3) are

$$\begin{Bmatrix} \varepsilon_1 \\ \varepsilon_2 \\ \gamma_{12} \end{Bmatrix}_i = \frac{K_I}{\sqrt{2\pi r}} [T]_i [\beta] \begin{Bmatrix} 1 \\ \sqrt{E_y/E_x} \\ 0 \end{Bmatrix} \tag{1}$$

where K_I is the mode 1 stress-intensity factor, E_x and E_y are the laminate elastic moduli in the x and y directions, and r is the distance ahead of the crack tip. The matrix $[\beta]$ is the matrix of constitutive properties for the laminate

$$[\beta] = \begin{bmatrix} 1/E_x & -\nu_{xy}/E_x & 0 \\ -\nu_{xy}/E_x & 1/E_y & 0 \\ 0 & 0 & 1/G_{xy} \end{bmatrix} \tag{2}$$

with G_{xy} and ν_{xy} being the laminate shear modulus and Poisson's ratio respectively, and the matrix $[T]_i$ is the transformation matrix for the ith ply given by

$$[T]_i = \begin{bmatrix} \cos^2\alpha & \sin^2\alpha & \sin2\alpha \\ \sin^2\alpha & \cos^2\alpha & -\sin2\alpha \\ -1/2 \sin2\alpha & 1/2 \sin2\alpha & \cos2\alpha \end{bmatrix} \tag{3}$$

where α is the fiber orientation angle from the x-direction
(Fig. 3). Using the expressions for the two matrices, the
longitudinal fiber strain for the ith ply can be written as

$$\varepsilon_{1(i)} = \frac{K_I}{\sqrt{2\pi r}E_x}[1-\nu_{xy}\sqrt{E_y/E_x}\,]\,[\cos^2\alpha +\sqrt{E_x/E_y}\,\sin^2\alpha] \qquad (4)$$

With the stated assumption that the laminate fails when the
fiber strains in the principal load-carrying plies reach
their critical value, it was argued by Poe that $\varepsilon_1\sqrt{2\pi r}$ is a
constant at failure. This constant was called the general
fracture toughness parameter and denoted by Q_c.

The value of Q_c was verified to be a material constant
in Ref. [31] for boron/aluminum composite specimens with a
centrally located slot, regardless of ply orientation. The
same approach was extended to specimens made from
graphite/epoxy, boron/epoxy, E-glass/epoxy, S-glass-
graphite/epoxy, and graphite/polyimide materials with
various $[0_i/\pm45_j/90_k]$ layups in Ref. [32]. It was further
verified that the values of Q_c/ε_{utf}, where ε_{utf} is the
ultimate tensile strain of the fibers, was reasonably
constant and equal to 1.5 $\sqrt{mm}$ for all layups made with
different materials except for those that delaminated or
split extensively in the 0° plies at the crack tips.

The critical value of the SIF, K_c, is proportional to
Q_c and can be calculated from Eq. (4). The constant of

proportionality depends only on the elastic constants of the laminate and the orientation of the principal load-carrying fibers. Hence, once the value of Q_c is known for a given material, it is possible to predict the critical value of the SIF for any layup of that material. Material properties representative of graphite/epoxy are used throughout the present work and a value of 0.015 $\sqrt{mm}$ (corresponding to $\varepsilon_{utf}=0.01$) is used for Q_c.

Chapter III

FAILURE CRITERION FOR CRACKED PLATES IN COMPRESSION

3.1 EXPERIMENTAL WORK

The failure of center-notched composite plates under
tensile loadings has been the focus of many experimental
investigations. The effects of different material and
geometry parameters on the failure loads and modes are
generally well understood. Recent experimental
investigations have also concentrated on the compressive
strength of notched plates. For thick, strength-critical
plates, experimental studies have shown that impact damage,
delaminations, machined cracks and cutouts can cause a
severe reduction in the compressive load carrying capacity
of the plates (see, for example Refs. [3,4 and 34-36]).

Unlike plates under tensile loading which deform in the
plane of the plate, compressive loads can cause a plate to
buckle and result in significant out-of-plane deformations
depending on the plate thickness, geometry and boundary
conditions. Following a common design practice of using
metal aircraft plates in the postbuckling range, some
researchers have been interested in the postbuckling
behavior of composite plates. Early analytical work (e.g.,

Refs. [37-43]), followed by experimental investigations
(e.g., Refs. [44-46]) have shown substantial postbuckling
strength for compression loaded graphite/epoxy plates.

The influence of circular holes on the postbuckling
response of flat rectangular graphite/epoxy plates was
investigated in Ref. [45]. It was found that circular holes
located along the longitudinal centerline of a plate do not
have a significant effect on the postbuckling response of
the plate. No experimental work is available, however, for
the effect of notches, as opposed to holes, on the
postbuckling performance of composite plates. Stress
concentrations introduced by notches are far stronger than
those introduced by holes and may interact with the out-of-
plane deformations of the plate to alter the failure mode
and cause early failure.

The purpose of the present experimental investigation
is to find the effect of notches or simulated through-cracks
on the buckling and postbuckling behavior of unstiffened
composite plates.

3.1.1 Test Specimens and Apparatus

Nine test specimens, similar to those studied in a
previous experimental study [45], were used in the present
investigation. Five of the nine specimens were 16-ply

quasi-isotropic laminates with a $[\pm45/0/90]_{2S}$ stacking sequence, and the remaining four were 24-ply quasi-isotropic laminates with a $[\pm45/0/90]_{3S}$ stacking sequence. All specimens were 50.8 cm long and 22.9 cm wide except for three of the 16-ply laminates which were 10.2 cm wide. Average thicknesses for the 24-ply and 16-ply laminates were 0.32 cm and 0.20 cm, respectively.

Six pairs of back-to-back strain gages were used to monitor longitudinal strains for each specimen. Direct current differential transformers were used to monitor longitudinal end-shortening and out-of-plane deflections at different locations on the specimens. Out-of-plane deformation patterns, monitored by the moire-fringe technique, were recorded photographically. All electrical measurements obtained from the tests were recorded on magnetic tape.

All tests were performed with a 1.33-MN hydraulic testing machine at NASA Langley Research Center, Structural Mechanics Branch. The unloaded edges of the specimens were simply supported by knife-edge restraints, and the loaded ends were clamped. A typical test specimen mounted in the support fixture is shown in Fig. 4.

A lateral slot approximately 0.04 cm wide and either 2.5 cm or 5.1 cm long was machined into each of the nine

plates at different locations (see Fig. 5). Results of Ref [45] for plates without cutouts and without impact damage indicate that failure occurs along a nodal line of the buckling mode. Therefore, slots were machined close to an expected nodal line in seven of the test specimens to determine their effect on failure loads. For the remaining two specimens, slots were located close to a point of maximum out-of-plane deflection to determine if a high level of bending stresses would affect the mode of failure.

The result of the impact-damage experiments [45] suggested that the lateral location of slots may affect the postbuckling strength. Consequently, the slots were centrally located for five of the test specimens (C1 through C5), and were offset with respect to the longitudinal center line for the remaining four specimens (S1 through S4). The offset slots were located in regions of high postbuckling strains which were expected to affect the failure.

3.1.2 Results and Discussion

3.1.2.1 Prebuckling and Buckling Response

The prebuckling responses of most of the plates with slots were similar to the prebuckling responses of the unslotted specimens of Ref. [45]. The initial buckling loads and the number of longitudinal halfwaves of the

buckling mode are presented in Table 1 for each plate. The measured failure loads are also included in the Table as well as corresponding results from Ref. [45]. Comparison of buckling loads in Table 1 with the corresponding analytical buckling loads of the control specimens of Ref. [45][+] indicates that there is almost no effect of the slot on the buckling load of the plates. However, local deformations caused by the slots affected the buckling mode shapes.

End-shortening results for the 24- and 16-ply plates are shown in Figs. 6 and 7, respectively, as a function of the applied compressive load. The end-shortening deflections, u, are normalized by the plate length, L. The applied loads, P, are normalized by the product $E_x A$ where A is the cross sectional area, and E_x is the laminate longitudinal modulus for specimens without slots given in Ref. [45]. End-shortening response of control specimens, obtained from Ref. [45], are also included in Figs. 6 and 7 (as solid lines) for each plate type. The failure load of each plate is indicated by a symbol on the appropriate curve.

[+] Experimental buckling loads were not reported in Ref. [45]; The reported analytical results are consistent with the stiffness changes shown on the load-deflection curves.

Longitudinal stiffness change. The prebuckling slopes for all specimens with slots, as shown in Figs. 6 and 7, are observed to be slightly smaller than the corresponding prebuckling slopes of the control specimens. This difference reflects a slight reduction in the axial stiffness of the slotted plates compared to the unslotted specimens. Calculated slopes for a representative 24-ply plate and a 16-ply plate, specimens S1 and S3, respectively, are also included in Figs. 6 and 7. A linear finite element program [33] for analyzing cracked orthotropic plates was used for the prebuckling stiffness calculations. Calculated slopes agree well with the corresponding experimental values. However, for specimens C3 and C4, the slopes of prebuckling paths are about 15% smaller than the calculated values.

Strain distribution. The strain versus load curves, in all cases, were similar to those obtained in Ref. [45] except for strain gages either located close to the slot or located close to the line collinear with the slot. For example, the strain gage located at the center of specimen S3, close to the line collinear with the slot, indicated higher strains than the control specimen. The strain gage located just below the slot indicated a lower strain compared to the control specimen.

3.1.2.2   Postbuckling Response

Comparison of the postbuckling end-shortening results for plates with slots and for the control specimens indicates no major differences in response up to failure (see Figs. 6 and 7). But, some effects of the slots on the local strains, deformations, and failure loads were observed.

Postbuckling strains and deformations. The average strains obtained from back-to-back strain gages located at the center of the plate are shown in Fig. 8 for the 24-ply specimens. The applied load and corresponding strains are both normalized with respect to their analytical buckling values for each specimen so that postbuckling strains at the strain gage location can be compared for plates with different slot locations. Postbuckling strain response at the center of the plate was not affected significantly in the case of a slot located at some distance from the plate center. For example, for specimen C5, where the slot located longitudinally far from the strain gage location, the postbuckling strain response is similar to the response of unslotted control specimen of Ref. [45] (see Fig. 8). For the control specimen, bending strains at the corresponding strain gage location increased with loading in the postbuckling range, but membrane strains attained their

maximum value at the buckling load and became very small at failure. For specimens with a slot located close to the plate center, the slot had a significant effect on the strains. For example, membrane strains for specimens C1 and C2 not only diminished in magnitude, but also changed sign to become tensile (see Fig. 8). For specimen C2, which had a longer slot compared to C1, the magnitude of the tensile strain prior to failure was almost as large as the maximum compressive strain experienced during buckling (However, the maximum value of the compressive strain for specimen C2 was small at the plate center compared to the other specimens). The postbuckling strain response of specimen S1 was similar to that of the control specimen except that specimen S1 failed at a lower load.

Moire-fringe patterns indicate some effect of the slots on buckling mode shapes. Longer slots reduce the stiffness of the plates and allow larger out-of-plane deformations to occur. Increased out-of-plane deformations close to the slot location were observed from measurements and fringe patterns especially for specimens C2, C3 and C4. Specimen C4, which is the most flexible plate (it has small thickness and long slot) buckled into a three longitudinal halfwaves with the slot located at the maximum amplitude of the middle halfwave. The unslotted control specimen buckled into two

longitudinal halfwaves with the region corresponding to the slot position in specimen C4 being on the nodal line of the buckling mode.

Failure loads. Comparison of the failure loads of the plates with central slots and the control specimens indicates no major differences in results (see Figs. 6 and 7). Changing the length of the central slot from 2.5 cm to 5.1 cm did not have any effect on the failure loads of the 24-ply plates.

There was a reduction in postbuckling strength for all but one of the plates with offset slots. There was no reduction in postbuckling strength for specimen S2 which had its slot located close to the longitudinal centerline (see Fig. 5). A 25% reduction in the failure load occurred for the other three specimens with offset slots, namely S1, S3, and S4, where the slots are located close to one of the longitudinal edges of the plates. These longitudinal edges carry most of the applied load in the postbuckled state. Large shearing strains also occur after buckling in these highly loaded regions of the plates as a result of out-of-plane deflection gradients, $\partial w/\partial x$ and $\partial w/\partial y$, in both the longitudinal and lateral directions, respectively. Moire-fringe patterns indicate the presence of such gradients for these plates (see, for example Fig. 9). The failure load

is, therefore, reduced by the combined effects of the high values of shearing strains due to out-of-plane deflections and the stress concentrations at the slot tip, interacting with the high stresses at the longitudinal edges.

In addition to the interaction of the stress concentrations caused by the slot with the high postbuckling stresses at the plate edges, it is also possible that the slot tip and the plate boundary interact to influence the prebuckling stresses. The results of a linear-elastic finite element study of the effect of slot location on the fracture behavior of composite plates loaded in tension indicate that such a boundary interaction occurs. The stress intensity factor used to obtain the strength of the stress concentration around the slot tip was calculated with the finite element program of Ref. [33] for plates similar to the test specimens. For offset slots, the stress intensity factors at the slot-tip located closer to the boundary were substantially larger than those obtained for central slots of same length. The effect of the slot location on the stress intensity factor indicates that there is an effect of the boundary on the prebuckling stress distribution.

3.1.2.3   Failure characteristics

Central slots. The failure mode for the plates with central slots was similar to the failure mode of the control specimen of Ref. [45]. The coupling of the increased membrane strains near the specimen edges with the out-of-plane deflection gradients at the nodal lines introduced sufficient transverse shearing loads to fail the plate in a shear failure mode, which was accompanied by extensive delamination. For example, specimen C5, which had a slot machined close to its maximum out-of-plane deflection location, failed along a nodal line leaving the slot location undamaged (Fig. 10).

When the central slots were located close to a nodal line (specimens C1 through C4) visual inspections after failure indicated that delamination damage extended from the nodal line to the closest slot surface. The moire-fringe pattern for specimen C2 in Fig. 11, recorded by applying a small amount of load to buckle the delaminated area, indicates the extent of damage after failure. Apparently, interlaminar stress concentrations, associated with a free edge of the slot, interacting with the delaminations along the nodal line during the failure caused this behavior. Further inspection (C-scan) did not indicate significant damage to the upper portion (with respect to the slot in Fig. 11) of the plate even at distances close to the slot.

Offset slots. When the slots were located close to the edge
of a plate, there was extensive damage in the area between
the slot and the closest plate edge. The failure
characteristics were similar to those reported previously
[36,47] for strength-critical plates with large holes. In
these earlier studies, a shear crippling failure mode, see
Fig. 12, was observed in some 0° plies which is believed to
be initiated by local microbuckling of the 0° fibers in
regions of high strain concentrations. These crippled or
failed 0° fibers may have caused subsequent delaminations to
occur, and the combination of shear-crippled fibers and
subsequent delaminations is suspected to be the cause of the
local damage propagation that failed the plate below its
unnotched strength. It is suspected that the high strain
concentrations at the slot tip combines with the shear
strains to cause a similar type of failure for the offset
slots in the present work. Slot surfaces did not have
significant damage except for some local delaminations which
were mostly due to bearing of the slot surfaces on one
another at failure.

Specimen S2, with a slot only slightly offset from the
center (see Fig. 5), had a third type of failure mode which
is apparently due to differential out-of-plane deformations
of the slot surfaces interacting with the right slot tip.

The failure seemed to propagate from the right tip of the slot to the plate edge (see Fig. 13) even though the left tip of the slot is closer to the boundary. Inspection indicated a minimal amount of delamination along the entire width of the specimen compared to the other plates with offset slots. Furthermore, unlike the other plates, the strain versus load curve for the strain gages right below the slot tip near the longitudinal center line of the plate indicated a strain reduction for both the front and back strain gages at about 85% of the failure load. The simultaneous strain reduction in both back-to-back strain gages indicates a reduction in the axial load carried at the strain gage location. This reduction can occur when the slot extends laterally as a result of slot tip damage. However, axial strains are too low in the central region of the specimen to cause failure in the postbuckling range. It is suspected, therefore, that the out-of-plane deflections of the slot surfaces relative to one another combined with the axial strains to initiate failure at the slot tip possibly by microbuckling or crippling of the fibers locally. Damage at the slot tip allowed larger out-of-plane deformations of the slot surfaces which, in turn, caused the damage to propagate to the specimen edge.

3.1.3   Summary

For the slot and plate geometries selected, the overall prebuckling and buckling behavior of the notched plates was not significantly different than that of unnotched plates.

The postbuckling strength and failure mode were not affected by centrally located slots, and plates failed along a nodal line of the buckling mode in an induced shear failure mode.   This type of failure is typical of plates without slots loaded into the postbuckling range.   Slots located close to an edge of the plates, where high postbuckling membrane strains exist, reduced somewhat the load level at failure and the plates failed in a mode similar to that of strength-critical plates with large holes, see Fig. 12.   The failure mode induced by the strain concentrations near the slot tip was characterized by extensive damage in the region between the slot tip and the plate edge.

The results indicate that for buckling-critical plates the effects of central cracks are not important, and can probably be ignored by the designer.   The rest of this work, therefore, is focused on strength-critical plates.   The second half of this chapter is devoted to seeking a failure criterion for designing strength-critical notched plates in compression.

3.2   ANALYTICAL CRITERION

While the state of the art in predicting the strength and damage development of composites has progressed rapidly during the past decade, there are still some unresolved problems. One such problem is the analytical prediction of the compressive strength of unidirectionally reinforced composites, and even more so the compressive strength of composite plates with cracks. The literature of compressive failure models is reviewed in the next sub-section. Although some of the approaches discussed are reported to agree with the experimental results, their application is limited to cases where the stress state is simple (usually only uniaxial compression). Even if a cracked plate is loaded with simple uniaxial loads, stresses around a crack tip are complex. Therefore, the direct application of approaches developed in the literature for uncracked plates is not possible. Therefore, damage tolerance methodology that can be used in an automated design process for compression loaded composite plates with a crack does not exist. The purpose of this section is to develop a failure model based on microbuckling followed by breaking of the fibers under the combination of normal and shear stresses around a crack tip for use in the design of cracked plates under compressive loading.

3.2.1 Review of Literature

Early work on the compressive failure of fiber-reinforced composite materials has considered buckling of stiff fibers in a relatively flexible matrix [48,49]. Rosen [48] considered the composite material to consist of alternate layers of reinforcement and matrix materials (see Fig. 14). For his two-dimensional model, the two possible types of microbuckling failure are shown in Fig. 15. For the mode shown in Fig. 15-a, fibers may buckle in opposite directions, and the matrix is extended or compressed in a direction transverse to the fibers. This mode is called the extension mode. In the other mode, called the shear mode, the fibers buckle in phase with one another subjecting the matrix material to shear deformation (see Fig. 15-b). Assuming the buckling displacement v of individual fibers in the transverse direction to be in the form of sine waves

$$v = \sum_{m=1}^{\infty} a_m \sin\frac{m\pi x}{\ell} \tag{5}$$

Rosen used an energy approach to calculate the critical fiber stress for extension and shear modes respectively as

$$\sigma_{f,CE} = 2 \left[\frac{V_f E_m E_f}{3(1-V_f)} \right]^{\frac{1}{2}} \tag{6-a}$$

$$\sigma_{f,CS} = \frac{G_m}{V_f(1-V_f)} \tag{6-b}$$

where E_m, E_f are the extensional moduli of the matrix and fiber material, respectively, G_m is the matrix shear modulus, and V_f is the fiber volume fraction. The same microstability failure analysis was performed by Schuerch [49], who called the elastic failure of the stiffening constituent crippling failure, and extended the application of the model into inelastic microbuckling. Noting that the crippling failure occurs mostly at strain levels exceeding the yield point of his metal matrix, he suggested replacing the extensional and shear moduli of the matrix material with tangent moduli corresponding to the compressive strain level in the matrix. Reasonable agreement of limited test results with the inelastic analysis is reported in Ref. [49] for Boron/Magnesium composites.

Another approach, called macroscopic shear instability formulation, is proposed for cases where the flexural rigidity is large compared to the shear rigidity of the structure [50,51]. In case of a shear instability, buckling accompanying shear deformation will take place, and the buckling load will be governed by the shear rigidity of the structure rather than the bending rigidity. Early applications of this concept to two-dimensional orthotropic solids, as well as discretized beam and frame structures, are given by Hayashi [50]. For a two-dimensional solid, the

shear instability is expected to occur when the applied stress level, σ, reaches the shear modulus, G_{xy}, of the material [50].

Foye [51] has reached the same conclusion by considering a unit element of material taken out from a continuous two-dimensional orthotropic sheet. Using an energy approach, he obtained the modified stress-strain law under combined compressive and shear loading as,

$$\tau_{xy} = (G_{xy} + \sigma) \gamma_{xy} \qquad (7)$$

Eq. (7) indicates that the effective shear modulus of the material, $(G_{xy} + \sigma)$, decreases as the stress σ increases in compression until, at the limit, the material loses its effective shear stiffness and becomes susceptible to crippling in a shear mode. Expressing the composite shear modulus in terms of its constituents, the critical fiber stress, $\sigma_f = \sigma/V_f$, can be written as

$$\sigma_{f,C} = \frac{G_m}{V_f(1-V_f) + V_f^2(G_m/G_f)} \qquad (8)$$

If the ratio of the matrix to fiber shear modulus is negligible, Eq. (8) reduces to critical fiber stress given by Rosen, Eq. (6-b). An advantage of Eq. (8) over Eq. (6-b) is that it remains bounded for values of fiber volume fraction close to 1.0.

Early experimental works [52-54] do not correlate with the available two-dimensional models. Buckling of fibers in a three-dimensional helical pattern [53] instead of the two-dimensional modes assumed in the models was claimed to account for the 40% lower compressive stress observed in Ref. [52,53]. In order to close the gap between experimental and theoretical results and to aid better understanding of factors involved, several researchers have concentrated on different aspects of the compression failure of composites.

Herrmann [55] performed microbuckling analysis of a single, round fiber imbedded in a matrix. Three-dimensional elasticity was used by Herrmann to characterize the matrix behavior, but the interaction between the adjacent fibers was neglected. Additionally, in a real composite material, fibers may have initial curvatures due to imperfections in the manufacturing process. The crookedness of fibers is considered to lower the compressive strength of unidirectional composites [55-57]. Beside microbuckling, fiber-matrix separation has been investigated by several researchers [57-59]. Prebuckling separation between fiber and matrix has, for example, been shown to decrease the buckling load of the fiber [58]. Broad reviews of early analytical and experimental work on microbuckling of

composites and further references can be obtained in Refs.
[60-62].

More recent investigations [63-67] suggest another type
of compressive failure mechanism, called fiber kinking
failure which is characterized by a band of buckled,
fractured fibers that has undergone both shearing and
compressional deformations as seen in Fig. 16. Experimental
investigations have shown that localized fiber rotations due
to microbuckling are associated with the kinking process
[64]. Fiber fracture strength is viewed as a primary
property governing the kink formation [64-67]. Weaver [65]
concluded that the kinking process is initiated by the
transverse fracture of buckled fibers in the composite
laminate. Kink formation is assumed to nucleate at a
material defect point such as a region with poor fiber
alignment [63] or at a notch that acts as a stress
concentrater [68]. The propagation of kinking through the
composite is preceded by a process of successive buckling
and fracture of adjacent fibers to form the kink band. The
nature of this process is essentially the same as the crack
propagation from a notch under tensile loading that causes
fibers to break successively. Indeed, Chaplin [68]
postulated that the prediction of compression failure of
composites is a classical fracture mechanics problem that

requires the determination of the extent of the degradation in compressive load carrying capacity of a given defect.

Based on the observations of References given in the previous paragraph, it is conceivable that the strength failure of composite plates with a crack is governed by fiber kinking. Compressive fatigue tests by Berg and Salama [69] and static tests by Parry and Wronski [70] of notched specimens indicate that microbuckling in the form of kink band formation at the tip of the notches is the principal mechanism of compressive notch extension and failure. Also, the shear crippling failure observed by Rhodes et al. [47] in compressive specimens with a hole (see Fig. 12) is believed to be initiated by local microbuckling of 0° plies followed by fiber kinking.

Some of the failure criteria developed for strength prediction of plates with holes and notches under tensile loadings have also been used for predicting compressive fracture strengths [47,71,72]. Rhodes et al. [47] and Haftka and Starnes [72] have used the point-stress criterion due to Whitney and Nuismer [23] for flat plates with holes. Nuismer [71] used the average-stress criterion. A description of these criteria is given in the previous chapter. It is claimed in Ref. [47] that the point-stress failure criterion can be an effective tool for predicting

and understanding the failure of graphite/epoxy composite laminates with holes and provides insight in predicting failure of panels with other flaw types. However, direct use of the criterion in a design process is limited. The point-stress criterion does not provide insight into the local material behavior and does not relate the local behavior to the failure process. Also, the stress state close to a notch or other types of cut-outs is usually complicated. The point-stress and average-stress criteria, like the previous microbuckling criteria [48,51,65], consider failure as a result of only the unidirectional compressive stresses and, therefore, are not suitable for the failure of compressively loaded notched plates.

3.2.2   Damage Model for Cracked Plates in Compression

As discussed previously, shear crippling of the principal load-carrying fibers is one of the most common damage mechanisms that are observed in compressively loaded composite laminates [73]. Such a mechanism can be activated by the microbuckling of the fibers within the laminae. In addition to high compressive stress concentrations, which may be the main cause of microbuckling of the fibers, significant in-plane shearing stress concentrations exist near the tips of a crack. Transverse shear deformations

were shown analytically to have a detrimental effect on the compressive strength of composites [74]. The experimental findings discussed in the first part of this chapter verify that claim. Also, Shuart and Williams [75] suggested that failure of plates with central holes is affected by the presence of such shearing stresses around the edges of the hole.

The objective of this section is to include those shearing stresses around a crack in a model for predicting the failure of composite plates under compressive loadings. An important issue in the development of a failure criterion for cracked plates is the singularity of the stress field at the crack tip. The magnitude of stresses near the crack tip is inversely proportional to the square root of the distance from the crack and, therefore, becomes infinitely large at the crack tip. The model developed must be capable of accounting for this stress singularity. Two main approaches are used in the literature. One approach is to combine some of the terms that multiply the singularity term and assume that these have an upper value which is a material constant at failure. This is done mostly in classical fracture mechanics applications. Also the criterion used in chapter 2 is based on a variation of this approach. Another approach is to associate the failure with what is happening

at (or within) a specified distance from the crack tip. The classical examples of this latter approach are the point-stress and average-stress criteria. The two approaches of avoiding the singularity are equivalent and either one of them can be used. In the present work, the latter approach will be utilised.

3.2.2.1 - Crack tip stresses

The strain components of Eq. (1) along the principal material direction of a ply with an arbitrary orientation are based on the stress field given by

$$
\begin{Bmatrix} \sigma_x \\ \sigma_y \\ \tau_{xy} \end{Bmatrix} = \frac{K_I}{\sqrt{2\pi r}} \begin{Bmatrix} 1 \\ \sqrt{E_y/E_x} \\ 0 \end{Bmatrix}
\tag{9}
$$

The stresses given in Eq. (9) are restricted to the points along the y axis, $\psi = 0$ (see Fig. 3), and neglect the mode II, in-plane shearing mode, stress intensity factor. The more general case of Eq. (9) for the analytical solution of stresses around the crack tip [76] is

$$
\sigma_x = \sigma_x^\infty + \frac{K_I}{\sqrt{2\pi r}} \mathrm{Re}(Z_1) + \frac{K_{II}}{\sqrt{2\pi r}} \mathrm{Re}(Z_2)
\tag{10-a}
$$

$$
\sigma_y = \sigma_y^\infty + \frac{K_I}{\sqrt{2\pi r}} \mathrm{Re}(Z_3) + \frac{K_{II}}{\sqrt{2\pi r}} \mathrm{Re}(Z_4)
\tag{10-b}
$$

$$
\tau_{xy} = \sigma_{xy}^\infty + \frac{K_I}{\sqrt{2\pi r}} \mathrm{Re}(Z_5) + \frac{K_{II}}{\sqrt{2\pi r}} \mathrm{Re}(Z_6)
\tag{10-c}
$$

where

$$Z_1 = \frac{1}{s_1 - s_2} \left(\frac{s_1}{\sqrt{C + s_2 S}} - \frac{s_2}{\sqrt{C + s_1 S}} \right)$$

$$Z_2 = \frac{1}{s_1 - s_2} \left(\frac{1}{\sqrt{C + s_2 S}} - \frac{1}{\sqrt{C + s_1 S}} \right)$$

$$Z_3 = \frac{s_1 s_2}{s_1 - s_2} \left(\frac{s_2}{\sqrt{C + s_2 S}} - \frac{s_1}{\sqrt{C + s_1 S}} \right)$$

$$Z_4 = \frac{1}{s_1 - s_2} \left(\frac{s_2^2}{\sqrt{C + s_2 S}} - \frac{s_1^2}{\sqrt{C + s_1 S}} \right)$$

$$Z_5 = \frac{s_1 s_2}{s_1 - s_2} \left(\frac{1}{\sqrt{C + s_1 S}} - \frac{1}{\sqrt{C + s_2 S}} \right)$$

$$Z_6 = \frac{1}{s_1 - s_2} \left(\frac{s_1}{\sqrt{C + s_1 S}} - \frac{s_2}{\sqrt{C + s_2 S}} \right)$$

where $C = \cos \psi$ and $S = \sin \psi$. s_1, s_2 and their complex conjugates in the above equations are the roots of the characteristic equation given by

$$a_{11} s^4 + 2a_{16} s^3 + (2a_{12} + a_{66}) s^2 - 2a_{26} s + a_{22} = 0 \qquad (11)$$

where the a_{ij} are the elements of the laminate compliance matrix.

Analysis of the plates considered in this work is limited to symmetric plates with balanced laminates. This restriction eliminates the mode II stress intensity factor leaving only the first two terms in Eqs. (10-a,b, and c). However, for $\psi \neq 0$, considerable shear stresses can be obtained with Eq. (10) in contrast to Eq. (9). A typical shear stress distribution around the crack tip is given in

Fig. 17 for a quasi-isotropic plate under uniaxial loading in x-direction that produce a stress intensity factor of 2500 MPa$\sqrt{mm}$.

3.2.2.2   Fiber-beam model

The approach used here is to modify Rosen's microbuckling model [48] to account for the shearing stresses that are obtained from the formulation in the previous section at an angle, $\psi \neq 0$, around the crack tip. The analytical formulation of the problem follows the same set of assumptions that are used in the original formulation of the microbuckling model, see Fig. 14. Individual fibers of length ℓ are considered as beams on elastic foundation. The cross section of the beams is rectangular with a thickness equal to the fiber thickness h and a unit depth. The thickness of the foundation is equal to the distance between fibers, 2c. The assumed mode of fiber deformation within a lamina at a point around the crack tip is shown in Fig. 18. In contrast to the two deformation shapes considered in Rosen's microbuckling model, namely extension and shear modes, only the shearing mode of deformation is considered in the present approach. This is a natural consequence of the existence of the shearing force which forces the fibers to deform in phase with one another.

An energy approach is used for the formulation of the equilibrium equation and boundary conditions. Neglecting the shearing deformations of the fiber and the extensional deformations of the matrix, the strain energy of the system can be written as

$$U = \frac{1}{2} \int_o^{\ell} E_f I_f (v'')^2 \, dx + \frac{1}{2} \int_o^{\ell} 2c \, \tau_{xy} \gamma_{xy} \, dx \qquad (12)$$

where $\tau_{xy} = G_m \gamma_{xy}$, $\gamma_{xy} = (1 + \frac{h}{2c}) v'$, and the prime denotes differentiation with respect to x (the coordinate along the fiber in Fig. 19).

In addition to the potential energy of the axial force P_f which is considered in previous model, there is also the potential energy due to the side force S_f which is applied at the free end of the beam as shown in Fig. 19.

$$\Omega = \frac{1}{2} P_f \int_o^{\ell} (v')^2 \, dx + S_f \int_o^{\ell} v' \, dx \qquad (13)$$

The side force S_f is assumed to be the result of shearing stresses at the point of interest.

Taking the first variation of the total energy and equating it to zero, the equilibrium equation for the fiber can be obtained as

$$(E_f I_f \, v'')'' + [P_f - 2c \, G_m (1 + \frac{h}{2c})^2] \, v'' = 0 \qquad (14)$$

and general boundary conditions at x = 0 and x = ℓ as,

I - either v=0 or $-(E_f I_f v'')' + [2c G_m (1+\frac{h}{2c})^2 - P_f] v' - q P_f = 0$

II- either $v'=0$ or $E_f I_f v'' = 0$

where $q = \frac{S_f}{P_f}$. Since the ratio of the axial force to the shearing force stays constant at any point around the crack tip as the applied load is increased, it is advantageous to use a new variable q as defined above.

Assuming that the fiber ends remain straight during the deformation, (see Fig. 19), the general boundary conditions given above reduce to

at $x = 0$ i- $v = 0$ ii- $v' = 0$

at $x = \ell$ iii- $v' = 0$ iv- $v''' = -\frac{q P_f}{E_f I_f}$

The loading on the fiber is symmetric with respect to the midpoint of the fiber (the uniform shear stress field along the length of the beam is modeled as two equal opposite concentrated forces at two ends). Therefore, symmetric end conditions are preferred and zero slope clamped-clamped end conditions are selected. A more realistic set of end conditions would have been to let the ends to rotate under loading by using rotational springs at the ends. But, the determination of elastic constants for such rotational springs is complicated and therefore not used in the present work.

Applying the above boundary conditions to the equilibrium equation, (14), yields three independent solutions depending on the value of the axial force P_f,

I - For $P_f \leq 2c\,G_m(\ 1 + \dfrac{h}{2c}\ )^2$

$$v = -\frac{qP_f}{E_f I_f (k_1)^3}[\,Sinh k_1 x - k_1 x - \frac{(Cosh k_1 \ell - 1)}{Sinh k_1 \ell}(Cosh k_1 x - 1)\,] \quad (15)$$

where $(k_1)^2 = [2c\,G_m(\ 1 + \dfrac{h}{2c}\ )^2 - P_f\,] \ / \ E_f I_f$

II - For $P_f = 2c\,G_m(\ 1 + \dfrac{h}{2c}\ )^2$

$$v = \frac{qP_f x^2}{2E_f I_f}(\frac{\ell}{2} - \frac{x}{3}) \quad (16)$$

III - For $P_f \geq 2c\,G_m(\ 1 + \dfrac{h}{2c}\ )^2$

$$v = \frac{qP_f}{E_f I_f (k_2)^3}[\,Sin k_2 x - k_2 x + \frac{(Cos k_2 \ell - 1)}{Sin k_2 \ell}(Cos k_2 x - 1)\,] \quad (17)$$

where $(k_2)^2 = [\ P_f - 2c\,G_m(\ 1 + \dfrac{h}{2c}\ )^2\ ] \ / \ E_f I_f$

Note from the above solutions that the value of the side displacement v is unbounded for $Sin\,k_2 \ell = 0$ which gives a critical load of

$$P_{f,C} = 2c\,G_m\ (\ 1 + \frac{h}{2c}\ )^2 + \frac{\pi^2}{\ell^2}\,E_f I_f \quad (18)$$

and substituting

$$V_f = \frac{h}{h+2c} \qquad I_f = \frac{h^3}{12} \qquad and \qquad P_{f,C} = \sigma_{f,C}\,h$$

in Eq. (18), we obtain the critical value of the stress for shear mode of the microbuckling model given by Rosen [48], see Eq. (6-b). The second term in Eq. (18) is neglected by Rosen by assuming the buckling wave length ℓ to be much larger than the fiber width h. For the wave lengths considered in the present work, the contribution from the second term is comparable to the first one and, hence, will be retained.

3.2.2.3 Fiber-beam deformation under loading

The normalized side displacement, v/ℓ, of the tip ($x=\ell$) of a fiber-beam of length $\ell = 0.05$ mm under the combined axial, P_f, and side load, S_f, is given in Fig. 20 by solid lines for four different values of the ratio of the side load to axial load, (q = 0.05, 0.20, 0.35, 0.50). The applied axial fiber load, P_f, in the figure is normalized by the critical fiber load obtained from Eq. (18). Material properties typical of graphite/epoxy, Table 2, are used for the calculations. Fiber and matrix thicknesses of 0.008 mm and 0.005 mm, respectively, are assumed. It is apparent from the figure that even for side loads of only 5 % of the axial force significant displacements are possible at loads substantially smaller than the bifurcation load (indicated by horizontal line on the figure).

The dashed lines in the figure are obtained by considering the change of the effective shear modulus of the material according to Eq. (7) as the compressive load is increased. It is assumed that the decrease in the effective laminate shear modulus is due to a decrease in the matrix shear modulus G_m only. The change in G_m with the loading is calculated by assuming that the shearing stresses on the fiber and the matrix are the same [77].

3.2.3   Failure Model

The failure model developed in the present work is based on the fact that large fiber bending stresses can be induced due to microbuckling of the fibers of the principal load-carrying plies around the crack tip.

3.2.3.1   Fiber stresses

For a fiber of unit depth and a thickness h, the maximum bending stress at a cross section is

$$\sigma_b = \frac{6\ M}{1 \cdot h^2} \tag{19}$$

where the bending moment, M, is given in terms of the fiber deformation by

$$M = E_f I_f v'' \tag{20}$$

The maximum compressive stress in a fiber is the sum of the normal compressive stress due to P_f and the maximum compressive bending stress. The maximum bending stresses are achieved at both ends of the fiber, at $x=0$ and $x=\ell$. Depending on the value of the axial fiber force, the expressions for the fiber deformation from Eqs. (15), (16), or (17) can be used to find the maximum compressive stress at the fiber as

I - For $P_f \leq 2c\, G_m (\,1 + \dfrac{h}{2c}\,)^2$

$$\sigma_{f,max} = \frac{P_f}{h} + \frac{6qP_f}{h^2 k_1} \frac{(\mathrm{Cosh}k_1\ell - 1)}{\mathrm{Sinh}k_1\ell} \qquad (21\text{-}a)$$

II - For $P_f = 2c\, G_m (\,1 + \dfrac{h}{2c}\,)^2$

$$\sigma_{f,max} = \frac{P_f}{h} + \frac{3q\ell P_f}{h^2} \qquad (21\text{-}b)$$

III- For $P_f \geq 2c\, G_m (\,1 + \dfrac{h}{2c}\,)^2$

$$\sigma_{f,max} = \frac{P_f}{h} - \frac{6qP_f}{h^2 k_2} \frac{(\mathrm{Cos}k_2\ell - 1)}{\mathrm{Sin}k_2\ell} \qquad (21\text{-}c)$$

The maximum fiber stresses for the same four q values used in the previous figure are plotted in Fig. 21 with solid lines as the fiber load is increased. The fiber stress is normalized by the critical fiber stress, and the applied axial fiber load is normalized by the critical fiber load. As in the case of the Fig. 20 curves given by the

dashed lines are obtained by considering the softening of the shear resistance of the material under the compressive load. The fiber compressive stress in the absence of bending, $q = 0$, increases linearly with the load. But, even a small amount of shearing load causes a large increase in the stress and induces slight nonlinearities. It is proposed here that these large compressive stresses, which are the result of bending of the fibers, may be the cause of breaking of the fibers and lead to crippling of the load carrying plies.

The value of the maximum stress that can be carried by a fiber is not well established in the literature. Fiber manufacturers report strength values in the range of 2500 MPa to 4000 MPa under tensile loadings, but values for the compressive strength are not available. Based on experimental results, calculated values for the fiber compressive failure stress are reported to be around 3000 MPa in Ref. [65] for carbon fibers. This value is used for the implementation of the model in the following sections. Note from Fig. 21 that for stress levels below 3000 MPa the effect of shear softening is small. Therefore shear softening is not included in the failure model. The value of the fiber length assumed for the model is $\ell = 0.05$ mm. This is a representative value for the length of fiber breaks observed in Ref. [65].

3.2.3.2   Failure prediction for cracked plates

As with the point-stress criterion, the implementation of the proposed model calls for determination of the distance ahead of the crack tip where the maximum fiber stress is compared to the allowable fiber stress value. The maximum fiber stress is a function of both the axial and shearing forces that change their relative values depending on the angular orientation of the point around the crack tip. For the present work, it is assumed that the radial distance r to the failure check point is a material constant which is independent of the ply combinations and stacking sequence of the laminate. However, for a given distance r it is necessary to search for a point on a circle with radius r, where the combination of axial and shear forces that maximizes the fiber stress for the principal load-carrying lamina is obtained.

To determine the value of r, experimental values of far-field failure strain for quasi-isotropic plates with machined cracks of different lengths from Ref. [47] are used. A finite element program with a special crack tip element [33] is used to relate the stress intensity factor at failure to the far-field failure strain and Eq. (10) is used to define the stress field in the immediate neighbourhood of the crack tip. Once the stresses are

obtained, the longest distance, r, to the point at which combination of axial and shear stresses causes breaking of the fiber is calculated for each of the quasi-isotropic specimens of Ref. [47]. The average of the distance r for all those specimens with different crack lengths is calculated to be 1.5 mm. A prediction curve based on the average value of r = 1.5 mm is shown in Fig. 22 with a solid line. Another prediction curve based on an average value of r = 0.05 mm is also generated, shown by the dashed line in Fig. 22, by excluding the effect of shearing force and using the microstability failure criterion of Rosen [48] given by Eq. (6-b). Both predictions seems to be in good agreement with the experimental values (circular symbols) in representing the failure behavior of the plate as the crack aspect ratio changes. Only at small crack aspect ratios do the two predictions give slightly different results. A slightly less steep prediction curve obtained with the present approach agrees better with the experimental results in this case.

The real challenge for the model is to match experimental failure loads of plates with various ply compositions and stacking sequences that introduce a different degree of orthotropy. Unfortunately, no experimental data have been found in the literature for

orthotropic plates with cracks. For plates with holes, on the other hand, some experimental data are available. The finite element mesh generator used in the present work is limited to plates with cracks, and the focus of this work is limited to designing plates with cracks that simulate a damage condition. However, because of the availability of such data, an attempt is made next to test the model for plates with holes assuming that analysis of cracked plates will give us some idea of the failure of plates with holes.

3.2.3.3   Failure prediction for plates with holes

For the analyses of plates with holes, the crack finite element program is used with a crack size equal to the hole diameter. First, a value of the radial distance ahead of the crack tip for each of the experimental quasi-isotropic plates with holes in Ref. [47] is determined so that the combined bending and axial stress in the fiber is equal to the fiber failure stress. The average of the distance r for those quasi-isotropic specimens is calculated to be 2.5 mm. Experimental values of the far field failure strain for those quasi-isotropic plates are given in Fig. 23 by circular symbols together with some experimental values for ±45° dominated plates shown by triangles and squares. Predictions made using the present model with r = 2.5 mm are

shown with the solid lines in the figure. Dashed lines are obtained by using Rosen's [48] microbuckling criterion with r = 0.08 mm. For the quasi-isotropic specimens, both models show good agreement with the experimental results. As in the case of cracked plates, the present model seems to have a slight advantage over the classical microbuckling model for small values of the crack aspect ratio. However, both predictions seem to confirm that analyses made with cracks can be used to represent the hole size effect for specimens with holes. Based on the same values of the distance r, predictions are also made for two ±45° dominated layups, namely $[(\pm 45)_{12}]_S$ or $[(\pm 45/\mp 45)_6]_S$ and $[(\pm 45/\pm 45)_2/90_3/\pm 45/\pm 45/90_3/\pm 45/\pm 45/90_2]_S$, see Fig. 23. The predictions obtained by the present model seem to capture the essential trend of the experimental results and show a reasonable agreement, while the Rosen's microbuckling criterion predicts far field failure strains which are too high. This is expected because the failure of ±45° dominated layups are affected more by shearing stresses [75] than 0° dominated layups.

The proposed model is also checked against a recent experimental investigation, Ref. [72], of the effect of degree of orthotropy of layup on failure loads. Experimental results are for 127 mm wide graphite/epoxy

specimens with a 25.4 mm hole. Specimens are all 78 plies thick with a fixed number of 90° plies. Four different layups were tested, $[\pm45_{18}/90_3]_S$, $[0_6/\pm45_{15}/90_3]_S$, $[0_{12}/\pm45_{12}/90_3]_S$, and $[0_{18}/\pm45_9/90_3]_S$, with 0° ply thicknesses constituting 0%, 15%, 31%, and 46% of the total thickness. Experimental values of the failure loads are shown with circular symbols in Fig. 24. Predictions made by the present model (r = 2.5 mm) and Rosen's model are (r = 0.08 mm) presented by the square and rectangular symbols, respectively. Although both predictions are at least 40% higher than experiments, the present model seems to agree with the trend of the experiments better than the microbuckling model without the shear. Predictions made in Ref. [72] are also included in the figure as indicated by pluses. They are obtained by using a point-strain criterion so that the fiber strains in the 0° plies will not exceed 1.4% (2.4% in the ±45° plies for the $[\pm45_{18}/90_3]_S$ specimen) at a distance around the hole. The distance r = 0.5 mm is obtained to give a best fit for experimental results in Ref. [72]. But, the trend of the prediction is equivalent to the trend of the Rosen's model.

It is interesting to note in Fig. 24 that present predictions made for percent of 0° plies higher than 50% indicate a drop in the load-carrying capacity of the plates,

whereas the microbuckling model without the shearing stresses predicts increased load carrying-capacity. No experimental work that investigates the compression failure of laminates with such a high percentage of $0°$ plies have been found in the literature. It is hoped that the present investigation may motivate some activity in that direction.

Chapter IV

ANALYSIS AND DESIGN

As explained in Chapter 2, the failure criterion for tension-loaded plates requires the evaluation of the stress intensity factor and the critical value of the stress intensity factor for a given plate. The failure criterion developed in Chapter 3 for compression-loaded plates is, on the other hand, based on the fiber stress in the principal load-carrying lamina at a certain distance from the crack tip. But, the stresses in the immediate surroundings of the crack tip are obtained in terms of the value of the stress intensity factor. Therefore, the stress intensity factor is also needed for the implementation of the compression failure criterion.

Analyses of plates for the stress intensity factor are performed with a finite element program which is driven by an optimization algorithm. The interface between the analysis and the optimization programs is fully automated. Any change in the plate geometry at any stage of the design process is transfered to the analysis program without need of intervention by the user. A more detailed explanation of the analysis and design techniques, and design capabilities is given in the following sections.

4.1 STRESS INTENSITY CALCULATIONS

The SIF, which is a function of loading and plate geometry, is evaluated by a finite element computer program developed by Chu et al [33]. The program is suitable for a two-dimensional elastostatic analysis of plane anisotropic homogeneous sheets with a through-the-thickness crack. The program employs two special crack-tip elements that account for the singular stress field associated with two crack-tip displacement modes. An 8-node element capable of representing mode I (the opening mode) displacements, in which the crack surfaces separate, is restricted to symmetric problems. The other element has 10 nodes and is also capable of representing mode II (the sliding mode) displacements in which the crack surfaces slide over each other in a direction perpendicular to the line of the crack front. In the present application of the program, only symmetric plates with a central crack under symmetric loading are considered so that only one quarter of the plate need be modeled. The program is capable of analyzing only membrane action so that bending can not be included. Therefore, only balanced symmetric laminates with symmetric stiffeners subjected to in-plane loading are considered.

A typical stiffened plate geometry is shown in Fig. 25. The plate is composed of plies with various

orientations. The flanges and the stiffeners are obtained by specifying additional thicknesses of material on top of the basic panel material. An automatic mesh generator, which is described in the next section, was developed to permit better utilization of the analysis program during the design process. A typical quarter-plate finite element mesh for a stiffened panel is given in Fig. 26. The mesh generator can model a crack which partially enters the flanges, but not a crack which goes through the stiffener blade. The stiffener is assumed to be perfectly bonded to the panel, and a single layer of finite elements is used for both the stiffener and the panel, by calculating the combined material properties.

The boundary conditions applied at the loaded edge of the finite element model simulate static test loading conditions. In a typical loading apparatus, the load is transmitted to the specimen through rigid components which can be simulated by applied uniform displacements at the boundary of the model. However, the magnitude of the applied load can not be controlled with such a model. The static test boundary conditions are achieved by employing a two-stage process. First, unit displacements in the direction of the load are applied along the boundary. The SIF and the total reaction force at the boundary are

calculated. Next, the ratio between the actual desired load and the total reaction force due to unit displacements is calculated and the SIF and other plate response quantities are multiplied by that ratio.

4.2   AUTOMATIC MESH GENERATION

A special mesh generation program is developed to interface the analysis program mentioned in the previous section with the optimization package that drives the design. The interface program serves two purposes. First, for a given initial plate geometry, the program discretizes the plate into triangular elements and a rectangular element at the crack tip, and initializes the material properties and thickness of elements. The second purpose of the interface program is to modify the finite element mesh as the design variables which control modeling parameters change during the design process. The modifications that can be made on the model of the plate include geometry of the plate (stiffener width and spacing, and crack length to a certain extent) as well as the thicknesses and material properties of elements. The capability of modifying geometry allows the use of shape parameters as design variables. However, no attempt has been made in the present work to use shape design variables.

For unstiffened plates, the parameters that define the model are plate width (W), plate length (L), total crack length (2a), and number of rows of elements desired along both the half-width and the half-length of the plate away from the crack. For example, the quarter-plate finite element mesh shown in Fig. 27 has four rows of elements along the half-width and twelve rows of elements along the half-length. The number of rows of elements along the half-length of the plate remains constant along the width of the plate. The number of rows along the half-width doubles twice at prescribed distances (built into the program) from the loaded edge before reaching the crack, and conforms with the crack tip finite element which has a three to one aspect ratio, Fig. 27.

The thicknesses and material properties of all the elements in a model are same for unstiffened plates. The input parameters required to obtain the element thicknesses and material properties are the number of plies, the thickness and orientation of each ply that constitute the layup, and the unidirectional material properties.

The mesh generation program permits modelling of a stiffened plate with up to four stiffeners, see Fig. 26. Stiffened plates discretizations are obtained using the unstiffened plate discretization as a starting base. The

middle bay of the plate (the section of the plate between the middle two stiffeners) is modelled exactly the same way as an unstiffened plate. For example, the middle bay of the mesh shown in Fig. 26 is obtained by using two rows of elements along the half-width and sixteen rows of elements along the half-length. Additional rows of elements are used to model the rest of the plate. The number of additional rows of elements is related to the dimensions of the remaining sections (stiffener blade width and flange width) of the plate and the number of rows of elements in the middle bay. A somewhat coarse mesh is used for the rest of the plate to keep down the number of total elements in a reasonable range. The parameters that are required, besides the number of rows of elements in the middle bay, for the complete definition of a stiffened plate are plate length (L), stiffener spacing (e), stiffener blade width (b), and stiffener flange width (d).

The thicknesses and material properties of the elements in the stiffener blades and flanges are obtained by adding plies on top of the plies that constitute the middle bay of the plate. All sections of the plate (stiffener blades, stiffener flanges, and bays of the plate) are uniform along the length of the plate.

The design variables that are used in the present work are the thicknesses and orientations of plies in different sections of the plates. Therefore, once the initial mesh is generated, the portions of the mesh generation that relate to the plate discretization are skipped during the design and only element thicknesses and material definitions are modified for successive design iterations.

4.3 PROBLEM FORMULATION AND OPTIMIZATION METHOD

The design problem is formulated as a typical weight minimization problem stated as

$$\text{Minimize} \qquad C \, W_g(\, X \,)$$

$$\text{such that} \qquad g_{SIF} = 1 - [K_I \, / \, K_c] \geq 0$$

$$g_\sigma \geq 0 \qquad\qquad (22)$$

$$X_L \leq X \leq X_U$$

where X is the vector of design variables, $W_g(X)$ is the weight, C is a convenient normalizing constant, g_{SIF} is the stress intensity factor constraint, K_I and K_c are the SIF and its critical value respectively, and X_L and X_U are vectors of lower and upper bounds, respectively, on the design variables. The form of the stress intensity factor constraint given in Eq. 22 is used for both tension-loaded and compression-loaded plate designs. For tension-loaded plates, the K_I value is compared with the critical value of

the stress intensity factor which is called the fracture toughness. For the compression case, the process of finding the stresses for a given stress intensity factor is reversed to find a value of the stress intensity factor that corresponds to a maximum allowable fiber stress at a predetermined distance. This value of the stress intensity factor, which is a function of both the layup and the material properties, is used for the critical stress intensity factor K_c under compression. Beside the stress intensity factor constraint, stress constraints, g_σ, based on the Tsai-Hill failure criterion applied to each layer of the laminate, are also used for some designs. Classical lamination theory is used to calculate the ply stresses. The design variables may include all the parameters defining the geometry of the plate in Fig. 25 as well as thicknesses and orientations of each ply of the laminate in each section of the plate, (i.e., panel, stiffener flange, stiffener blade). No constraints were used for the thickness design variables to maintain integer number of plies in the final designs.

General purpose mathematical optimization programs, NEWSUMT [78] and its modified version NEWSUMT-A [79], are used to obtain minimum weight plates. NEWSUMT employs the Sequential Unconstrained Minimizations Technique with an

extended interior penalty function formulation [80] for converting the constrained problem into a sequence of unconstrained problems. This type of penalty function has the advantage, over exterior and interior penalty functions, of being able to start with an infeasible design and stay in the feasible design space for subsequent designs. Newton's method is used for solving the unconstrained minimizations. The second derivatives of the penalty function are approximated by using expressions involving only first derivatives of the constraints. Additionally, NEWSUMT-A employs constraint approximations and has a move limits strategy. Computational time savings of up to 70%-80%, depending on the number of design variables, were achieved by using NEWSUMT-A instead of NEWSUMT with comparable results.

An analytical approach is used to obtain the first derivatives of the constraints with respect to the design variables (often called design sensitivity derivatives). The special nature of the boundary conditions used at the loaded edge of the plate required a modification of the standard adjoint method for sensitivity derivatives. The details of the sensitivity derivative calculations are discussed in the next section.

4.4 DESIGN SENSITIVITY DERIVATIVES

The adjoint variable technique (known also as the dummy load technique, Ref. [81]) is widely used for calculating sensitivity derivatives of stress and displacement constraints in structural optimization applications. It is more efficient than the direct method for obtaining these derivatives when the number of design variables is larger than the number of active displacement or stress constraints.

The application of the method is straight-forward for simple displacement or stress boundary conditions. For more generalized boundary conditions, it requires specialized treatment. Hsieh and Arora [82], for example, employ Lagrange multipliers to extend the method to general displacement boundary conditions. This section is concerned with the application of the adjoint variable method under the special combination of displacement and stress boundary conditions which occurs when static test conditions are simulated.

As it was discussed previously, the static test loading boundary conditions are achieved by using a two-step approach. First, a unit displacement vector I (in the direction of the load) is applied to those nodes at the loaded end of the finite element model. Algebraically, the

calculation of the internal stresses and displacements, as well as the forces at those displaced nodes, can be shown by using the partitioned form of the equilibrium equation for a structure discretized by a finite element

$$
\begin{bmatrix} K_{aa} & | & K_{ad} \\ --- & | & --- \\ K_{ad}^T & | & K_{dd} \end{bmatrix} \begin{Bmatrix} U_I \\ -- \\ I \end{Bmatrix} = \begin{Bmatrix} 0 \\ -- \\ R_I \end{Bmatrix} \tag{23}
$$

where K_{aa}, K_{ad} and K_{dd} are submatrices of the stiffness matrix, U_I is the unknown displacement vector per unit applied boundary displacements, R_I is the reaction force vector under the unit applied displacement and 0 is a null vector.

Once the system in Eq. (23) is solved, the total load applied to the specimen, when the displacement vector I is specified, can be obtained by

$$
P_I = I^T R_I \tag{24}
$$

If the required applied load is P, then the displacement vector U under the actual required loading is

$$
U = s \, U_I \tag{25}
$$

where

$$
s = \frac{P}{P_I} \tag{26}
$$

Now, assume that the derivative of some function g of the displacement field (e.g., a stress component) with respect to a design parameter x is required. The function can also depend explicitly on the design parameter so that $g = g(x,U)$. The derivative of g with respect to x may be written as

$$\frac{dg}{dx} = \frac{\partial g}{\partial x} + Z^T \frac{dU}{dx} \tag{27}$$

where Z denotes a vector with $z_i = \frac{\partial g}{\partial u_i}$. Using Eq. (25), we obtain

$$\frac{dg}{dx} = \frac{\partial g}{\partial x} + Z^T [\frac{ds}{dx} U_I + s \frac{dU_I}{dx}] \tag{28}$$

For $\frac{dU_I}{dx}$ differentiate Eq. (23) with respect to x to obtain

$$K_{aa} \frac{dU_I}{dx} = - \frac{dK_{ad}}{dx} I - \frac{dK_{aa}}{dx} U_I \tag{29}$$

$$\frac{dR_I}{dx} = \frac{dK_{ad}^T}{dx} U_I + K_{ad}^T \frac{dU_I}{dx} + \frac{dK_{dd}}{dx} I \tag{30}$$

Finally, to obtain $\frac{ds}{dx}$ differentiate Eqs. (24) and (26):

$$\frac{ds}{dx} = \frac{dP}{dx}/P_I - \frac{s}{P_I} I^T \frac{dR_I}{dx} \tag{31}$$

The direct method for obtaining $\frac{dg}{dx}$ starts by solving Eq. (29) for $\frac{dU_I}{dx}$, then obtaining $\frac{dR_I}{dx}$ from Eq. (30) and $\frac{ds}{dx}$ from Eq. (31), and finally using Eq. (28). The direct method has a disadvantage that the

entire process of calculation has to be repeated for any other design variable.

To obtain the adjoint method, we first transform Eq. (31) with the aid of Eqs. (23), (29) and (30)

$$\frac{ds}{dx} = \frac{dP}{dx}/P_I - \frac{s}{P_I}[2I^T \frac{dK_{ad}}{dx} U_I + I^T \frac{dK_{dd}}{dx} I + U_I^T \frac{dK_{aa}}{dx} U_I] \qquad (32)$$

An adjoint variable Λ is now defined as the solution to

$$K_{aa} \Lambda = Z \qquad (33)$$

Using Eqs. (29) and (33), Eq. (28) becomes

$$\frac{dg}{dx} = \frac{\partial g}{\partial x} + \frac{ds}{dx} Z^T U_I - s\Lambda^T [\frac{dK_{ad}}{dx} I + \frac{dK_{aa}}{dx} U_I] \qquad (34)$$

Now $\frac{dg}{dx}$ can be evaluated from Eq. (34) where $\frac{ds}{dx}$ is given by Eq. (32). The major difference between the adjoint variable method and the direct method is that instead of solving Eq. (29) for $\frac{dU_I}{dx}$, one solves Eq. (33) for Λ. For large systems, the solution process for these equations is the major computational cost in the derivative calculation. Because Eq. (29) depends only on the design variable x and Eq. (33) on the constraint g, the use of the adjoint method is preferred when the number of design variables is larger than the number of constraints. The direct method is better when the number of constraints is larger than the number of design variables.

All the design cases considered in the present work involved more design variables than the number of constraints. Therefore, utilization of the adjoint variable technique is favored. For the implementation of the technique, note that the vector Z is sparsely populated because the only displacements that affect the SIF are the ones associated with the nodes of the crack-tip element. Those nonzero terms of the vector Z are calculated by analyzing an isolated crack-tip element, and applying a unit displacement to a single node while restraining the other nodes. The derivatives of the submatrices of the global stiffness matrix are calculated by finite differences.

The analytical sensitivity derivative formulation resulted in computational time savings of 40-60 % over finite difference calculations for problems with 3-6 design variables.

Chapter V

DESIGN STUDIES

The automated design procedure described in the
previous Chapter is used in conjunction with the failure
criteria, described in Chapters 2 and 3, for designing
plates with cracks that simulate structural damage. The
unified strain criterion [32] of Chapter 2 is used to ensure
that further propagation of a crack with fiber failures
ahead of the crack tip is prevented under tensile loadings.
For compressively loaded cracked plates, the failure model
developed in Chapter 3 is used. The compression failure
mechanism which is covered by the model is fiber kinking
that involves microbuckling of stiff fibers in a relatively
soft matrix followed by fiber breaking. This kind of
failure is observed experimentally for plates with holes and
cracks under static and cyclic loadings.

Design studies for plates loaded in tension and
compression are presented in the next two sections. The
design studies have a dual purpose. First, they demonstrate
the methodology which is described in the present work.
Second, they provide insight into the effect of using damage
tolerance constraints in the design process. No attempt has
been made within the content of this work to combine the

damage tolerance constraints for tension- and compression-loaded plates to achieve designs that are capable of handling load reversals. In each section, design studies are presented first for plates with uniform thicknesses. Next, plate designs with regions of additional thickness of material are presented. Those regions with additional thickness of material have a constant cross section along the length of the plate and are placed symmetrically with respect to the central crack, see Fig. 25. Main purpose of the thick regions is considered to be containing the crack in a controlled region and maybe providing some bending stiffness to the plates. They are referred as stiffeners in subsequent sections of this Chapter.

5.1   PLATES LOADED IN TENSION

5.1.1   Uniform Thickness Plates

Uniform thickness, 76.2 mm wide plates having length to width ratio, L/W , of 3 were designed. Three design variables which are the thicknesses of the 0°, 90°, and ±45° plies were used. For all the combinations of crack length, 2a, and load level, the optimization algorithm eliminated the 90° and ±45° plies leaving the plate with only 0° plies when the damage tolerance was the only constraint.

Considerations like transverse strength requirements and biaxial load conditions usually require significant thicknesses of 90° and ±45° plies. Also, crack-like slits in 0° unidirectional plates and plates with large amount of 0° plies fail due to matrix damage [20,31]. That is, high shear strain at the ends of the slit causes matrix cracks parallel to the fibers. The failure criterion used in this work assumes breakage of the fibers ahead of the crack-tip collinear with the crack, and therefore is not adequate for designing predominantly 0° ply plates.

To obtain more practical designs, the thickness of 0° plies was limited to certain percentage of the total thickness. With this constraint, the optimizer eliminated the 90° plies. Besides the designs obtained by the optimization procedure, plates with fixed ratios of 90° and ±45° plies were analyzed. The thicknesses of plates with such constraints are shown in Figs. 28 and 29 as a function of the percentage of 0° plies in the laminate for crack aspect ratios, 2a/W, of 0.2 and 0.6, respectively. The different curves represent different proportions of the 90° and ±45° plies. The designs in Figs. 28 and 29 were obtained for a load level of P = 122 kN, but the thicknesses may be linearly scaled for any load level. Experimental results (scaled to a load level of 122 kN) for plates with

similar proportions of 0°, ±45°, and 90° plies from Ref. [16] are included in Fig. 28 for comparison.

The thickness penalty associated with the reduction of percentage of 0° plies in the laminate is a strong function of the orientation of the plies that are used to replace 0° plies. For example, the reduction of 0° plies from 95% to 60% (see Fig. 28) causes a 60% increase in thickness for 0°/90° laminates but only an increase of about 10% for the 0°/±45° laminates. A comparison of 0°/±45° designs in Figs. 28 and 29 shows that, for larger cracks, the thickness increases faster as the amount of 0° plies is reduced. For the 0°/90° designs, the increase in thickness, compared to the optimum design, due to the reduction in 0° plies, though large, is not sensitive to the crack aspect ratio.

As an example of a requirement which may call for 90° or ±45° plies, a shear load of magnitude of 20% of the axial load was assumed to act on the plate. It was assumed that the structure has to carry the combined load when it is undamaged. The Tsai-Hill failure criterion was used for the stress constraints with stress allowables typical of graphite/epoxy. The resulting design, indicated by a filled triangle in Figs. 28 and 29, favours a laminate with a 0° and ±45° ply combination similar to that of an $[0_6/±45]$ layup for the crack aspect ratio of 0.2. For a crack aspect

ratio of 0.4 we have a combination similar to that of an $[0_{11}/\pm45]$ layup. Further increases in the crack length make the stress intensity factor highly critical and pushes the designs to have more and more $0°$ plies.

The dependence of the thickness of designs on the crack aspect ratio is given in Fig. 30 for a plate with a combination of $0°$, $\pm45°$, and $90°$ plies similar to that of an $[0_2/\pm45/0_2/90/0]_S$ layup. Experimental results [16] for uncracked plates and plates with different crack lengths are also indicated in the figure by open squares.

5.1.2 Stiffened Plates

Stiffeners perfectly bonded to the plate symmetrically with respect to the crack, and composed of a flange and a blade section were used (see Fig. 25). Both the flange and the blade were considered to have $0°$, $\pm45°$, and $90°$ plies. Although cracks entering the flanges can be used to model a partly damaged stiffener, results presented in this section include only a mid-bay panel crack running from one stiffener flange to the adjacent flange. When the fracture constraint is the only constraint, the thicknesses of plies in the panel section were reduced to their minimum gage values, so that the load was carried mostly by stiffeners.

Having a very thin panel section is undesirable because of two reasons. First, stiffened plates used in aircraft structures are often subject to load reversal and must be designed to resist some compressive loads. Stiffened plates with thin panel sections might fail prematurely due to local buckling. Second, plates designed to carry the applied loads mostly by the stiffeners can fail catastrophically due to stiffener damage. To prevent thin panel sections, stress constraints with additional shear loading or increased lower bounds on the design variables were used (constraining the amount of material in the panel section to be a certain fraction of the total material of the plate was also another possibility).

With these additional constraints, the panel sections had more $\pm 45°$ plies than $0°$ plies, and no $90°$ plies. Also, the blade part of the stiffeners was eliminated and the flange was left with $0°$ plies only. The preference for more $\pm 45°$ plies than $0°$ plies in the panel section may be explained by the displacement patterns of loaded plates. For panel sections with predominantly $0°$ plies, additional crack opening is observed due to a Poisson's effect. Because of the low stiffness of the panel section in the lateral direction, the stiffeners are pulled in at the section along the crack line resulting in a reduced

restraining effect of the stiffeners on the crack opening. The ±45° plies provide the necessary lateral stiffness and (unlike 90° plies) contribute also to the longitudinal stiffness of the panel.

Plate designs with two edge stiffeners without the blade are given in Fig. 31 for a varying stiffener width. The total width of the plates was kept constant at 76.2 mm. as the stiffener width was varied. The cracked plate was designed to carry an axial load of P = 122 kN. As done for some of the unstiffened plate designs, a shear load of magnitude 20% of the axial load was applied, and the panel was required to carry the combined loading when undamaged. Laminates with only 0° and ±45° layers were used for the panel section, and the stiffeners were made up of only 0° plies. Three design variables, which are the thicknesses of afore mentioned plies, were used. The resulting designs indicated a minimal effect of stiffener width on the weight (proportional to total area) of the plate, with a slight decrease in area for increasing stiffener width.

Similar results are also obtained for plates with four stiffeners, two on each side of the crack compared to one in the previous case, designed under similar loading conditions and with a same set of design variables. But when the 0° plies are removed from the panel section and the orientation

of the angle plies, ±θ from the x axis, used as a design
variable, a somewhat stronger effect of the stiffener width
on the weight of the plate is observed. Results for such
plate designs are shown in Fig. 32 for axial load of 600 kN
and no shear loading. Also, no stress constraints are used,
but the thickness of angle plies (referred as ±θ plies from
now on) is set to a constant value of 1.12 mm to prevent the
panel section from being eliminated by the optimizer. As
was the case in the previous set of results shown in Fig.
31, the crack is assumed to run from one stiffener to the
other, but only in the middle panel section of the plate.
For some values of the total strip width to plate width
ratios, i.e. % strip width, two designs are presented in the
figure. They are obtained by using two different finite
element meshes for the same plate geometry (the ones with a
larger cross sectional area are obtained by using a refined
mesh). The dashed line shows the decreasing trend of the
weight as the stiffener width is increased. For all the
designs, the value of optimum angular orientation of the
panel section are obtained to be between 45° and 50° without
any obvious trend.

The effect of changing the angular orientation of the
±θ plies of the panel section on the weight of the plate is
shown in Fig. 33 for a plate with stiffener width of 22.5

mm, and spacing of 77.5 mm (which gives a total stiffener width to plate width ratio of about 0.35). The three different symbols are for three different values of the total plate width to plate length ratios. Minimum plate weights are achieved for panel angles of 45°-55° regardless of the plate aspect ratio, W/L. For panel angular orientations greater than 40%, the weight of the plate seem to be insensitive to the plate aspect ratio, and is almost constant. Using angles smaller than 40° introduces large weight penalties which are higher for long plates than short plates.

For the design examples of Fig. 33, only ±θ° plies with a total thickness of 1.12 mm are used in the panel section of the plate. The trend of the weight changes significantly if a portion of those ±θ° plies is replaced by 0° plies. Designs shown in Fig. 34 are obtained by replacing 25% of the ±θ° plies in the panel used in the previous figure by 0° plies. Minimum plate weights are achieved for an orientation range of about 30°-50° for the angle-ply laminates. But, the minimum weight for this combination of 0° and ±θ° plies in the panel section is 30% heavier than the all ±θ° panel section with same total thickness. Moreover, for panel angles greater than 50°, there is a large increase in the plate weight as opposed to previous examples where the weight remained almost constant.

If, for some reason, it is important to keep a certain amount of 0° plies in the panel section regardless of the additional thickness of the ±θ° plies, depending on the amount of 0° plies that we want to preserve in the panel, additional thickness of angle plies may or may not improve the total weight. The three horizontal lines in Fig. 35 indicate three designs with only 0° plies in the panel section for a plate with the same planar geometry as the ones used in Figs. 33 and 34. From the lower to upper lines they have 0.28, 0.56, and 1.12 mm of 0° plies in the panel section. Designs obtained by allowing additional thickness of ±θ° plies in the panel section are indicated by open symbols. When angle-ply laminates with less than 15° or greater than 60° plies are included in the design, they are eliminated by the program, leaving the panel section with only 0° plies. Adding 0.51 mm of ±36° plies to the 0.28 mm panel improved the weight 15% by decreasing the stiffener thickness from 11.02 mm to 7.82 mm. But, for the 1.12 mm thick 0° panel, adding 0.42 mm of ±38° plies reduced the weight only 3%.

As mentioned previously, buckling may also be a consideration in the design of aircraft plates. Buckling resistant plates do require stiffeners with deep blades. Such designs can be achieved by imposing a blade with

specified width and thickness and redesigning the plates with this new geometry. A blade width of 5 mm composed of only 0° plies was used for this purpose. A plate with four stiffeners was utilized. The stiffener flange widths were 30 mm, and they were spaced 75 mm apart from each other. The plate was designed to carry an axial load of 600 kN. A minimum gage thickness of 0.28 mm was used for all plies. The minimum weight design without the blades had a total cross sectional area of 892 mm². The weight penalty due to the blades for various blade heights is shown in Fig. 36 The cross sections of the half plate without the blades and the cross sections of the stiffeners for some blade stiffened designs are also shown in the figure. Significant blade heights are possible with less than a 15% weight penalty. This provides considerable flexibility for the designer.

5.2   PLATES LOADED IN COMPRESSION

5.2.1   Uniform Thickness Plates

Plates 127 mm wide and with a length to width ratio, L/W, of 2 were designed using the compression failure criterion developed in Chapter 3. Three design variables which are the thicknesses of the 0°, 90°, and ±45° plies were used to find the minimum weight design for a given

crack length and load level. For all the combinations of crack length and load level considered, the optimization algorithm eliminated the 90° plies. In contrast to the tension case however, minimum weight designs consisted of combination of a 0° and ±45° plies. For a plate with a crack aspect ratio of 2a/W = 0.1 under 500 kN of compression, for example, 51% of the total thickness (t_{tot}= 9.52 mm) was 0° plies. Changing the crack aspect ratio altered the optimum ratio of 0° to ±45° plies only slightly. As the crack aspect ratio increased, the percentage of 0° plies decreased steadily. For a crack aspect ratio of 0.8, the percentage of 0° plies was 45% of the total thickness.

When plates were designed with only 0° and 90° plies, a higher value for the optimum percentage of 0° plies, compared to the percentage of 0° plies for 0°/±45° combination, was obtained. For a crack aspect ratio of 0.1, 78% of the total thickness (t_{tot}= 9.91 mm) was 0° plies. The optimum ratio of 0° to 90° plies was again insensitive to crack aspect ratio.

The total thicknesses of designs with 0°/±45° and 0°/90° ply combinations are given in Fig. 37 as the crack aspect ratio changes. As in the case of plates under tension, there is a significant increase in the total

thickness of the plates with increasing crack aspect ratio. However, the increase is not as steep as in the tension case. For example, increasing the crack aspect ratio from 0.2 to 0.6 increased the thickness by 90% for compression plates with 0°/±45° plies, see Fig. 37, whereas for similar plates under tension (with the same percentage of 0° and ±45° plies) the increase was 120%.

In order to understand the effect of using combinations of non-optimum ply thicknesses on the weight, plates with various fixed proportions of 0°, ±45°, and 90° plies are presented in Figs. 38 and 39 for crack aspect ratios of 0.2 and 0.4. The designs in Figs. 38 and 39 were obtained for a load level of P = 500 kN, but the thickness may be linearly scaled for any load level. Three curves in each of the Figs. 38 and 39 are, from top to bottom, for 0°/90°, 0°/±45°/90° with t(±45°)=2*t(90°), and 0°/±45° ply combinations. The optimum design for each of the three groups is indicated by a solid circular mark on appropriate symbol in the figures. No stress constraints were used for the designs in Figs. 38 and 39. However, the optimum design for each of the three ply combinations was checked and did not prove to be stress critical.

The optimum plate design with the 0°/±45°/90° ply combination was 25% thicker than the optimum plate design

with the 0°/±45° ply combination for both crack aspect
ratios.   Eliminating the ±45° plies increased the thickness
penalty significantly.   The optimum design for the 0°/90°
plate was 85% thicker for both crack aspect ratios than the
0°/±45° plate, Figs. 38 and 39.   Increasing or decreasing
the percentage of 0° plies from their optimum value also
caused significant thickness penalties.   For example,
decreasing the percent of the 0° plies in the 0°/90°
laminate from 79% (optimum value) to 20% increased the total
thickness by 70%.   The thickness of the plate with 100% 0°
plies was twice the thickness of the optimum 0°/±45° plate
design.   Note that for the plate designs with the tension
fracture constraint, 100% 0° ply designs were always the
optimum designs, see Figs. 28 and 29.   Also comparison of
Figs. 38 and 39 indicated that, in contrast to tension-
loaded plates, changing the crack aspect ratio did not
affect the thickness penalty associated with non-optimum ply
thickness combinations.

When the effect of shearing forces ahead of the crack
tip was excluded, the design trends changed completely.
Designs obtained by using three different approaches for
plates with only 0°/±45° ply combinations are given in Fig.
40 for comparison.   The curve indicated by asterisks is
taken from Fig. 38 and was obtained by using the model

developed in this work. The other two curves do not include the effect of shearing force. The one indicated by square symbols was obtained using Rosen's microbuckling model at a point r = 0.05 mm away from the crack tip. The other curve, indicated by triangular symbols, was obtained by using the point-strain criterion with a 1.4% ultimate strain of the fibers at a distance r = 2.0 mm from the crack tip. The distance r for this latter model was obtained as a best fit to experimental results for quasi-isotropic plates. The plate designs obtained by using the models that do not include the effect of the shearing force indicated a behavior similar to the plates designed for tensile loads. The optimum design is the one with 100% 0° plies and is 70% thinner compared to the design obtained by the present model. This result seems implausible because it is experimentally observed [83] that plates with all 0° plies do not have a good compressive behavior. Even if the actual failure mode observed for all 0° plates may be different than the shear crippling failure mode assumed in the present model, the present model can successfully eliminate such unrealistic designs.

5.2.2 Stiffened Plates

Plates having the same external size as the unstiffened plate designs presented in the previous section are considered. Four 12.7 mm wide stiffeners placed symmetrically with respect to the central crack (two on each side) were included. The crack runs from one stiffener to the adjacent stiffener in the mid-bay panel which produces a crack length to total plate with ratio of 0.2. Six design variables which are the thicknesses of 0°, ±45°, and 90° plies in the panel section, and additional thicknesses of similar plies in the stiffeners were used. When the crack tip fiber kinking constraint is the only constraint, the plies in the panel section were eliminated, and the resulting plate had stiffeners with only 0° plies. When the Tsai-Hill stress constraints were used, a 0.21 mm thick panel section was obtained with mostly 0° plies. Stiffeners were all 0° plies, and the ratio of the thickness of the stiffeners to the total thickness (stiffener thickness plus the panel thickness) was 98%. This design had a total cross-sectional area (560 mm²) less than half of the unstiffened optimum plate with 0°/±45° plies (1200mm²) with the same crack aspect ratio.

Having a very thin panel section is undesirable because stiffened plates with thin panel sections might fail

prematurely due to local buckling of the panels. One easy way to obtain thicker panel sections is to constrain the amounts of material in the panel and the stiffener sections. Designs obtained by using an upper bound on the stiffener thickness that may be allowed are given in Fig. 41. Fig. 41 shows the ratio of the total cross-sectional area of the stiffened plate to the cross-sectional area of the unstiffened plate with same dimensions and crack length versus the ratio of the stiffener thickness to the total plate thickness. Using an upper bound of 8 mm on the stiffener thickness, the optimum design is obtained to have a panel tickness of 2.27 mm (of which 1.19 mm was 0° plies and 1.08 mm was ±45° plies) which gives a stiffener thickness to total thickness ratio of 0.78. The stiffened design was some 43% lighter than the unstiffened plate and was checked to be free of panel buckling. The rightmost design point in Fig. 41 is the one obtained in the previous paragraph by using stress constraints and proved to have a buckling critical panel section.

Plate designs with four stiffeners without blades are given in Fig. 42 for a varying stiffener width. The total width of the plates was kept constant, 255 mm., as the stiffener width was varied. The plate was designed to carry an axial load of P = 500 kN. As done for some tension

design cases, a shear load of magnitude 20% of the axial load was applied, and the panel was assumed to carry the combined loading when undamaged. Laminates with only 0° and ±45° layers were used for the panel section, and the stiffeners were made up of only 0° plies. As in the case of stiffened plate designs under tension in Fig. 31, the resulting designs indicated a minimal effect of stiffener width on the weight of the plate, with a slight decrease in area for increasing stiffener width.

Designs with deep blades are achieved, as done before for tension case, by imposing a blade with specified width and height and redesigning the plate with this new geometry. A blade width of 5 mm composed of only 0° plies was used for this purpose. A plate design with flange widths of 30 mm and spaced 75 mm apart from each other is used from the previous figure. The plate was designed to carry an axial load of 500 kN. A minimum gage thickness of 0.28 mm was used for all plies. The minimum weight design without the blades had a total cross sectional area of 881 mm². The weight penalty due to the blades for various blade thicknesses is shown in Fig. 43. The cross sections of the half plate without the blades and the cross sections of the stiffeners for some blade stiffened designs are also shown in the figure. It is observed that the weight penalty due

to blade height is small, even smaller than the penalty in the tension case.

Chapter VI

CONCLUDING REMARKS

An optimization procedure for designing stiffened composite plates subject to a local damage constraint under tensile and compressive loadings has been developed. A centrally located, through-the-thickness crack was used to simulate the damage condition. For tension-loaded plates, failure was characterized by the propagation of the crack with tensile fiber failures.

Results of an experimental study conducted to evaluate the effect of slots (simulated cracks) on the buckling response, the postbuckling response, and the failure characteristics of flat rectangular graphite/epoxy plates loaded in compression were presented. Centrally located slots did not affect the failure loads or failure modes of the buckling-critical plates. Therefore, attention was focused on the failure of cracked strength-critical plates. A fiber kinking mechanism is assumed to be responsible for the failure of such plates. An analytical failure model for the kinking mechanism was developed. The model was based on microbuckling followed by breaking of the fibers under combined compressive and shear stresses.

A finite element program based on linear elastic fracture mechanics for calculating the stress intensity factor(SIF) at the crack tip was incorporated in the design cycle. Only symmetric balanced laminated plates under symmetric loading were considered. Values of the critical stress intensity factor, which was used as a measure of the fracture toughness, under tensile loadings were calculated by using a unified strain criterion due to Poe. Values of the critical stress intensity factor for compressive plates were based on the model developed.

Weight minimizations were performed by general purpose mathematical optimization programs, NEWSUMT and NEWSUMT-A, based on the extended interior penalty function approach. An automatic mesh generator was used to generate finite element models of the plates during the design process. The computational efficiency of the optimization procedure was improved by utilizing analytical sensitivity derivatives. The adjoint variable technique, modified to handle the static test loading boundary conditions, was used for that purpose.

Unstiffened plate designs loaded in tension tended to have only 0° plies in the laminate regardless of the crack length. More realistic designs were obtained by imposing restrictions on the relative amounts of various ply

orientations or using stress constraints. Stiffened plate designs tended to eliminate the panel section. Using stress constraints or minimum thickness constraints for the panel section resulted in designs with mostly ±45° plies in the panel section and only 0° plies in the stiffener flange eliminating the blades of the stiffeners. But addition of significant blade thicknesses was possible without a considerable weight penalty.

Unstiffened plate designs loaded in compression eliminated only the 90° plies in the laminate. But, there was an optimum thickness of 0° plies and ±45° plies. When 90° plies were forced into the design, a higher value of the optimum 0° ply thickness with respect to the total thickness was obtained together with increased plate weight. The optimum thickness of the 0° plies was seem to be insensitive to crack aspect ratio.

REFERENCES

1. Davis, G. W., and Sakata, I. F., "Design Considerations For Composite Fuselage Structure of Commercial Transport Aircraft," NASA CR-159296, March, 1981.

2. Dickson, J. N., and Biggers, S. B., "Design and Analysis of a Stiffened Composite Fuselage Panel," NASA CR-159302, August, 1980.

3. Rhodes, M. D., Williams, J. G., and Starnes, J. H., Jr., "Low Velocity Impact Damage in Graphite Fiber Reinforced Epoxy Laminates," Proceedings of the 34th Annual Conference of Reinforced Plastics/Composites Institute, The Society of the Plastics Industry, Inc., New Orleans, Louisiana, January 29 - February 2, 1975.

4. Sharma, A. V., "Low-Velocity Impact Tests on Fibrous Composite Sandwich Structures." Test Methods and Design Allowables for Fibrous Composites, ASTM STP 734, C. C. Chamis, Ed., American Society for Testing and Materials, 1981, pp. 54-70.

5. Arora, J. S., Haskell, D. F., and Govil, A. K., "Optimal Design of Large Structures for Damage Tolerance," AIAA Journal, Vol. 18, May 1980, pp. 563-570.

6. Starnes, J. H. Jr., and Haftka, R. T., "Preliminary Design of Composite Wing-Box Structures for Global Damage Tolerance," AIAA Paper 80-0755, presented at the AIAA/ASME/ASCE/AHS 21st Structures, Structural Dynamics and Materials Conference, Seattle, Washington, May 1980.

7. Haftka, R. T., Starnes, J. H. Jr., and Nair, S., "Design for Global Damage Tolerance and Associated Mass Penalties," Journal of Aircraft, Vol. 20, No. 1, January 1983, pp. 83-88.

8. Combes, R. C., Jr., "Design for Damage Tolerance," Journal of Aircraft, Vol. 7, No. 1, January-February 1970, pp. 18-20.

9. Toor, P.M., "A Review of Some Damage Tolerance Design Approaches for Aircraft Structures," Engineering Fracture Mechanics, Vol. 5, 1973, pp. 837-880.

10. Poe, C.C., Jr., "Stress-Intensity Factor for a Cracked Sheet With Riveted and Uniformly Spaced Stringers," NASA TR R-358, May 1971.

11. Kruse, G. S., "An Automated Procedure for Preliminary Design of Primary Structure for Transport Aircraft," ASME 76-WA/Aero-9, American Society of Mechanical Engineers, 1976.

12. Davis, C. S., "Automated Design of Stiffened Panels Against Crack Growth and Fracture Among Other Design Constraints," Flaw Growth and Fracture, ASTM STP 631, American Society for Testing and Materials, 1977, pp. 416-445.

13. Dobbs, M. W., and Nelson, R. B., "Minimum Weight Design of Stiffened Panels with Fracture Constraints," Computers & Structures, Vol. 8, No. 6, 1978, pp. 753-759.

14. Rhodes, M. D., "Damage Tolerance Research on Composite Compression Panels." Selected NASA Research in Composite Materials and Structures, NASA Conference Publication 2142, August 11-13, 1980, pp. 107-142.

15. Poe, C. C. Jr., and Kennedy, J. M., "Assessment of Buffer Strips for Improving Damage Tolerance of Composite Laminates." Journal of Composite Materials Supplement, Vol. 12, 1980, pp. 57-70.

16. Chu, C. S., and Freyre, O. L., "Failure Stress Correlation of Composite Laminates Containing a Crack," Journal of Aircraft, Vol. 19, No. 2, 1980.

17. Olster, E. F., and Roy, P. A., "Tolerance of Advanced Composites to Ballistic Damage," Composite Materials: Testing and Design, ASTM STP 546, American Society for Testing and Materials, 1974, pp. 583-603.

18. Dorey, G., Sidey, G. R., and Hutchings, J., "Impact Properties of Carbon Fibre/Kevlar 49 Fibre Hybrid Composites," Composites, January 1978, pp. 25-32.

19. Avery, J. G., Bradley, S. J., and King, K. M., "Fracture Control in Ballistic-Damaged Graphite/Epoxy Wing Structure," Fracture Mechanics: Thirteenth Conference, ASTM STP 743, Richard Roberts, Ed., American Society for Testing and Materials, 1981, pp. 338-359.

20. Dorey, G., "Fracture of Composites and Damage Tolerance," Practical Considerations of Design, Fabrication and Tests For Composite Materials: AGARD-LS-124, September 1982, paper 6.

21. Wu, E. M., "Application of Fracture Mechanics to Anisotropic Plates," Journal of Applied Mechanics, December 1967, pp. 967-974.

22. Waddoups, M. E., Eisenmann, J. R., and Kaminski, B. E., "Macroscopic Fracture Mechanics of Advanced Composite Materials," Journal of Composite Materials, Vol. 5, October 1971, pp. 446-454.

23. Whitney, J. M., and Nuismer, R. J., "Stress Fracture Criteria for Laminated Composites Containing Stress Concentrations," Journal of Composite Materials, Vol. 8, July 1974, pp. 253-265.

24. Zweben, C., "Fracture Mechanics and Composite Materials: A Critical Analysis," Analysis of the Test Methods for High Modulus Fibers and Composites, ASTM STP 521, American Society for Testing and Materials, 1973, pp. 65-97.

25. Rosen, B. W., Kulkarni, S. V., and McLaughlin, P. V., Jr., "Failure and Fatigue Mechanisms in Composite Materials," Inelastic Behavior of Composite Materials, AMD Vol. 13, American Society of Mechanical Engineers, 1975, pp. 17-72.

26. Hedgepeth, J. M., and Van Dyke, P., "Local Stress Concentrations in Imperfect Filamentary Composite Materials," Journal of Composite Materials, Vol. 1, No. 3, 1967, pp. 294-309.

27. Tsai, S. W., and Hahn, H. T., "Recent Developments in Fracture of Filamentary Composites," Proceedings of an International Conference on: Prospects of Fracture Mechanics, Eds. Sih, G. C., van Elst, H. C., and Broek, D., June 1974, pp. 493-508.

28. Kanninen, M. F., Rybicki, E. F., and Brinson, H. F., "A Critical Look at Current Applications of Fracture Mechanics to the Failure of Fibre-Reinforced Composites," Composites, January 1977, pp. 17-22.

29. Yeow, Y. T., Morris, D. H., and Brinson, H. F., "A Correlative Study Between Analysis and Experiment on the Fracture Behavior of Graphite/Epoxy Composites," Journal of Testing and Evaluation, Vol. 7, No. 2, 1979, pp. 117-125.

30. Tirosh, J., Mast, P., Beaubien, L., Mulville, D., Sutton, S., and Wolock, I., "Fracture Criteria of Fibrous Laminated Composites Under In-Plane Multidirectional Loading," Journal of Applied Mechanics, Vol. 47, September 1980, pp. 563-569.

31. Poe, C. C., Jr., and Sova, J. A., "Fracture Toughness of Boron/Aluminum Laminates with Various Proportions of 0° and ±45° Plies," NASA TP-1707, 1980.

32. Poe, C. C., Jr., "A Unifying Strain Criterion for Fracture of Fibrous Composite Laminates," Engineering Fracture Mechanics, Vol. 17, No. 2, 1983, pp. 153-171.

33. Chu, C. S., et al, "Finite Element Computer Program to Analyze Cracked Orthotropic Sheets," NASA CR-2698, July, 1976.

34. Knauss, J. F., Starnes, J. H., Jr., and Henneke, E. G., II, "The Compressive Failure of Graphite/Epoxy Plates with Circular Holes," VPI-E-78-5, Interim Report Number 11, NASA-VPI&SU Composites Program NASA Grant NGR 47-004-129, February 1978.

35. Starnes, J. H., Jr., Rhodes, M. D. and Williams, J. G., "Effect of Impact Damage and Holes on the Compressive Strength of a Graphite/Epoxy Laminate," Non Destructive Evaluation and Flaw Criticality for Composite Materials, ASTM STP 696, R. B. Pipes, Ed., Amer. Society of Testing and Materials. 1979, pp. 145-171.

36. Starnes, J. H., Jr., and Williams, J. G., "Failure Characteristics of Graphite-Epoxy Structural Components Loaded in Compression," In Mechanics of Composite Materials, Recent Advances, Proceedings of the 1st IUTAM Symposium on Mechanics of Composite Materials, Held at Blacksburg, VA, August 16-19, 1982, Z. Hashin and C. T. Herakovich, Eds., Pergamon Press Inc., 1983, pp. 283-306.

37. Chan, D. P., "An Analytical Study of the Postbuckling of Laminated, Anisotropic Plates," Ph.D. Thesis, Case Western Reserve University, 1971.

38. Turvey, G. J., and Wittrick, W. H., "The Large Deflection and Postbuckling Behaviour of Some Laminated Plates," _Aeronautical Quarterly_, Vol. 24, 1973, pp. 77-84.

39. Harris, G. Z., "Buckling and Post-Buckling of Orthotropic Laminated Plates," AIAA Paper No. 75-813, 1975.

40. Harris, G. Z., "The Buckling and Post-Buckling Behavior of Composite Plates Under Biaxial Loading," _International Journal of Mechanical Sciences_, Vol. 17, 1975, pp. 187-202.

41. Banks, W. M., "The Post Buckling Behaviour of Composite Panels," _Proceedings of the 1975 International Conference on Composite Materials_, ICCM Vol. 2, 1976, pp. 272-293.

42. Stein, M., "Postbuckling of Orthotropic Composite Plates Loaded in Compression," _AIAA Journal_, Vol. 21, No. 12, December 1983, pp. 1729-1735.

43. Arnold, R. R., and Mayers, J., "Buckling, Postbuckling, and Crippling of Materially Nonlinear Laminated Composite Plates," _Journal of Solids and Structures_, (forthcoming).

44. Spier, E. E., and Klouman, F. L., "Post Buckling Behavior of Graphite/Epoxy Laminated Plates and Channels," _Composite Materials: The Influence of Mechanics of Failure on Design_, Proceedings of the Army Symposium on Solid Mechanics, AD-A029 735, September 1976, Army Materials and Mechanics Research Center, Watertown, Massachusetts.

45. Starnes, J. H., Jr., and Rouse, M., "Postbuckling and Failure Characteristics of Selected Flat Rectangular Graphite-Epoxy Plates Loaded in Compression," Presented at the AIAA/ASME/ASCE/AHS 22nd Structures, Structural Dynamics and Materials Conference, Atlanta, Georgia, April 6-8, 1981.

46. Starnes, J. H., Jr., Knight, N. F., Jr., and Rouse, M., "Postbuckling Behavior of Selected Flat Stiffened Graphite-Epoxy Panels Loaded in Compression," Presented at the AIAA/ASME/ASCE/AHS 23rd Structures, Structural Dynamics and Materials Conference, New Orleans, Louisiana, May 10-12, 1982.

47. Rhodes, M. D., Mikulas M. M. Jr., and McGowan, P. E., "Effects of Orthotropy and Width on the Compression Strength of Graphite-Epoxy Panels with Holes." AIAA Journal, Vol. 22, No. 9, 1984, pp. 1283-1292.

48. Rosen, B. W., "Mechanics of Composite Strengthening," Fiber Composite Materials, American Society of Metals, Metals Park, Ohio, October 1964.

49. Schuerch, H., "Prediction of Compressive Strength in Uniaxial Boron Fiber-Metal Matrix Composite Materials," AIAA Journal, Vol. 4, No. 1, 1966, pp. 102-106.

50. Hayashi, T., "On the Shear Instability of Structures Caused by Compressive Load," Presented at the Joint Meeting of the American Institute of Aeronautics and Astronautics, Royal Aeronautical Society, and the Japan Society for Aeronautics and Space Science, Aircraft Design and Technology Meeting, Los Angles, California, November 1965. AIAA Paper No. 65-770.

51. Foye, R. L., "Compression Strength of Unidirectional Composites," AIAA Paper No. 66-143.

52. Lager, J. R., and June, R. R., "Compressive Strength of Boron-Epoxy Composites," Journal of Composite Materials, Vol. 3, January 1969, pp. 48-56.

53. Moncunill de Ferran, E., and Harris, B., "Compressive Strength of Polyester Resin Reinforced with Steel Wires," Journal of Composite Materials, Vol. 4, January 1970, pp. 62-72.

54. Chung, Wen-Yi, and Testa, R. B., "The Elastic Stability of Fibers in a Composite Plate," Journal of Composite Materials, Vol. 3, January 1969, pp. 58-80.

55. Herrman, L. R., and Mason, W. E., "Response of Reinforcing Wires to Compressive State of Stress," Journal of Composite Materials, Vol. 1, 1967, pp. 212-226.

56. Hanasaki, S., and Hasegawa, Y., "Compressive Strength of Unidirectional Fibrous Composites," Journal of Composite Materials, Vol. 8, July 1974, pp. 306-309.

57. Davis, J. G., Jr., "Compressive Strength of Fiber-Reinforced Composite Materials," Composite Reliability, ASTM STP 580, American Society for Testing and Materials, 1975, pp. 364-377.

58. Lanir, Y. and Fung, Y. C. B., "Fiber Composite Columns Under Compression," Journal of Composite Materials, Vol. 6, July 1972, pp. 387-401.

59. Kulkarni, S. V., Rice, J. S., and Rosen, B. W., "An Investigation of the Compressive Strength of Kevlar 49/epoxy Composites," Composites, September 1975, pp. 217-225.

60. Davis, J. G., Jr., "Compressive Strength of Lamina Reinforced and Fiber Reinforced Composite Materials," Ph.D. dissertation, Virginia Polytechnic Institute and State University, Blacksburg, VA., May 1973.

61. Greszczuk, L. B., "Compressive Strength and Failure Modes of Unidirectional Composites," Analysis of the Test Methods for High Modulus Fibers and Composites, ASTM STP 521, American Society for Testing and Materials, 1973, pp. 192-217.

62. Greszczuk, L. B., "Microbuckling of Lamina-Reinforced Composites," Composite Materials: Testing and Design (Third Conference), ASTM STP 546, American Society for Testing and Materials, 1974, pp. 5-29.

63. Argon, A. S., Fracture of Composites," Treatise on Materials Science and Technology, Academic Press, New York and London, pp. 79-114, 1972.

64. Hancox, N. L, "The Compressive Strength of Unidirectional Carbon Fibre Reinforced Plastic," Journal of Materials Science, No. 10, pp. 234-242, 1975.

65. Weaver, C. W., and Williams, J. G., "Deformation of a Carbon-epoxy Composite under Hydrostatic Pressure," Journal of Materials Science, No. 10, pp. 1323-1333, 1975.

66. Evans, A. G., and Adler, W. F., "Kinking as a Mode of Structural Degradation in Carbon Fiber Composites," Acta Metallurgica, Vol. 26, p. 725-738, 1978.

67. Hull, D., "Strength of Unidirectional Laminae: Longitudinal Compressive Strength," An Introduction to Composite Materials, Cambridge University Press, pp. 154-162, 1981.

68. Chaplin, C. R., "Compressive Fracture in Unidirectional Glass-reinforced Plastics," Journal of Materials Science, Vol. 12, pp. 347-352, 1977.

69. Berg, C. A., and Salama, M., "Fatique of Graphite Fiber-reinforced Epoxy in Compression," Fiber Science and Technology, Vol. 6, p 79, 1973.

70. Parry, T. V., and Wronski, A. S., "Kinking and Compressive Failure in Uniaxially Aligned Carbon Fibre Composite Tested Under Superposed Hydrostatic Pressure," Journal of Materials Science, Vol. 17, pp. 893-900, 1982.

71. Nuismer, R. J., and Labor, J. D., "Application of the Average Stress Failure Criterion: Part II-Compression," Journal of Composite Materials, Vol. 13, pp. 49-60, January 1979.

72. Haftka, R. T., and Starnes, J. H., Jr., "Use of Optimum Stiffness Tailoring to Improve the Compressive Strength of Composite Plates with Holes," To be presented at the AIAA/ASME/ASCE/AHS 26th Structures, Structural Dynamics, and Materials Conference, Orlando, Florida, April 1985.

73. Hahn, H. T., and Williams, J. G., "Compression Failure Mechanisms in Unidirectional Composites," NASA Technical Memorandum 85834, August 1984.

74. Chou, Tsu-Wei, and Kelly, A, "The Effect of Transverse Shear on the Longitudinal Compressive Strength of Fibre Composites," Journal of Materials Science, Vol. 15, pp. 327-331, 1980.

75. Shuart, M. J., and Williams, J. G., "Compression Failure Characteristics of ±45°-Dominated Laminates with a Circular Hole or Impact Damage," Presented at the AIAA/ASME/ASCE/AHS 25th Structures, Structural Dynamics, and Materials Conference, Palm Springs, California, May 14-16, 1984. AIAA Paper No:84-0848.

76. Sih, G. C., and Liebowitz, H., "Mathematical Theories of Brittle Fracture," Fracture, Vol. 2, pp 68-188, Ed. Liebowitz, H., Academic Press, New York, 1968.

77. Jones, R. M., <u>Mechanics of Composite Materials</u>, McGraw-Hill , 1975, pp. 94-96.

78. Miura, H., and Schmit, L. A., Jr., "NEWSUMT: A Fortran Program for Inequality Constrained Function Minimization - Users Guide," NASA-CR-159070, June 1979.

79. Grandhi, R. V., Thareja, R. R., and Haftka, R. T., "NEWSUMT-A: A General Purpose Program for Constrained Optimization using Constraint Approximations," Presented at the ASME International Computers in Engineering Conference, August 7-11, 1983, Chicago, Illinois.

80. Haftka, R. T., and Starnes J. H., Jr, "Application of a Quadratic Extended Interior Penalty Function for Structural Optimization," <u>AIAA</u> <u>Journal</u>, Vol. 14, June 1976, pp. 718-724.

81. Haug, E. J., and Arora, J. S., <u>Applied</u> <u>Optimal</u> <u>Design</u>, John Wiley and Sons, 1979.

82. Hsieh, C. C., and Arora, J. S., "Structural Design Sensitivity Analysis with General Boundary Conditions," University of Iowa Technical Report, CAD-SS-83.5, March 1983.

83. Starnes J. H., Jr, personal communication, November, 1984.

TABLES

TABLE 1

Experimental results.

Specimen	Control specimens[a]			Specimens with slots		
	Number of plies	Analytical buckling load, kN	Failure load, kN	Buckling load, kN	Number of longitudinal halfwaves	Failure load, kN
C1	24	33	102	34	2	95
C2	24	33	102	34	2	96
C3	16	9	45	9	2	48
C4	16	9	45	10	3	47
C5	24	33	102	34	2	98
S1	24	33	102	35	2	67
S2	16	18	38	20	6	39
S3	16	18	38	19	5[b]	29
S4	16	18	38	19	6	30

[a]Results for undamaged plates without holes from Reference 9.
[b]Five longitudinal halfwaves formed initially but later changed to six.

TABLE 2

Typical properties of unidirectional graphite/epoxy systems.

===

Longitudinal compression strength, GPa	1.45
Longitudinal compression modulus, GPa	131.0
Transverse modulus, GPa	13.0
Shear modulus, GPa	6.4
Poisson's ratio (major)	.38
Short beam shear strength, MPa	131.0
Fiber volume fraction	0.71
Neat resin elongation to failure	0.010
Average ply thickness, mm	0.14

===

FIGURES
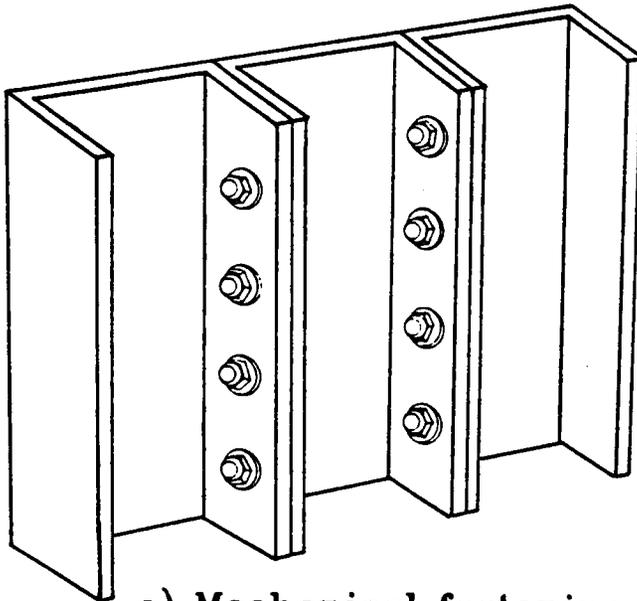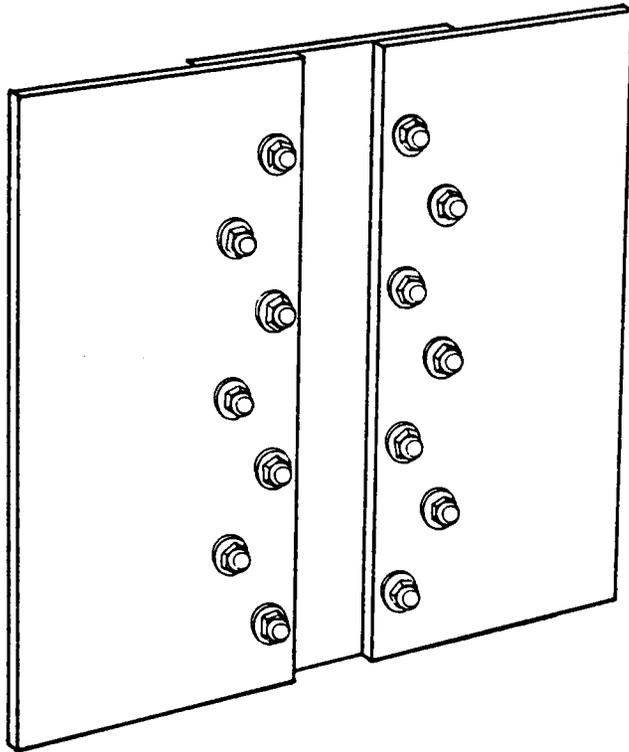
a) **Mechanical fastening**.

Figure 1: Damage tolerant structural concepts.
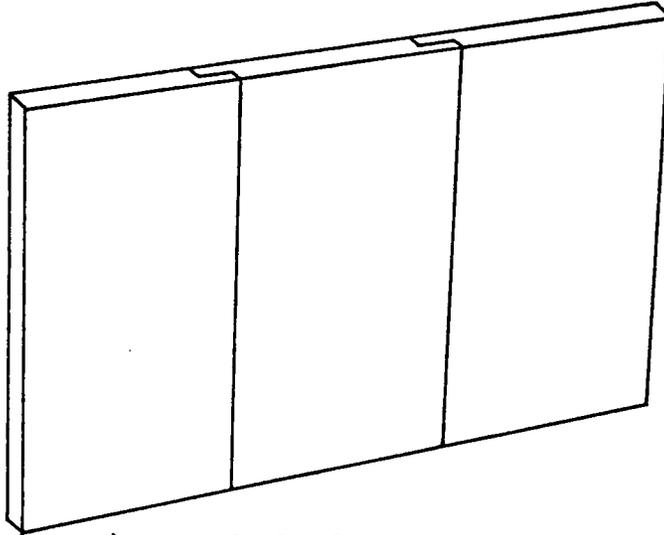
b) Bonded plate section.
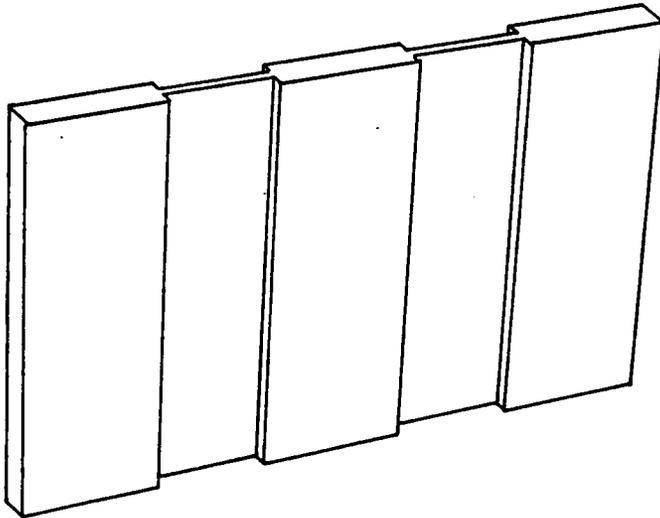
c)Discrete stiffness design.

Figure 1:   Concluded.
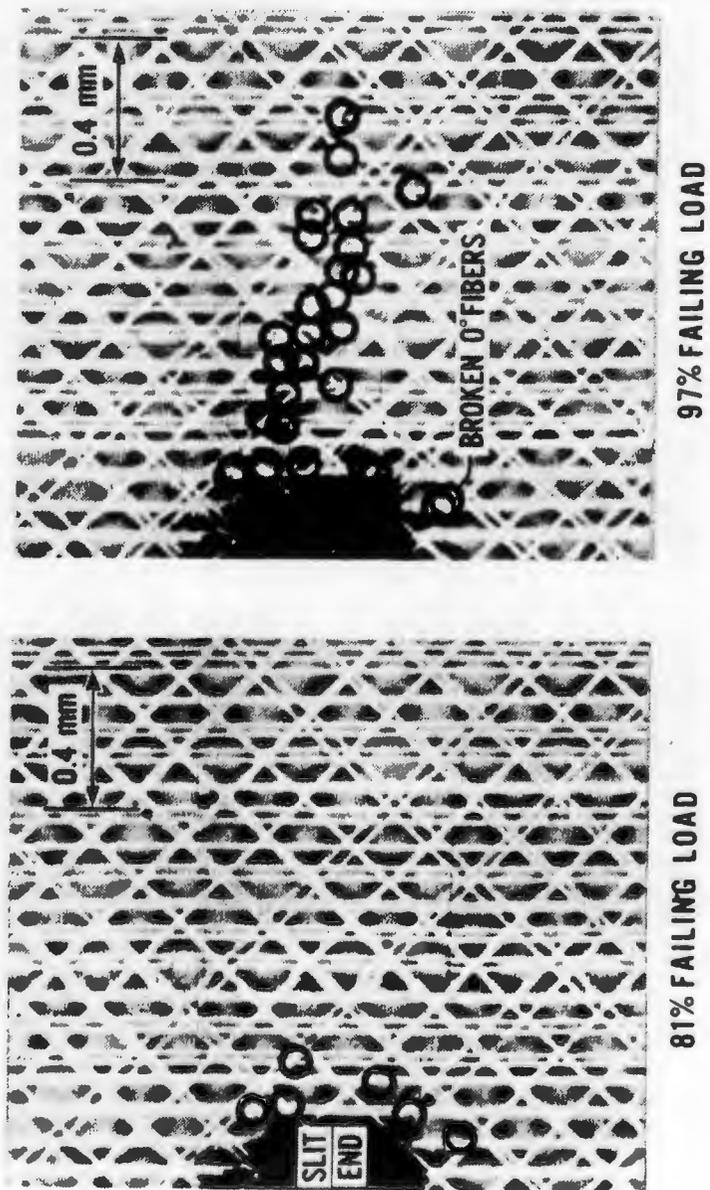
Figure 2: Broken 0° fibers at the slot tip for a $[\pm 45/0_2]_S$ Boron/Aliminum laminate, Poe [31].
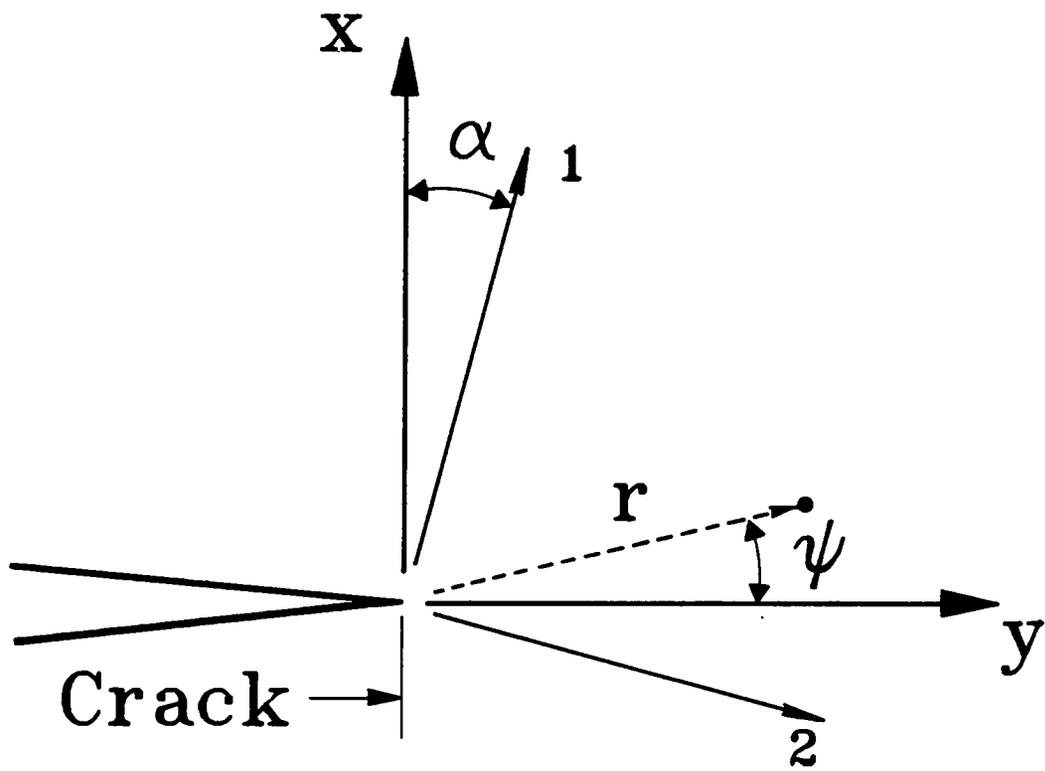
Figure 3: Crack-tip coordinates.
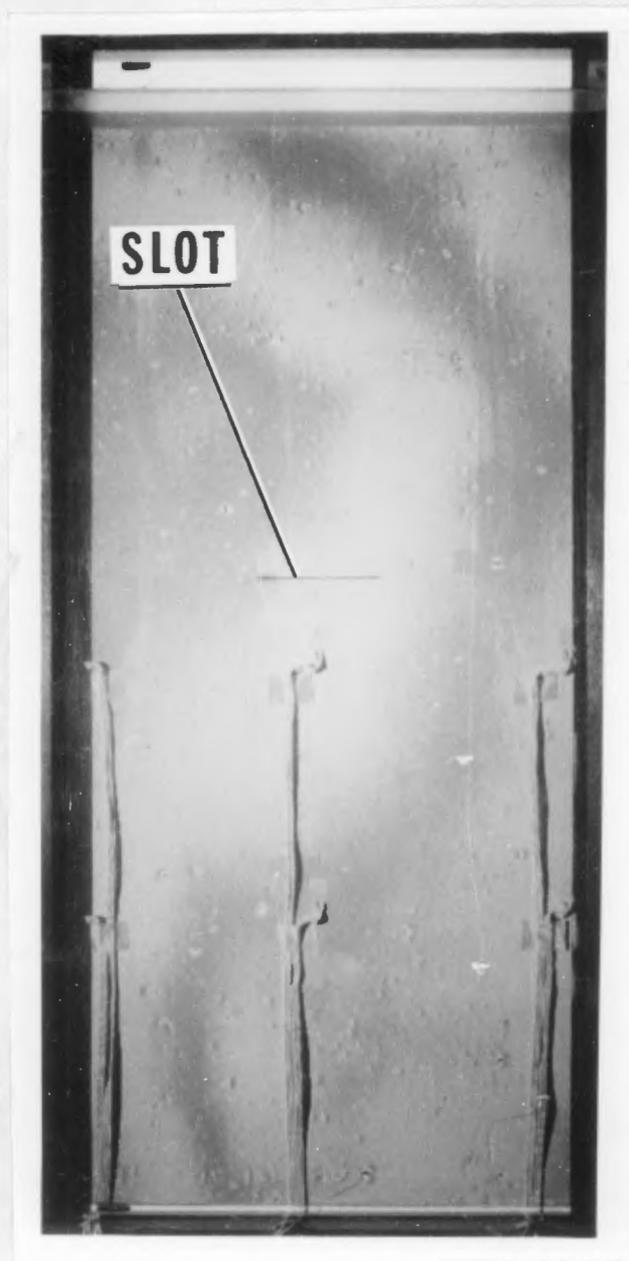
Figure 4: Typical test specimen.
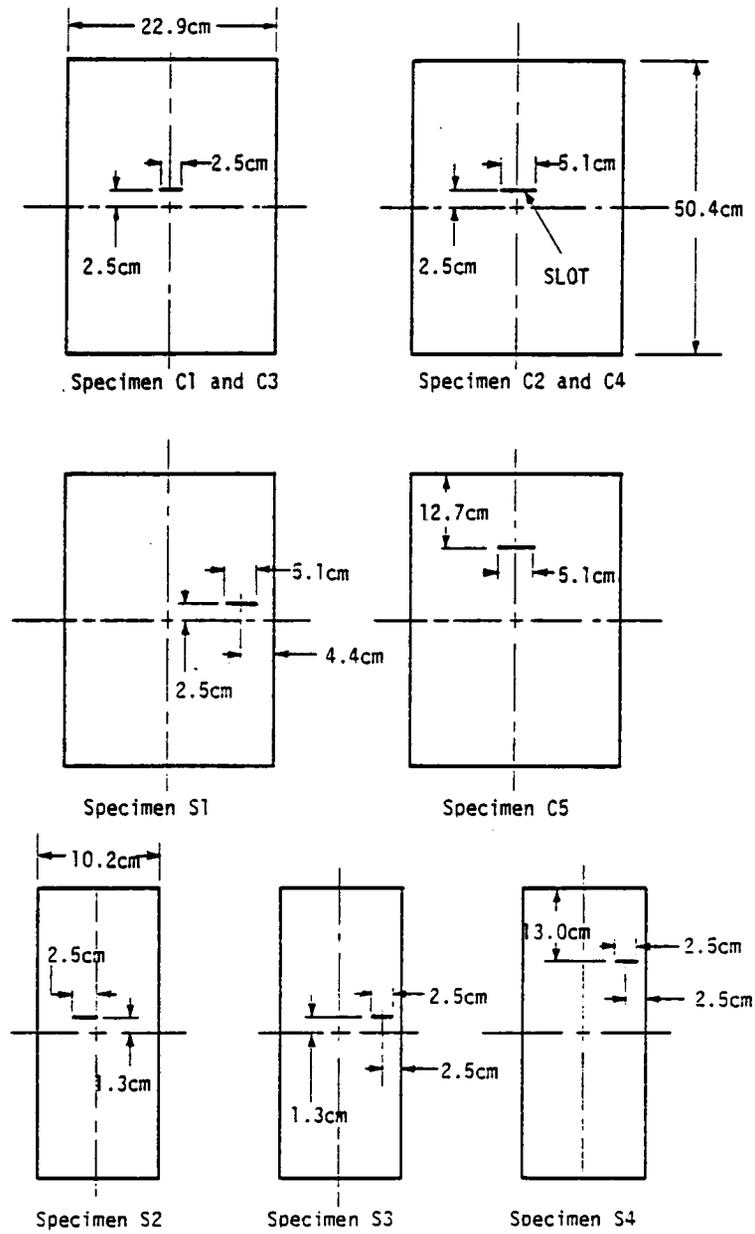
Figure 5: Slot locations.
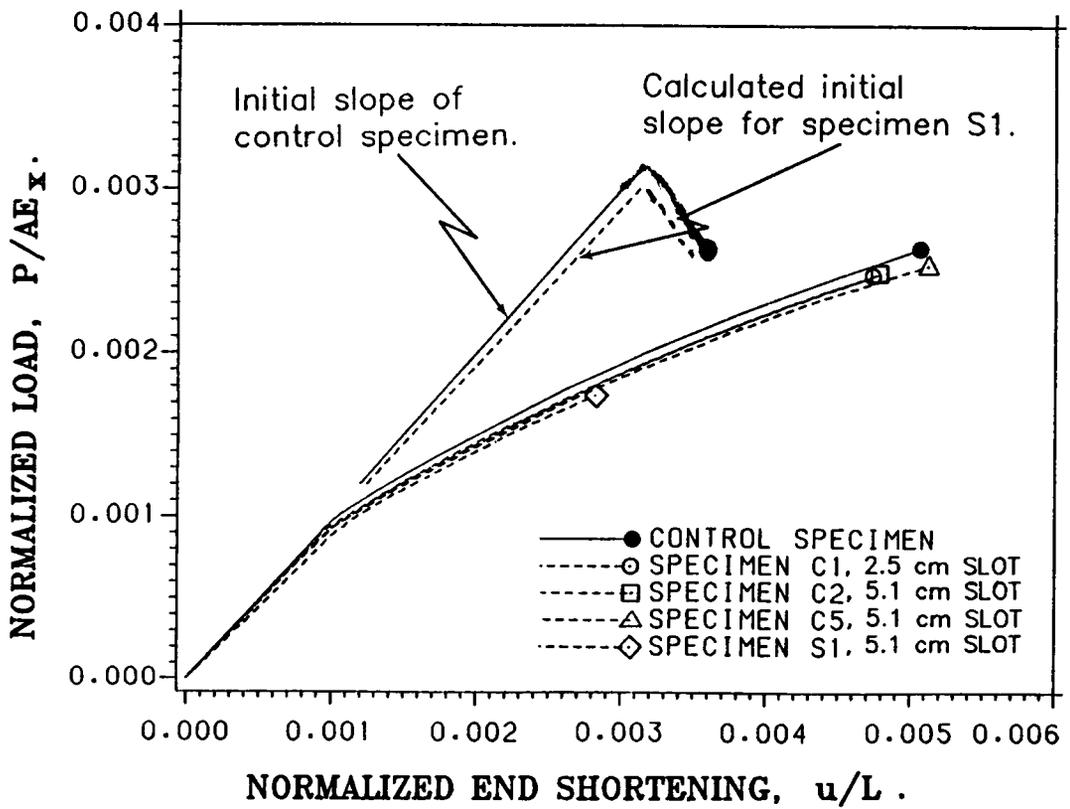
Figure 6:   Load shortening responses of the 24-ply plates.
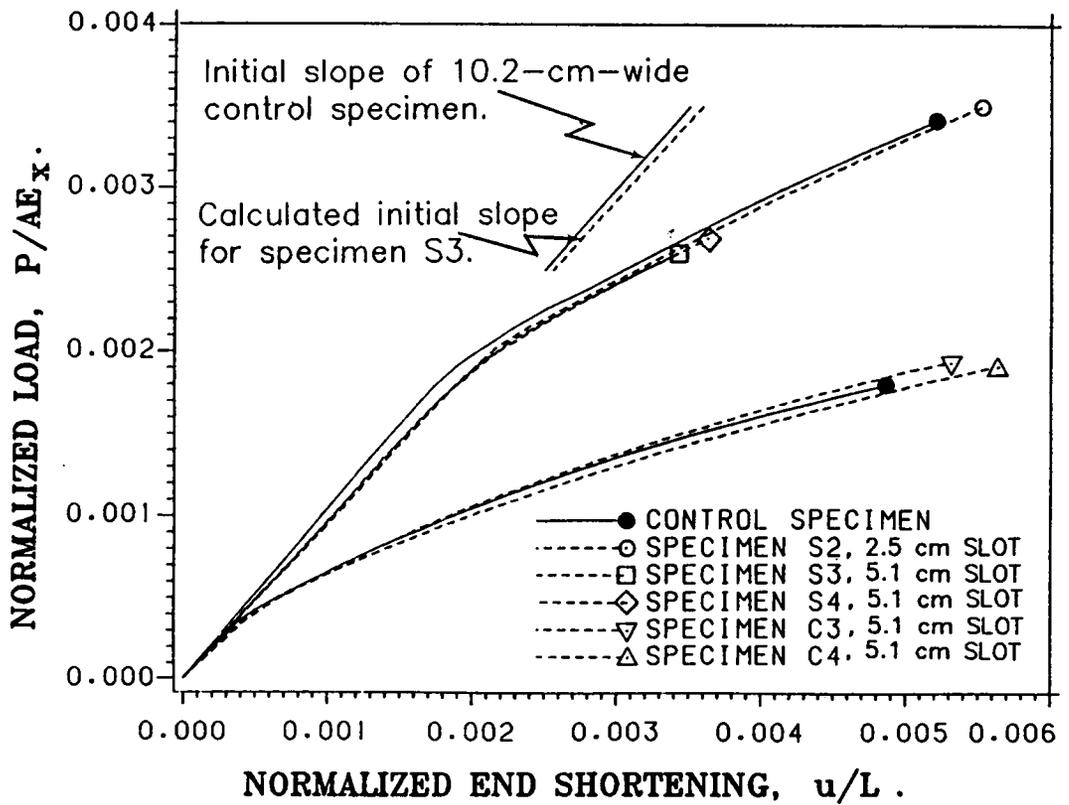
Figure 7: Load shortening responses of the 16-ply plates.
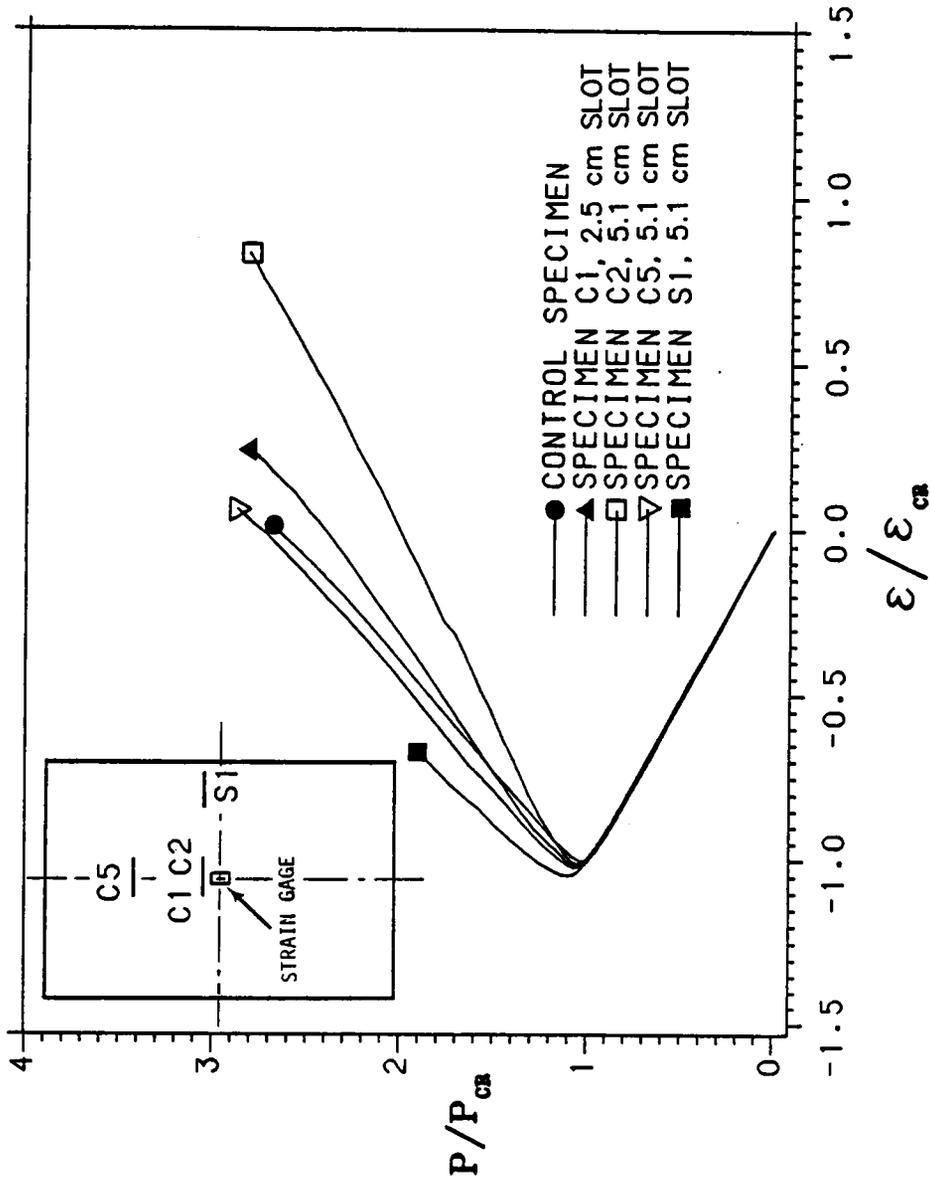
Figure 8: Postbuckling membrane strains at the plate center for 24-ply specimens.
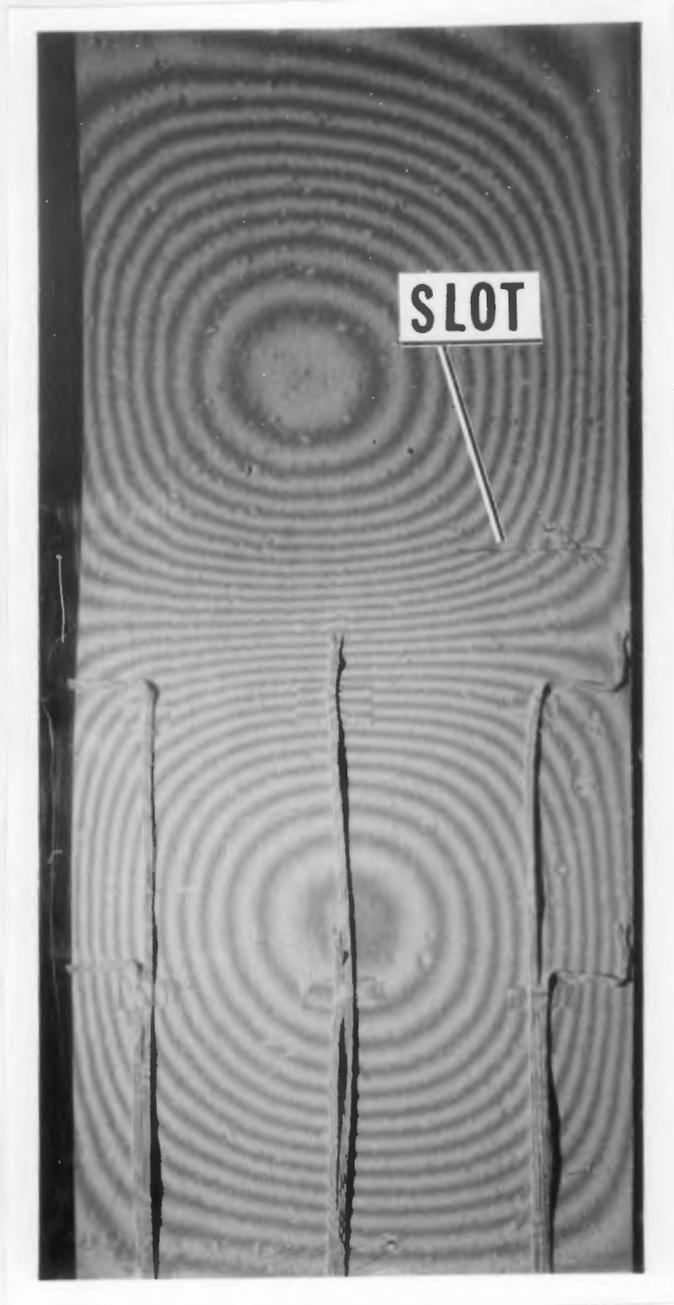
Figure 9:   Moire-fringe pattern of specimen S1, P=62 kN.
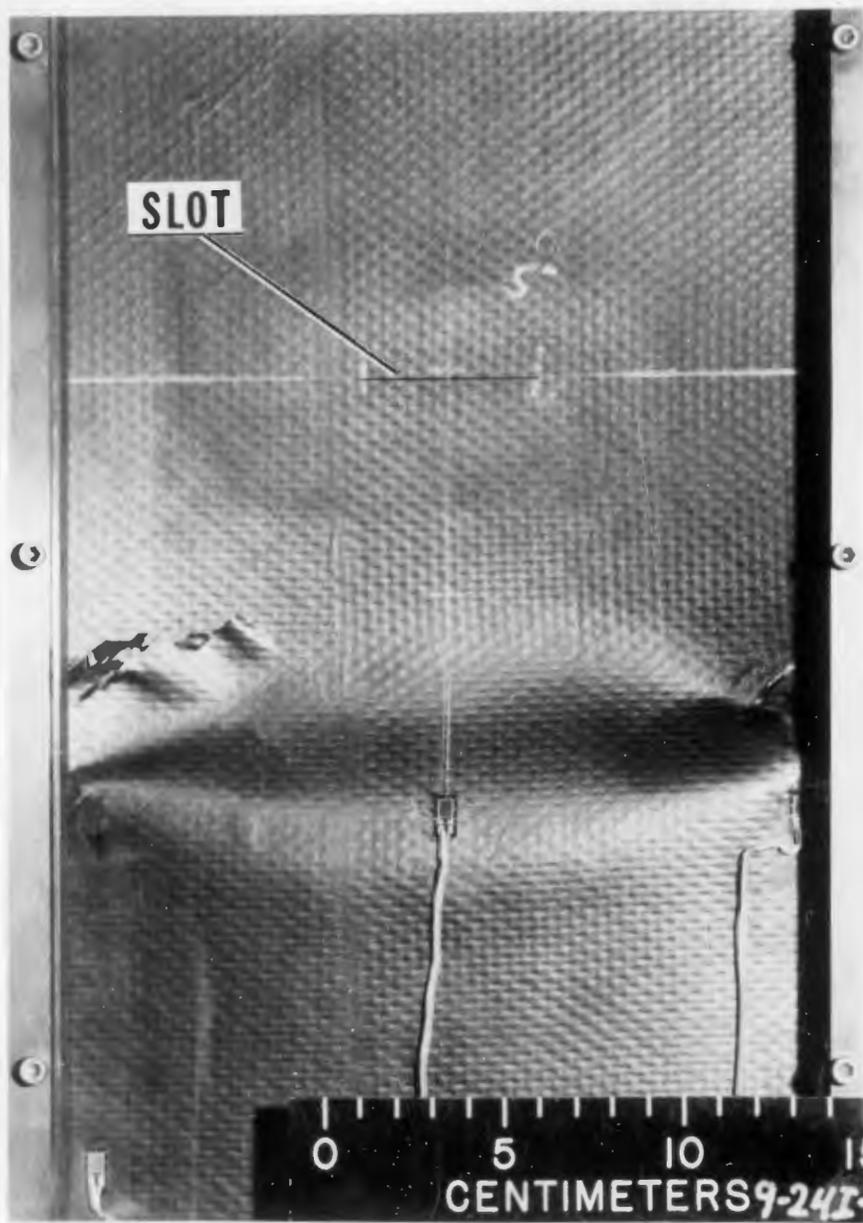
Figure 10:   Shear failure of specimen C5.
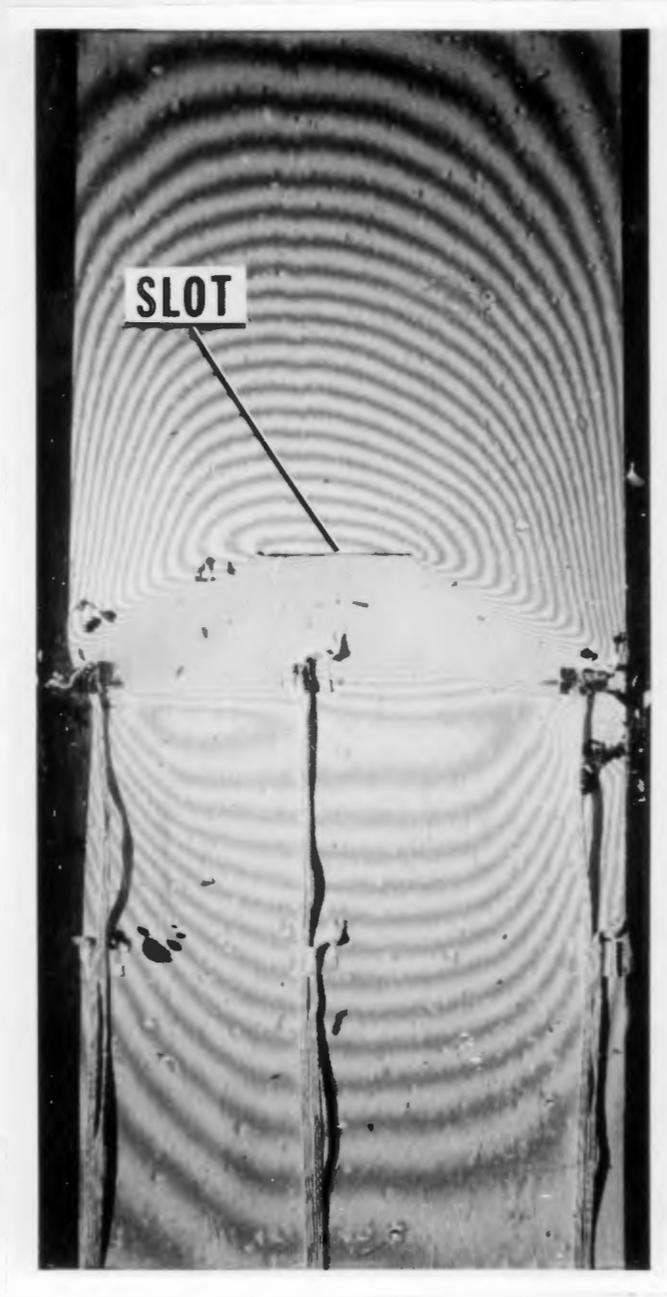
Figure 11: Damage of specimen C2 after failure.
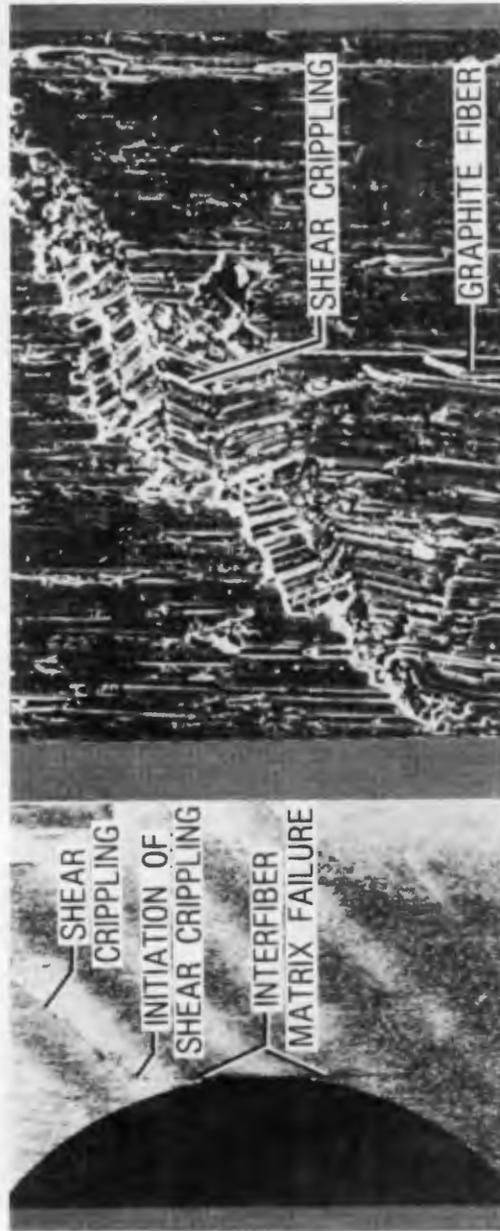
Figure 12: Shear crippling failure of specimen with a hole, from Ref. 47.
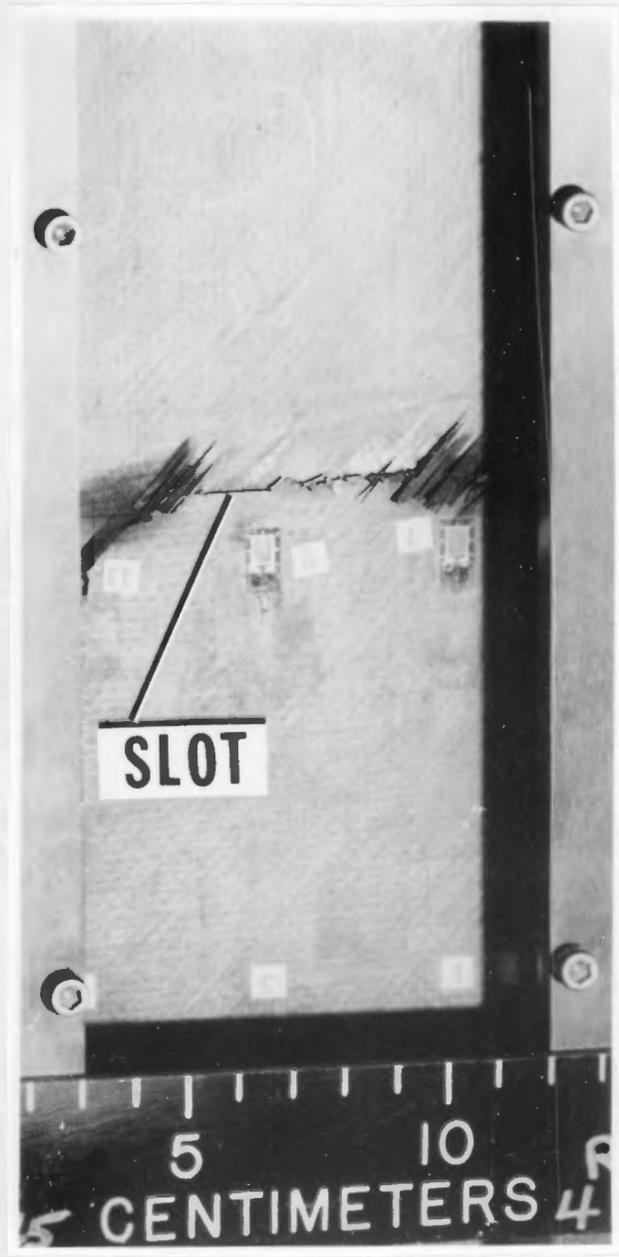
Figure 13:   Failure of specimen S2.
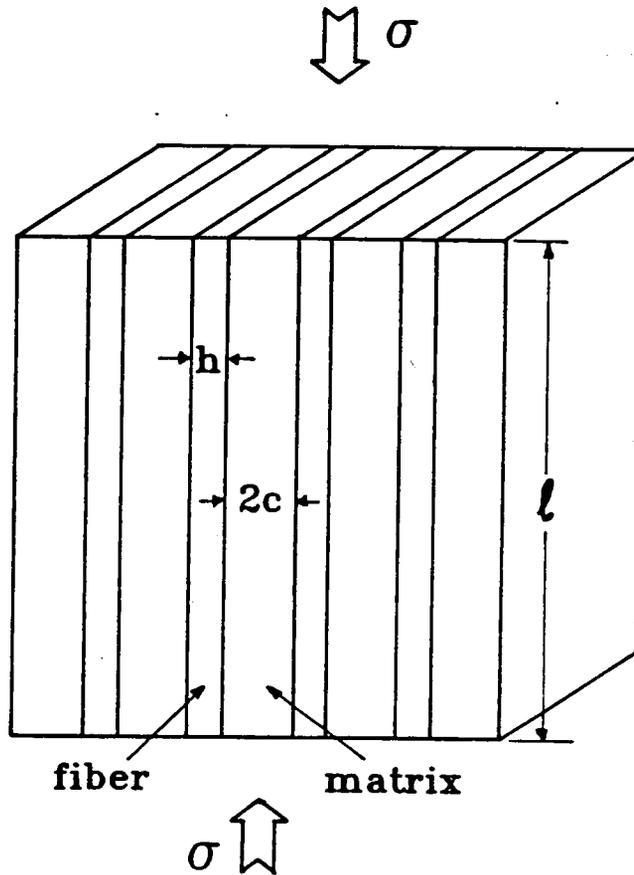
Figure 14: Composite material model considered by Rosen
[48].
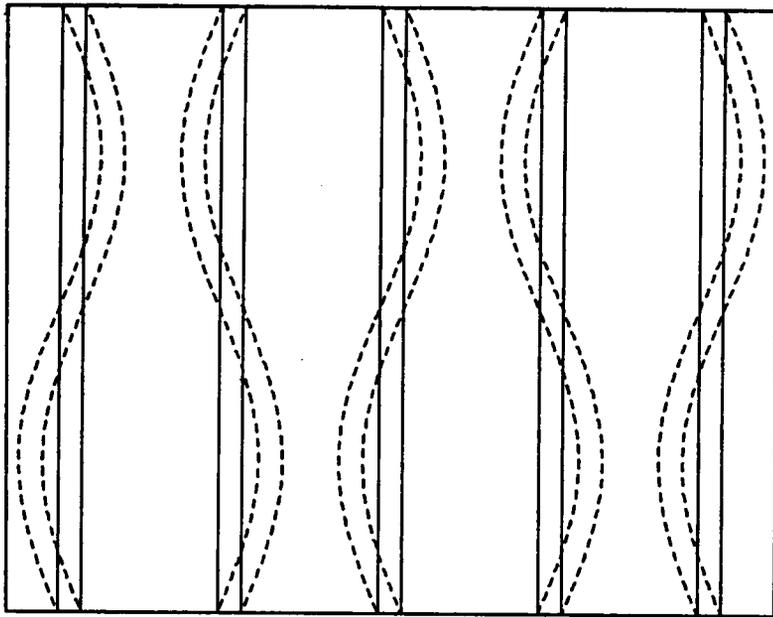
a) Extension mode.
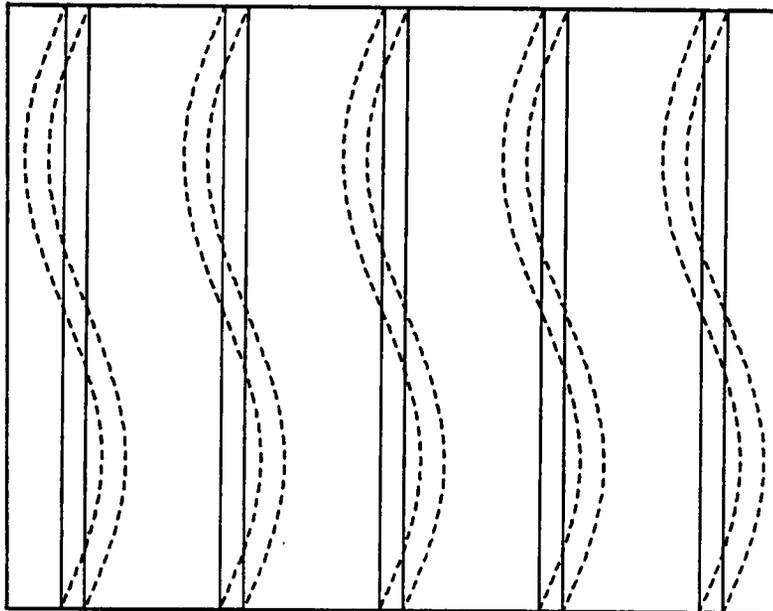
b) Shear mode.

Figure 15: Extensional and Shear modes of microbuckling
            deformations.
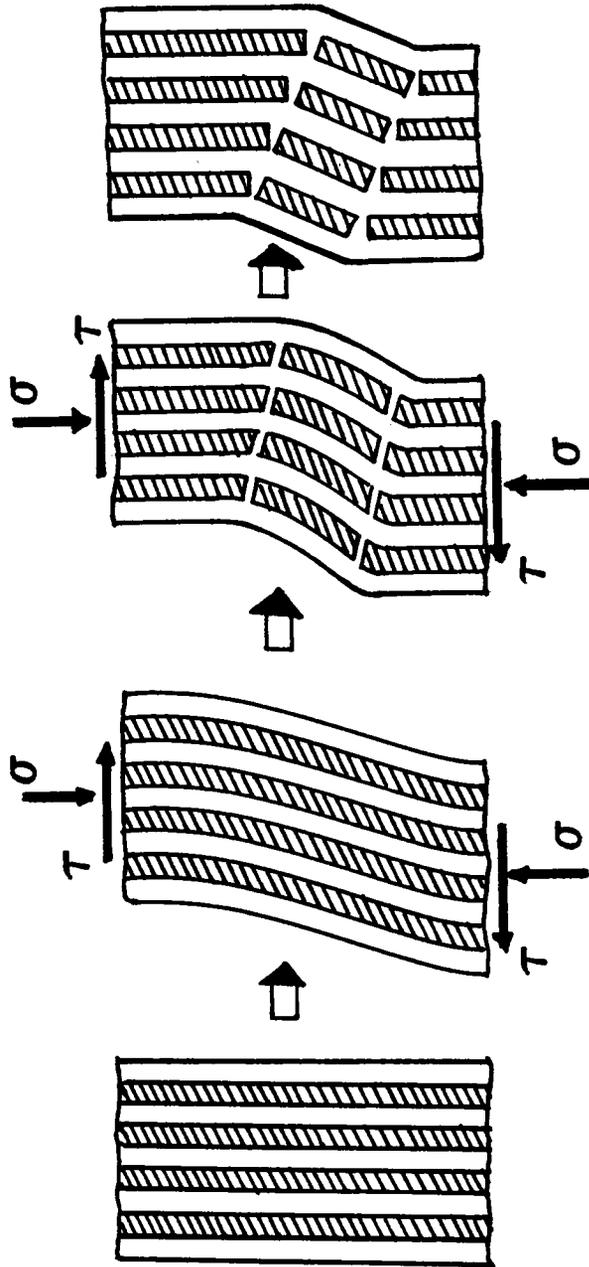
Figure 16: Kinking mode of compressive failure.
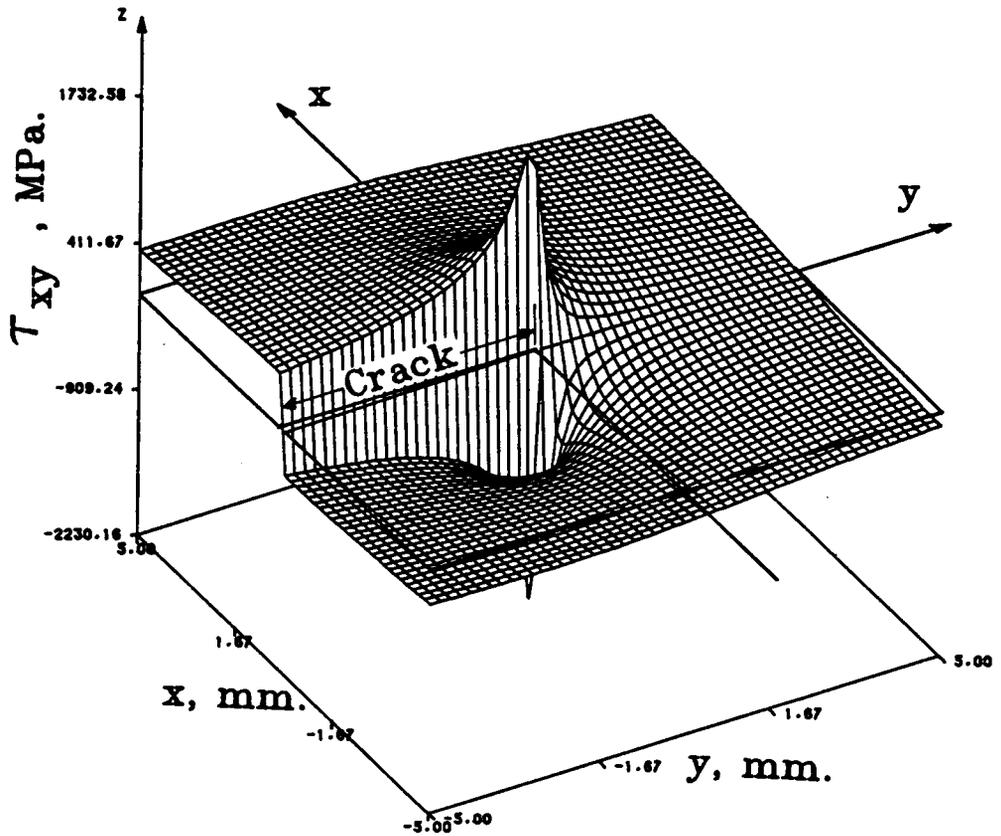
Figure 17: Magnitude of a typical crack-tip shear stress distribution in a quasi-isotropic plate, $K_I = 2500$ MPa$\sqrt{mm}$.
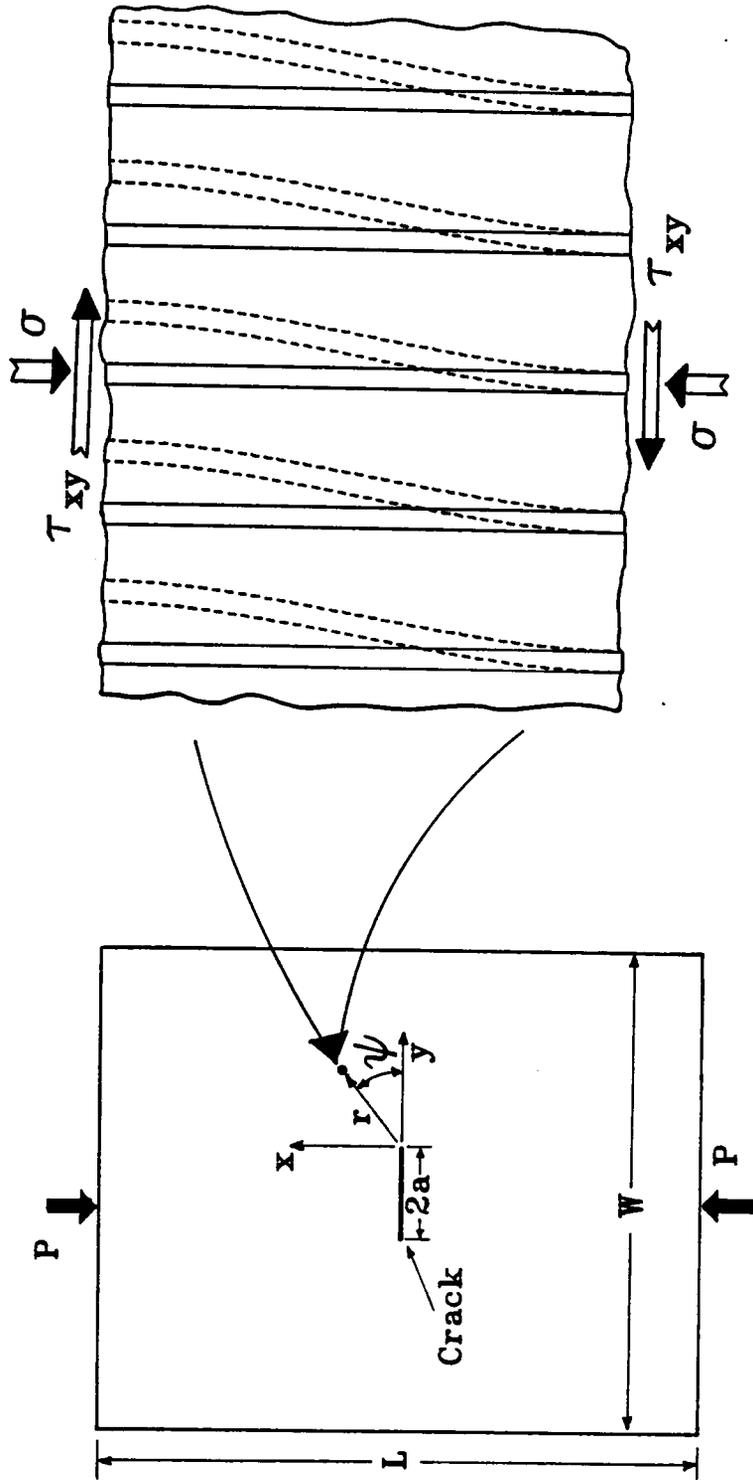
Figure 18: Deformation mode of the fibers at a point around the crack-tip.
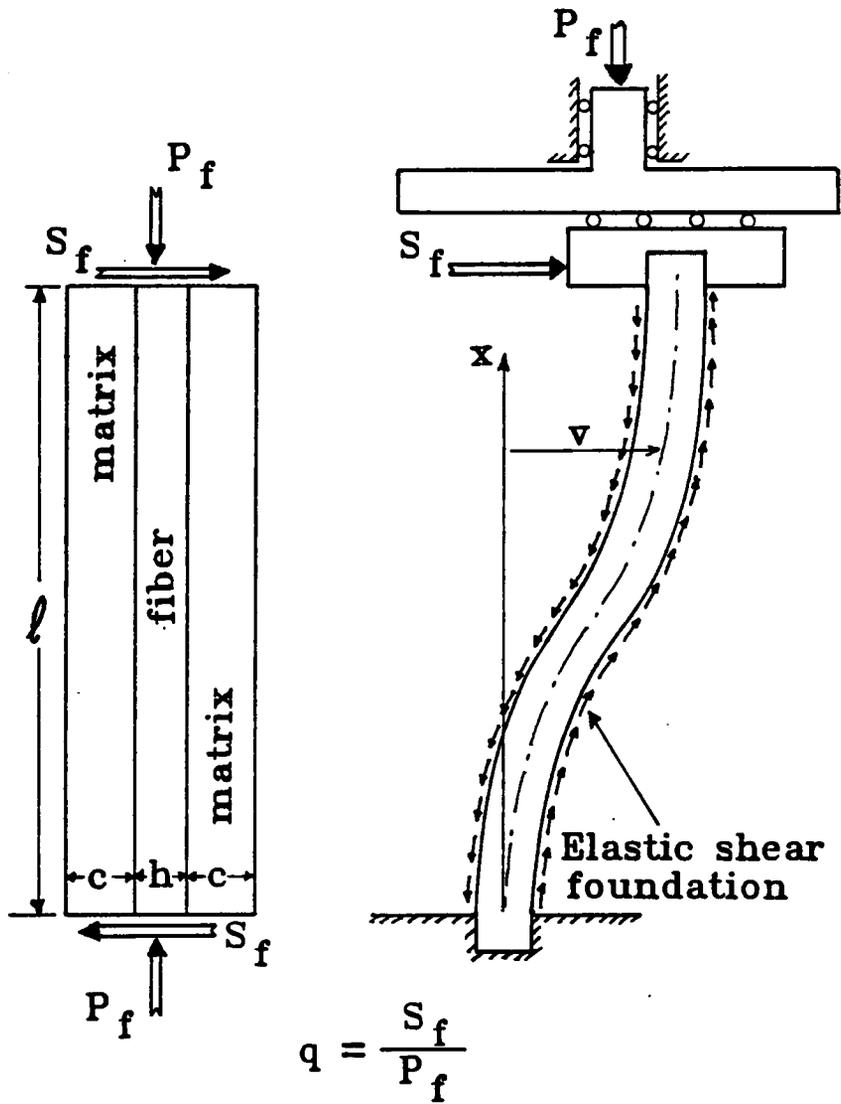
Figure 19: Beam on an elastic foundation model of a fiber under combined axial and side forces.

126
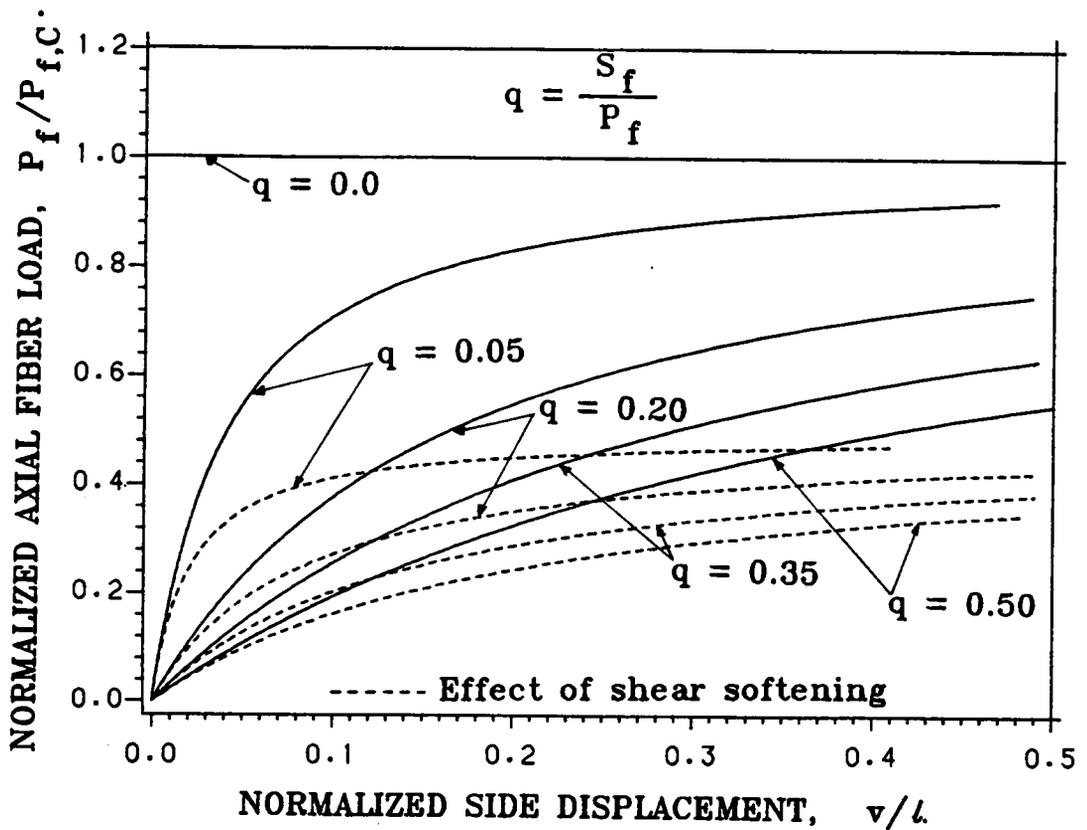
Figure 20: Fiber end (x=l) deformation for different q values.
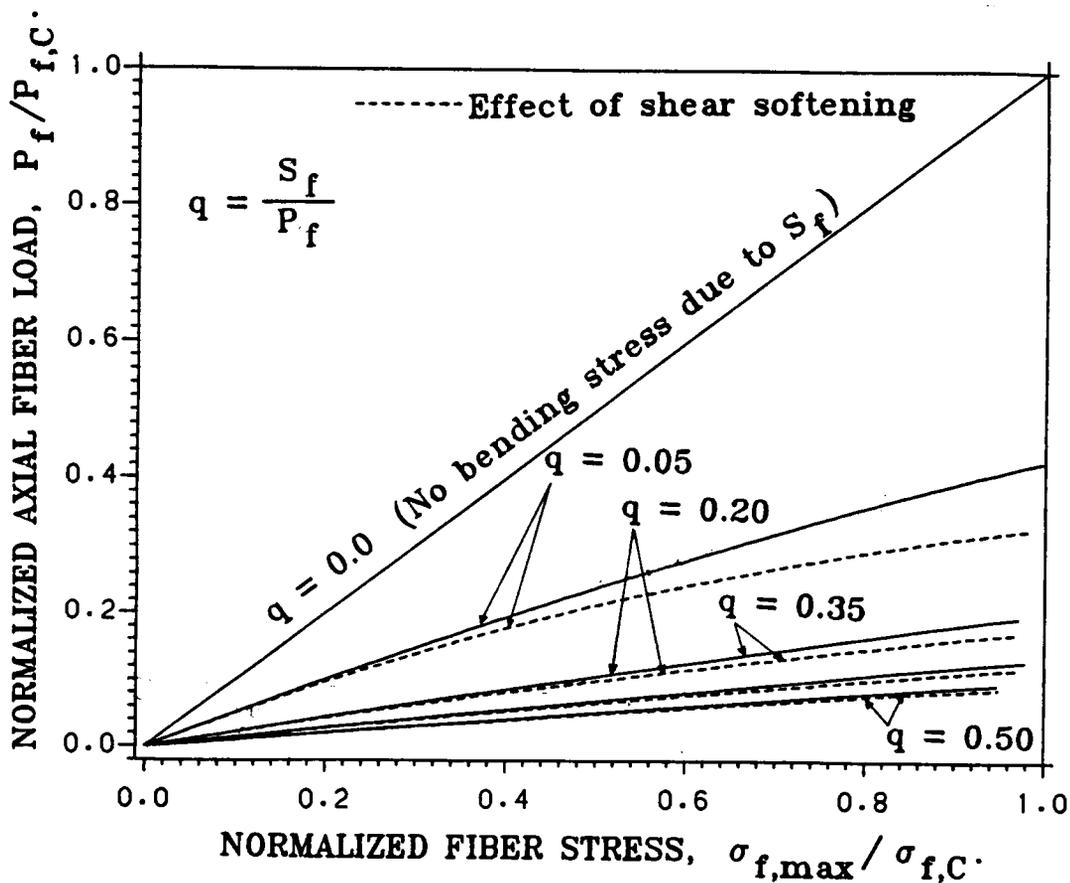
Figure 21: Maximum compressive fiber stress (combined bending and normal stress at x=0 or x=1) for different q values.
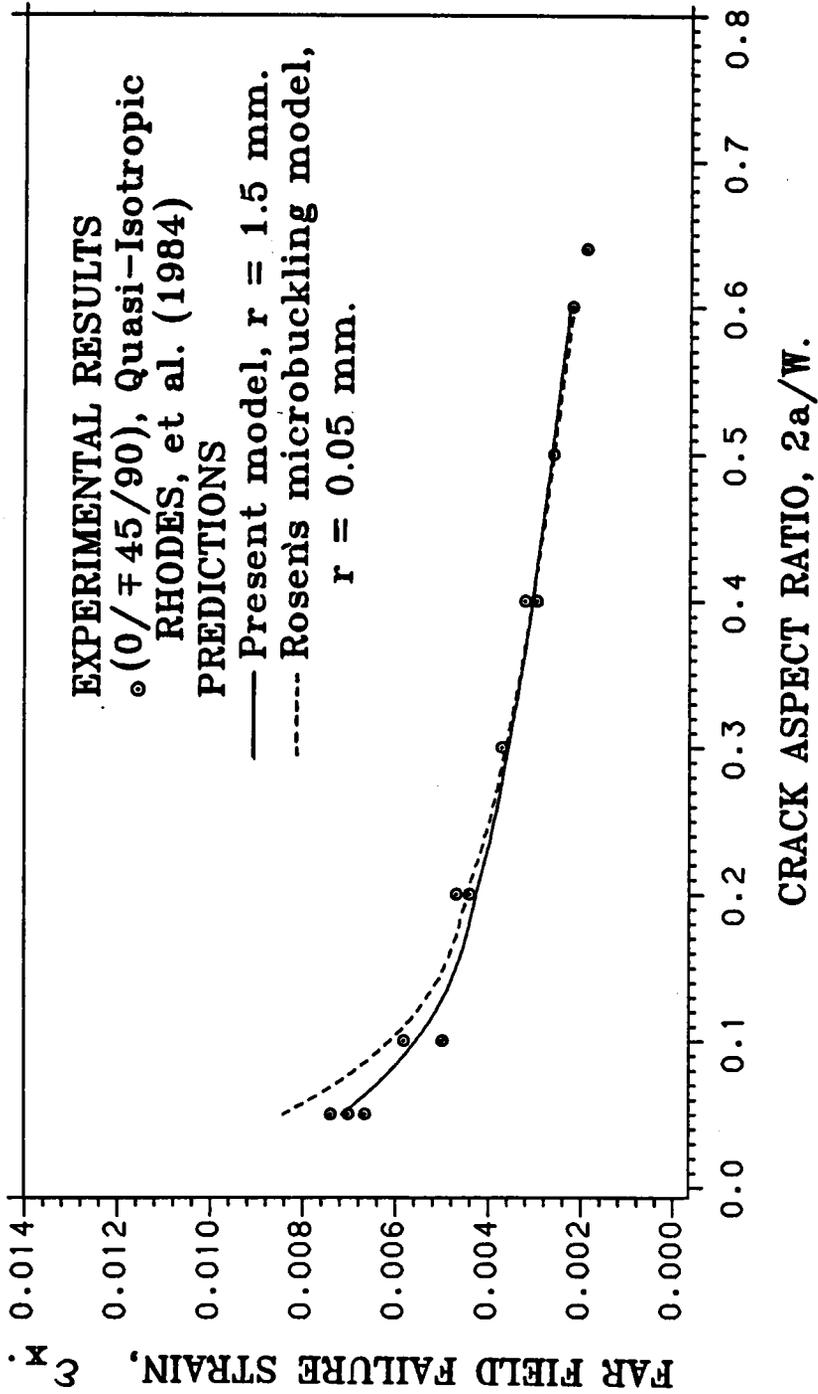
Figure 22: Failure prediction for Quasi-Isotropic plates with a crack.
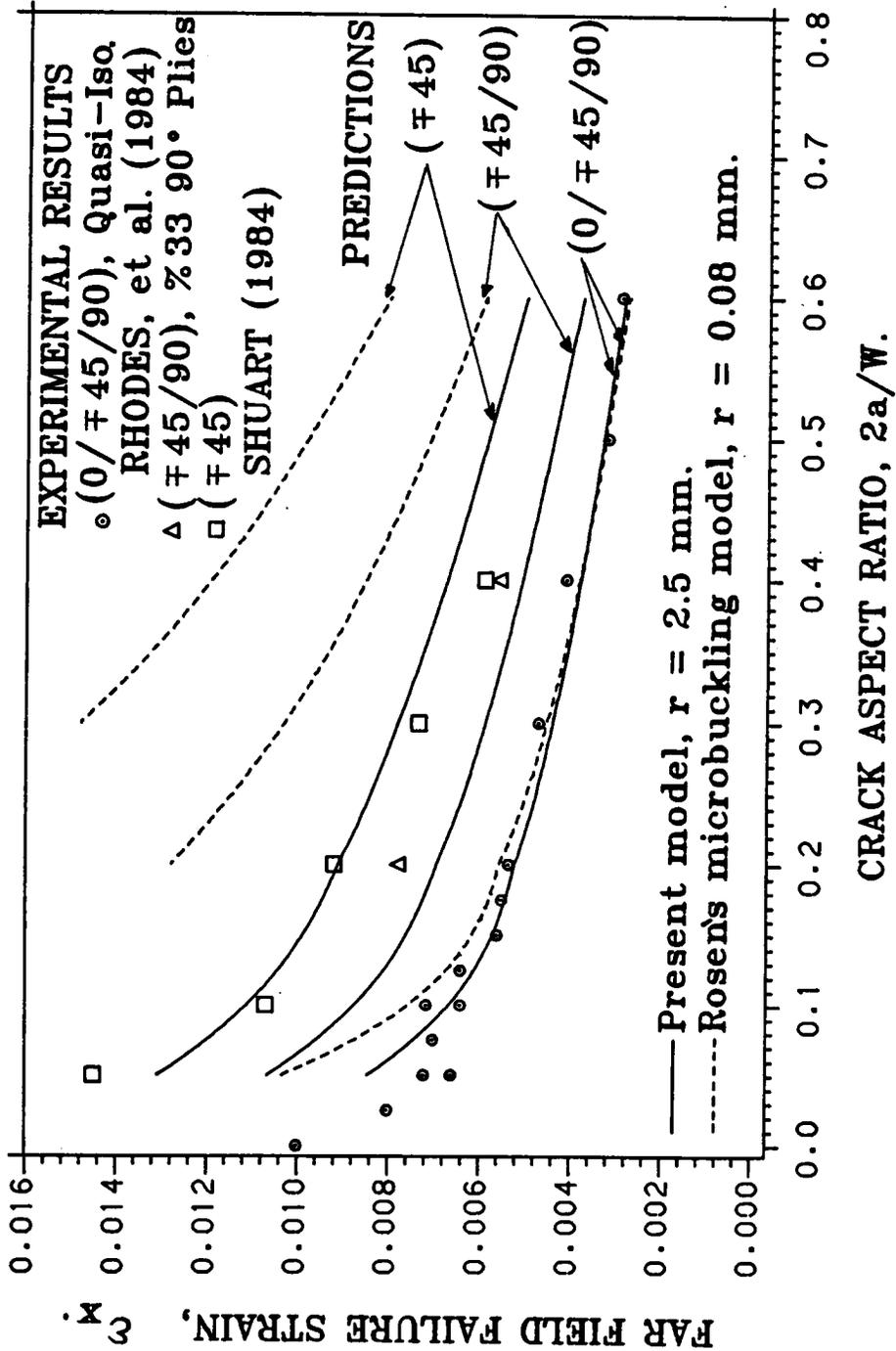
Figure 23: Failure prediction for Quasi-isotropic and ±45° dominated plates with a hole.
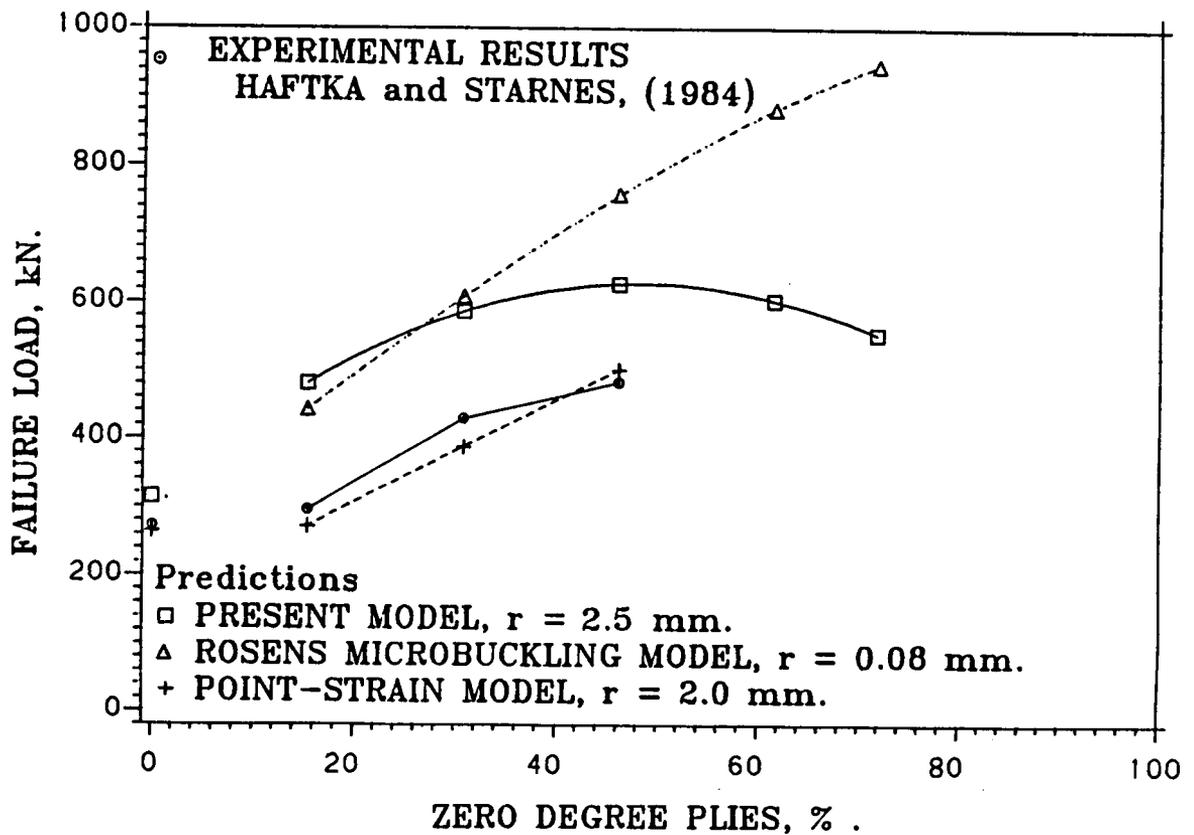
Figure 24: Comparison of failure predictions of the present
            work (Rosens model and model developed)
            with the experiment and point strain predictions of
            Haftka and Starnes. (Experimental values are for
            $[\pm 45_{18}/90_3]_S$, $[0_6/\pm 45_{15}/90_3]_S$, $[0_{12}/\pm 45_{12}/90_3]_S$, and
            $[0_{18}/\pm 45_9/90_3]_S$ layups; Point-strain criterion
            assumes 2.4% allowable strain for $\pm 45°$ plies and
            1.4% for $0°$ plies).
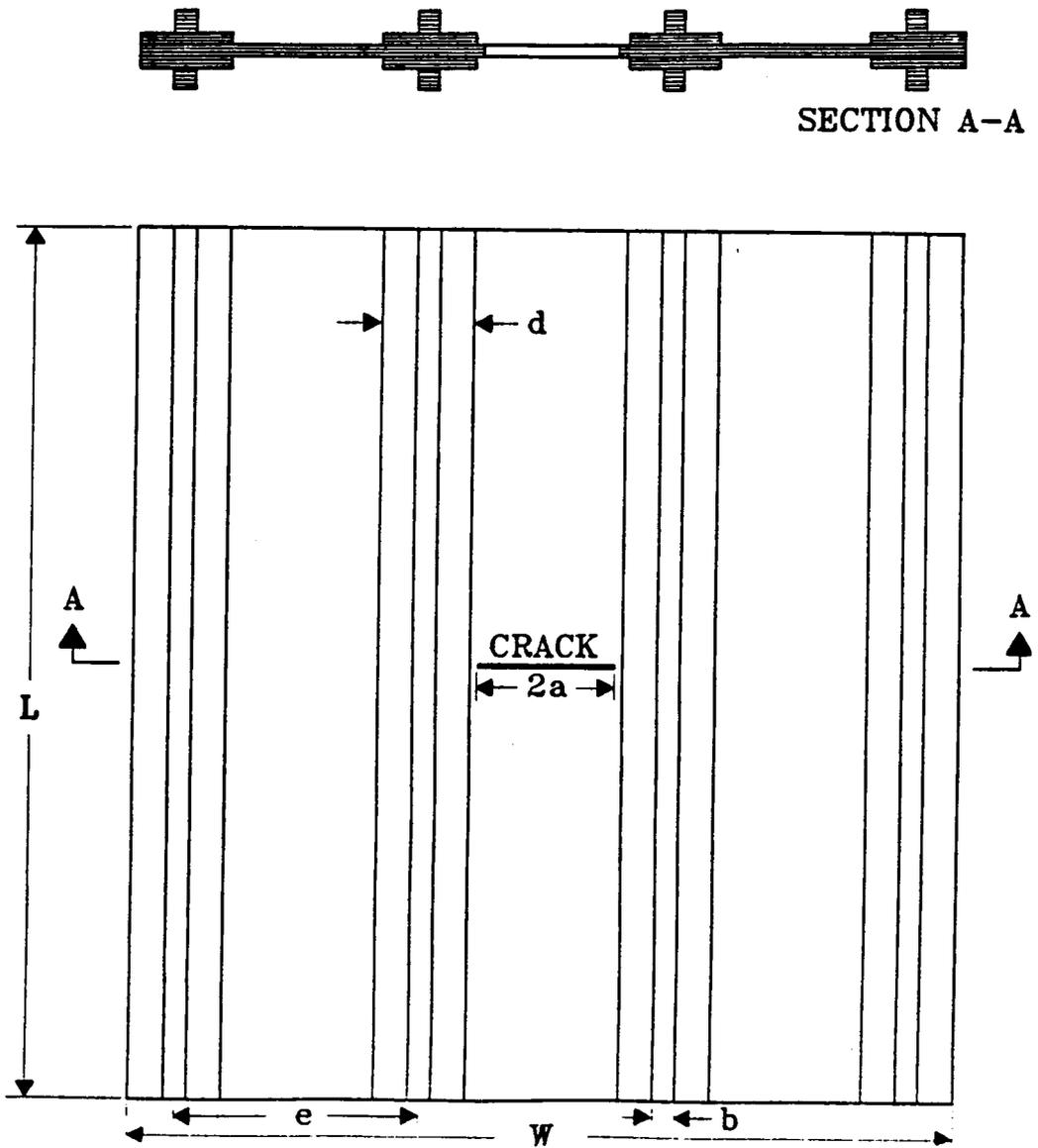
Figure 25:   Stiffened plate geometry.
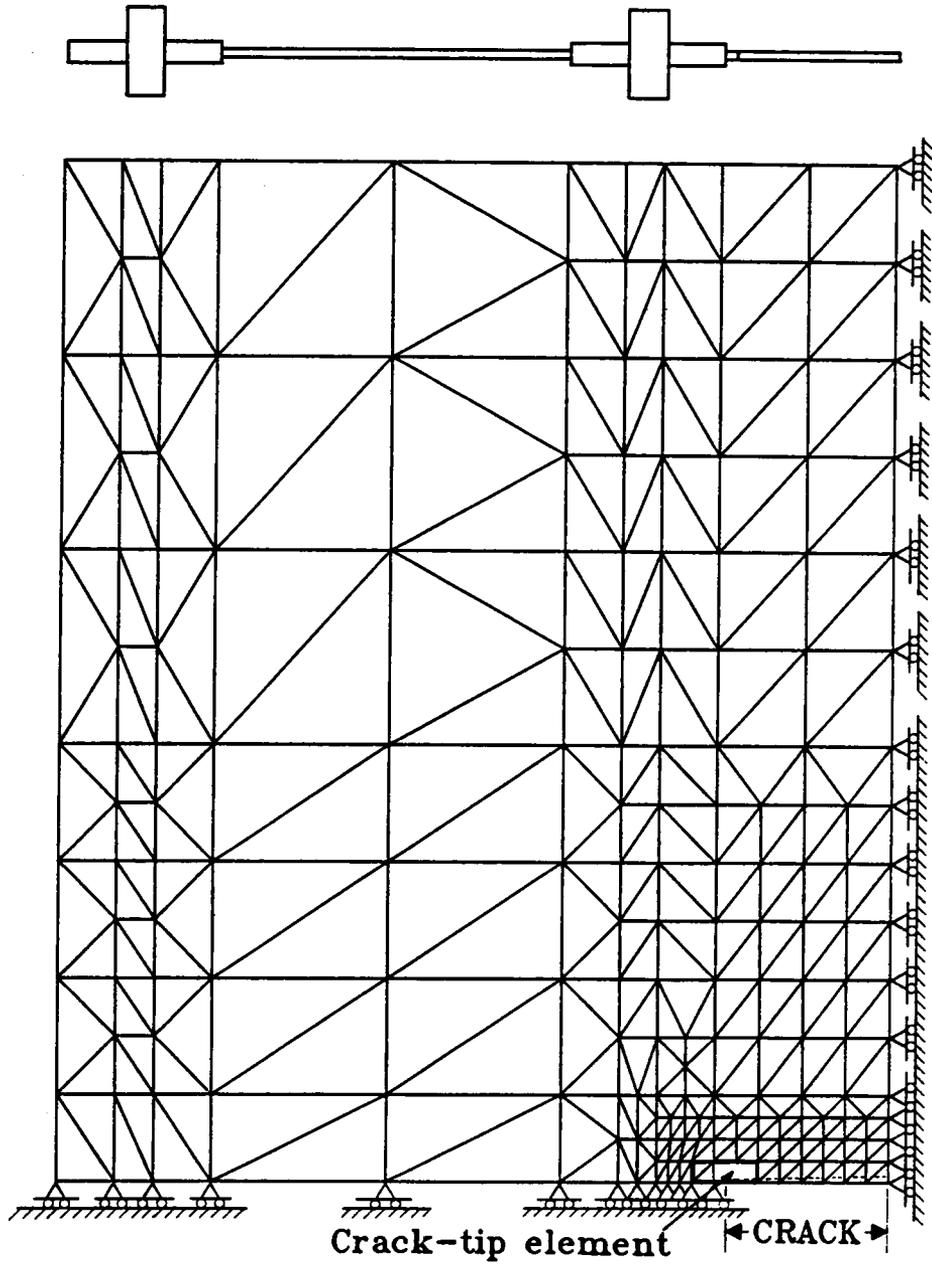
Figure 26:   A typical quarter-plate finite element mesh for a stiffened plate.
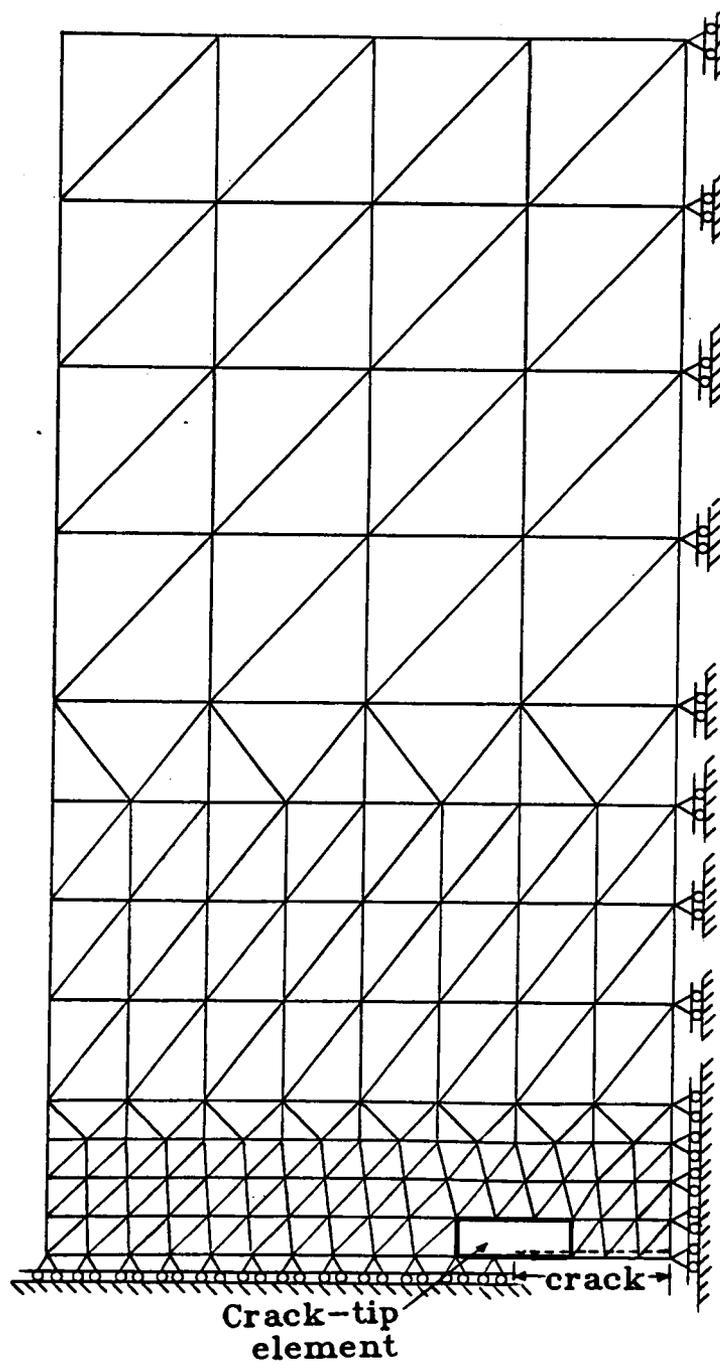
Figure 27: A typical quarter-plate finite element mesh for
an unstiffened plate.
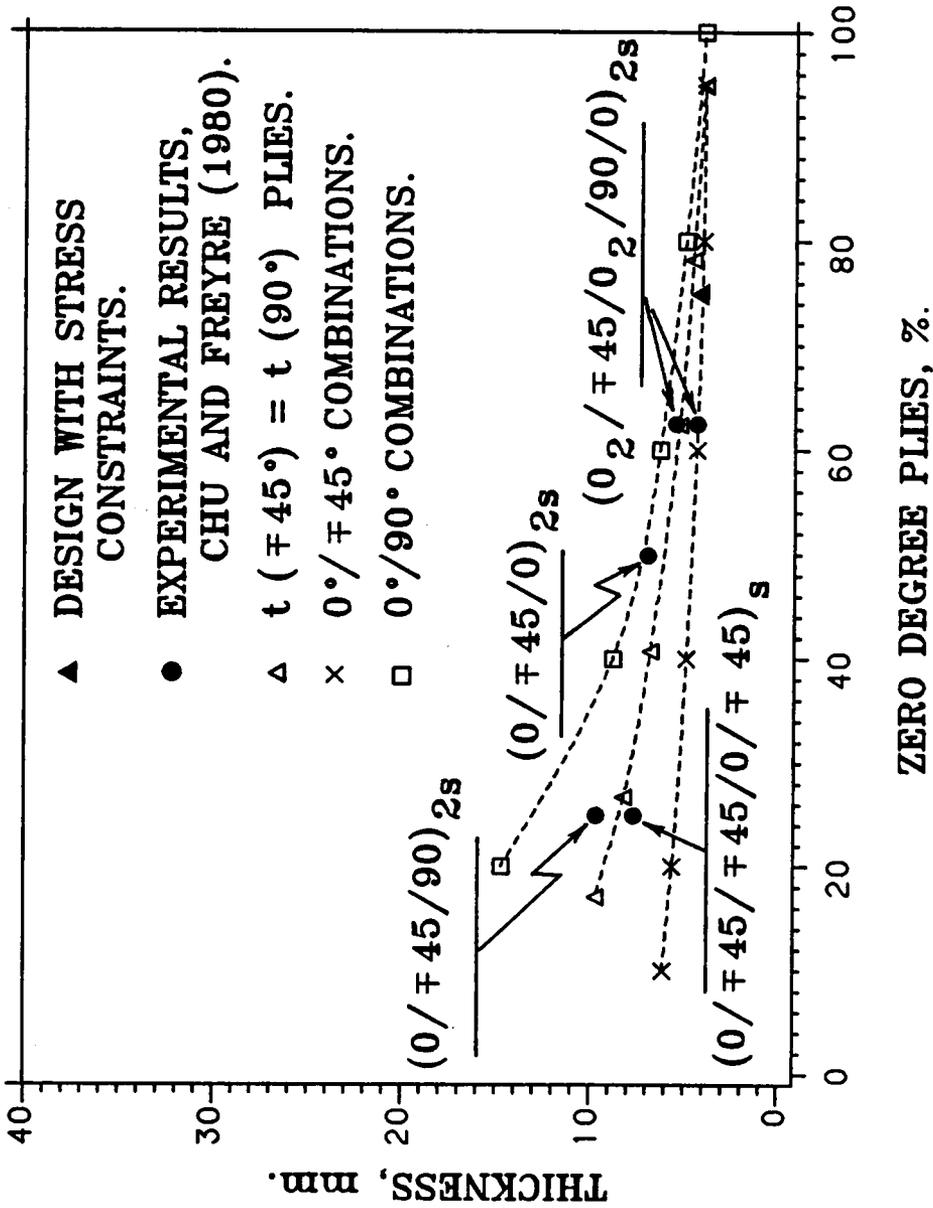
Figure 28: Unstiffened plate designs under tension, (P=122 kN, W=76.2 mm, 2a/W=0.2, L/W=3.0).
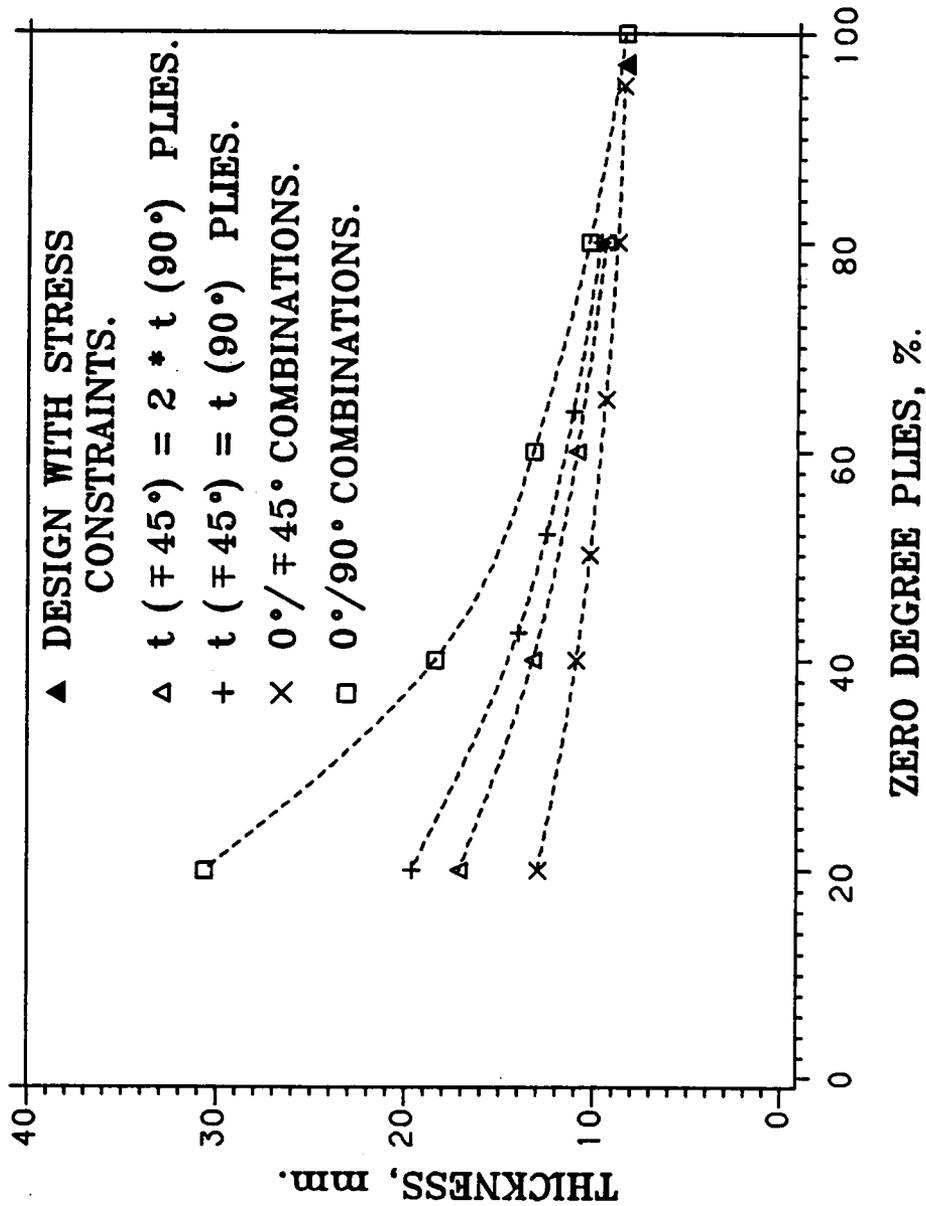
Figure 29: Unstiffened plate designs under tension, (P=122 kN, W=76.2 mm, 2a/W=0.6, L/W=3.0).
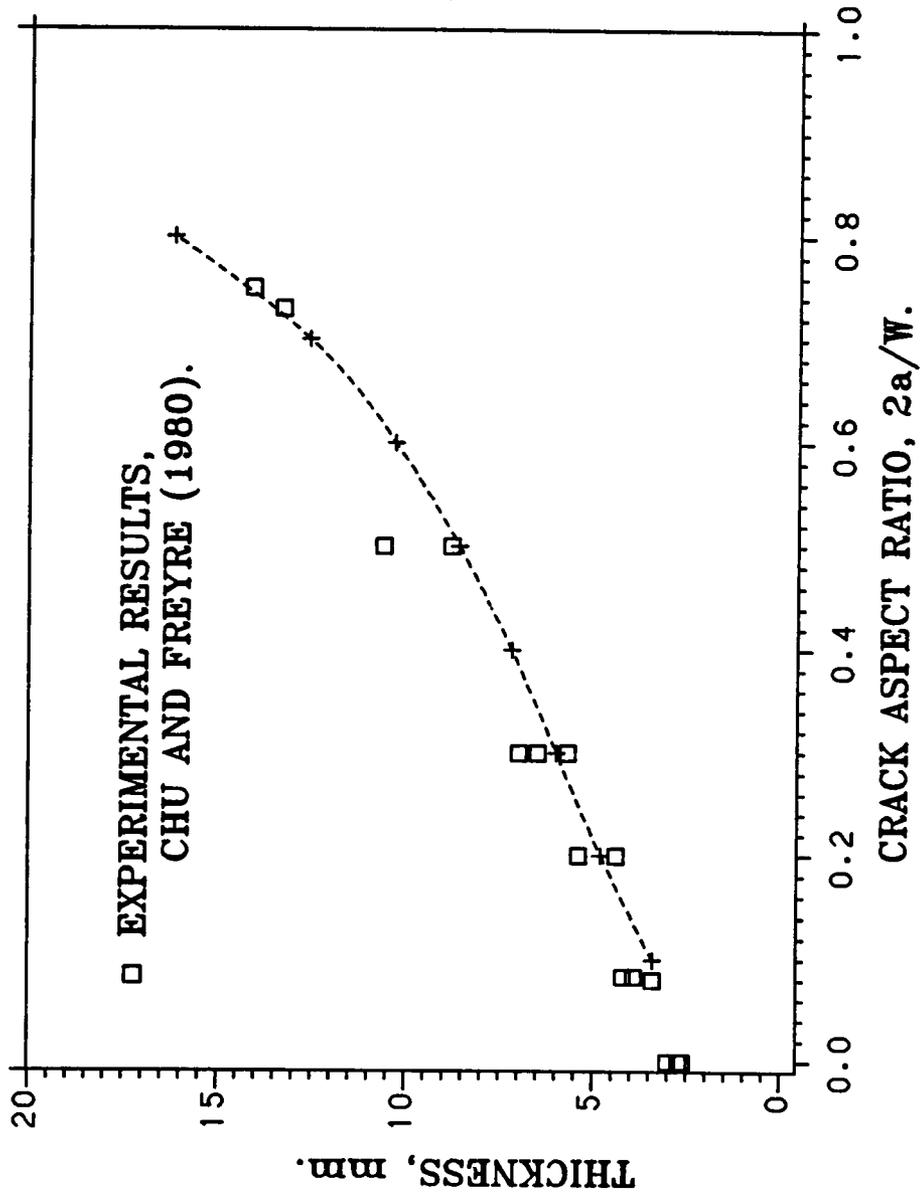
Figure 30: Effect of crack length on unstiffened plate design for ply combinations similar to $[0_2/\pm45/0_2/90/0]_S$, (P=122 kN).

Figure 31: Plates with side stiffening strips under tension, (P=122 kN, 20% shear force, W=76.2 mm, L/W=3.0, crack extending from one strip to the other).
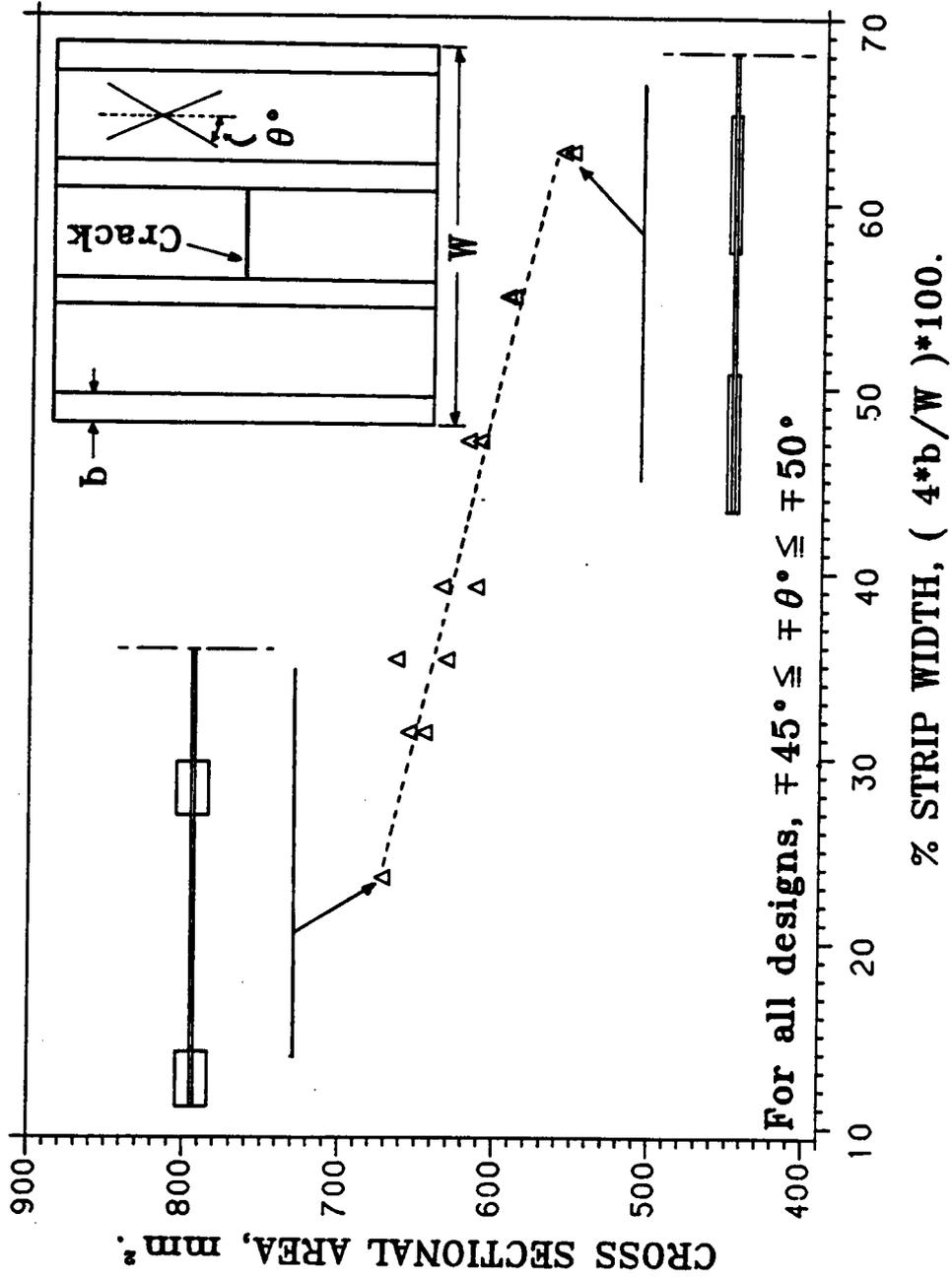
Figure 32: Plates with four stiffening strips under tension, panel section with only optimum ±θ° ply orientations, (P=600 kN, W=255 mm, L/W=1.6).
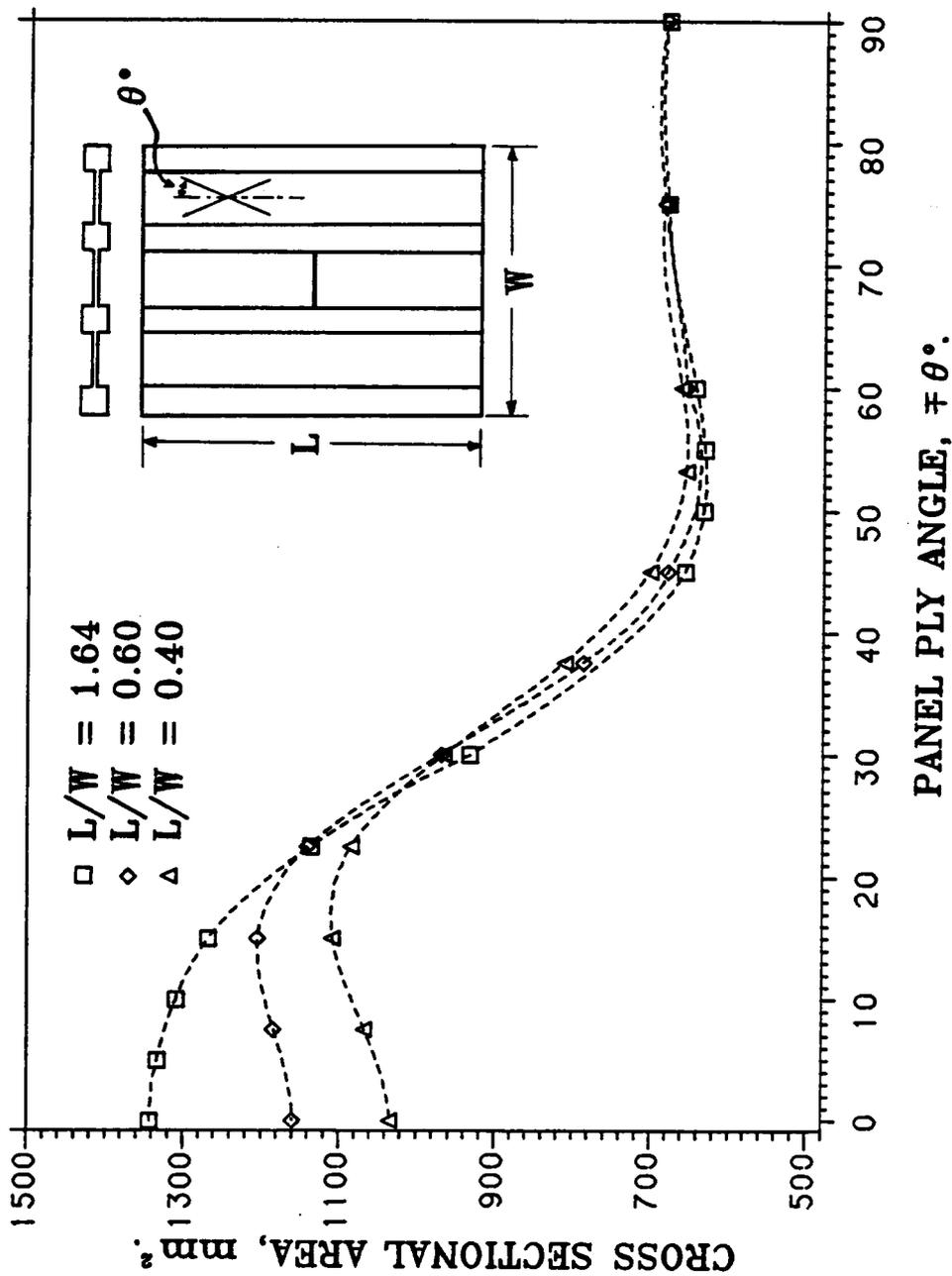
Figure 33: Effects of panel angle and length on weight,
(only ±θ° plies in the panel, t_p=1.12 mm, P=600 kN,
b=22,5 mm, e=77.5 mm, W=255 mm).
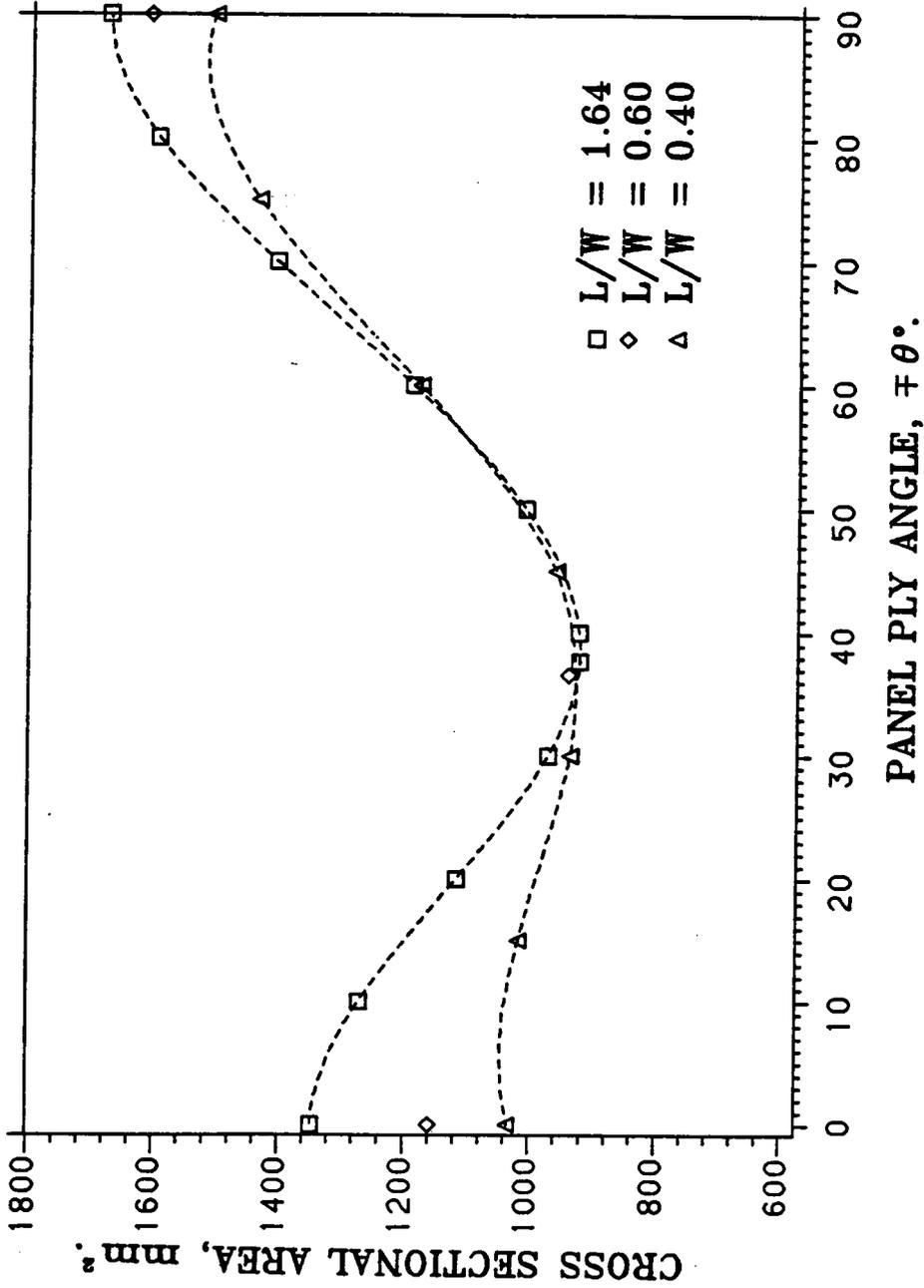
Figure 34: Effects of panel angle and length on weight,
(0°/±θ° panel, 0.28 mm 0° plies, 0.84 mm ±0°
plies, P=600 kN, b=22.5 mm, e=77.5 mm, W=255 mm).
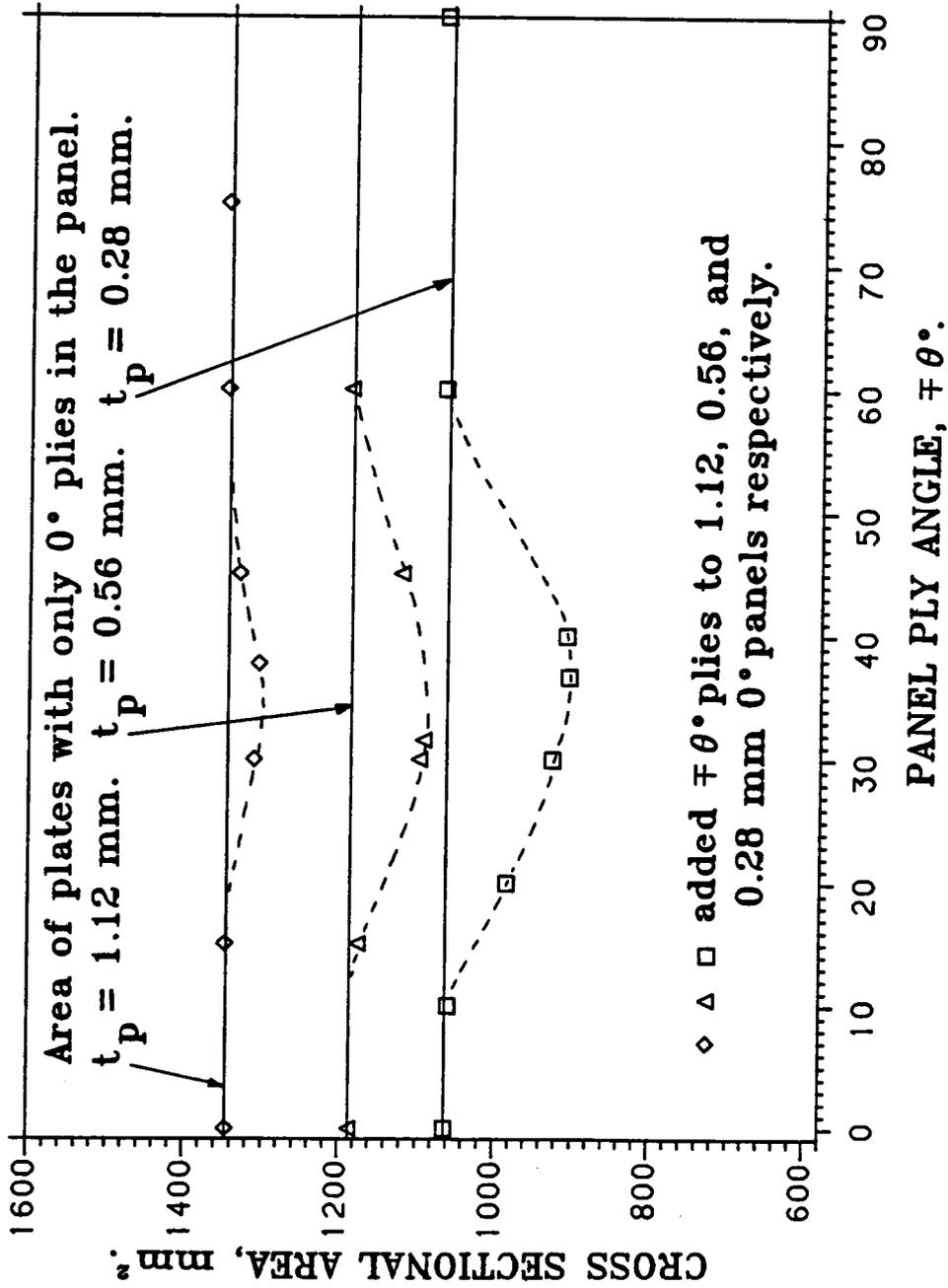
Figure 35: Effect of added angle plies to 0° panel section of a stiffened plate under tension, (P=600 kN, b=22.5 mm, e=77.5 mm, W=255 mm).
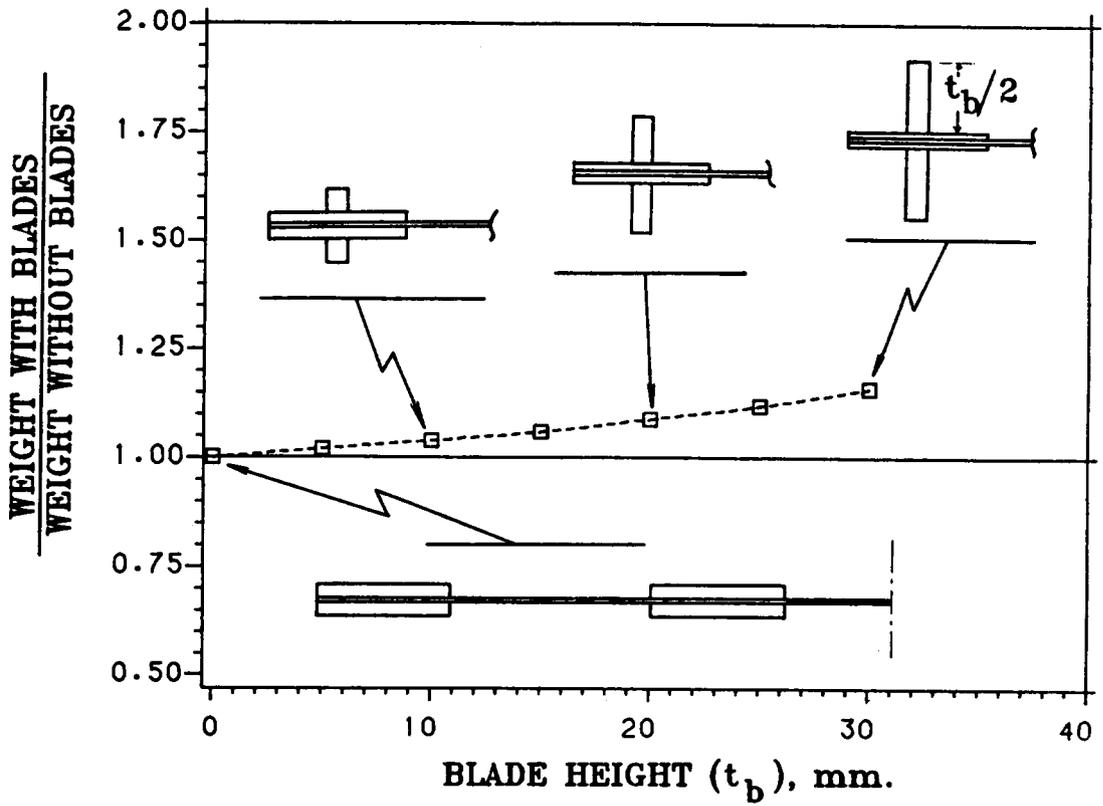
Figure 36: Weight penalty due to blade stiffeners, (P=600 kN, b=5 mm, d=30 mm, e=75 mm).
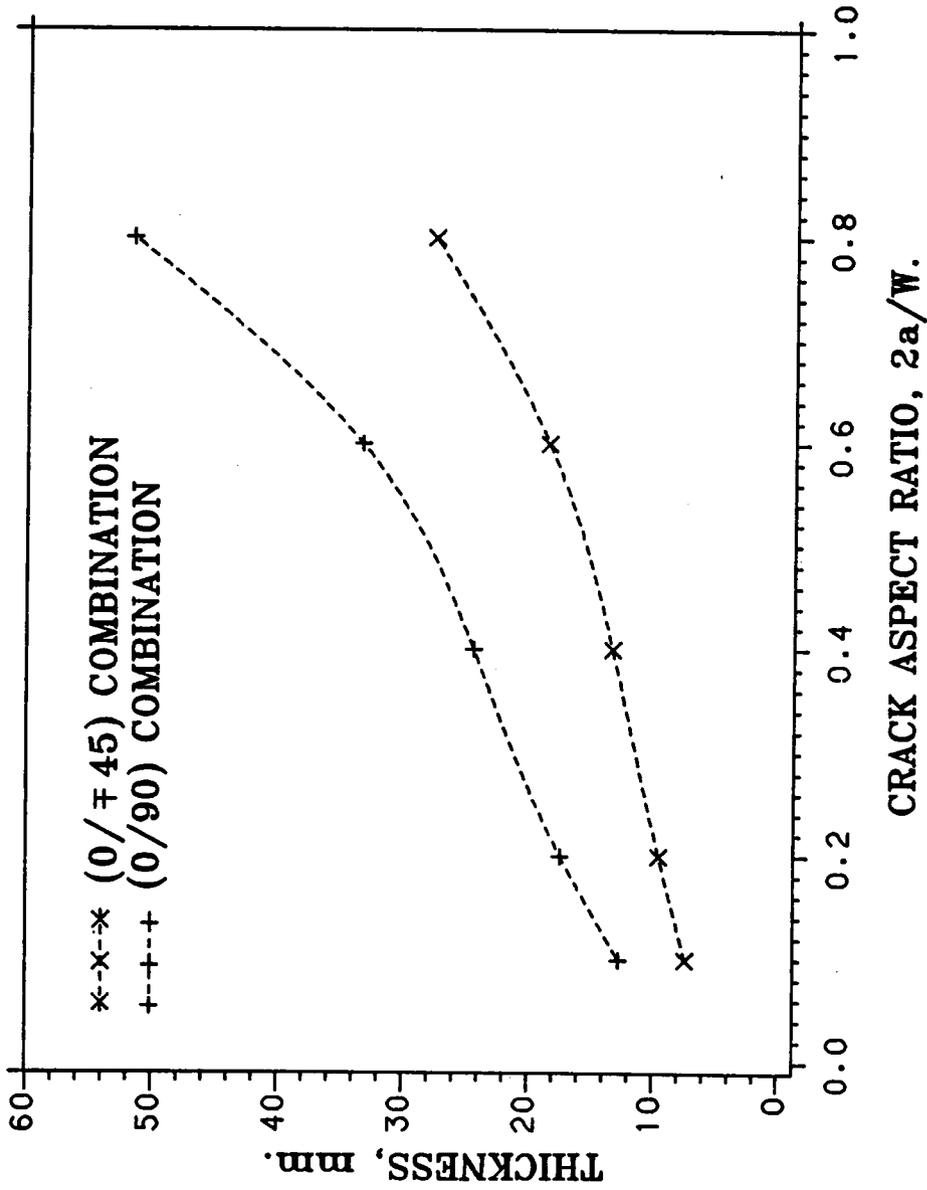
Figure 37: Unstiffened plate designs under compression, (P=500kN, W=127 mm, L/W=3.0).
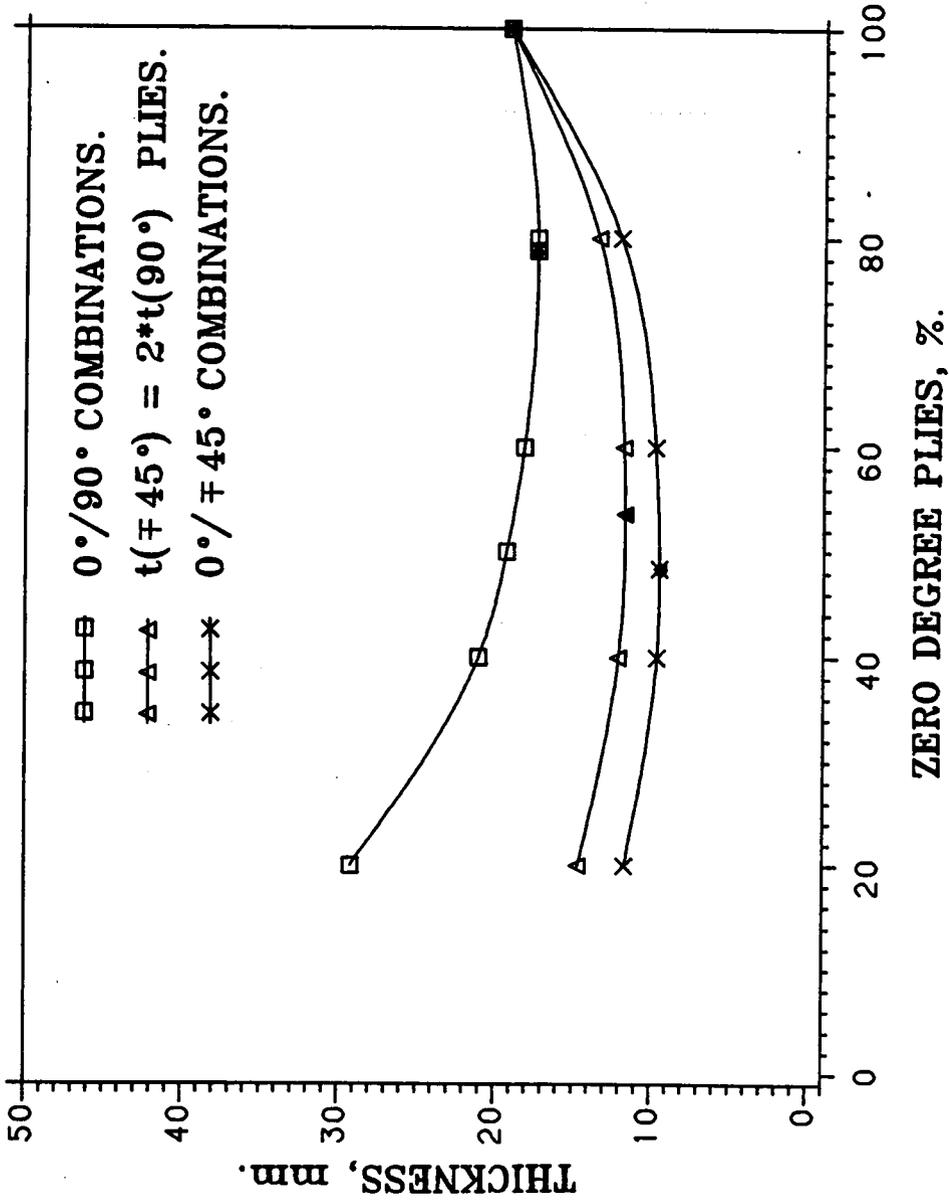
Figure 38: Unstiffened plate designs under compression,
(P=500 kN, W=127 mm, 2a/W=0.2, L/W=3.0).
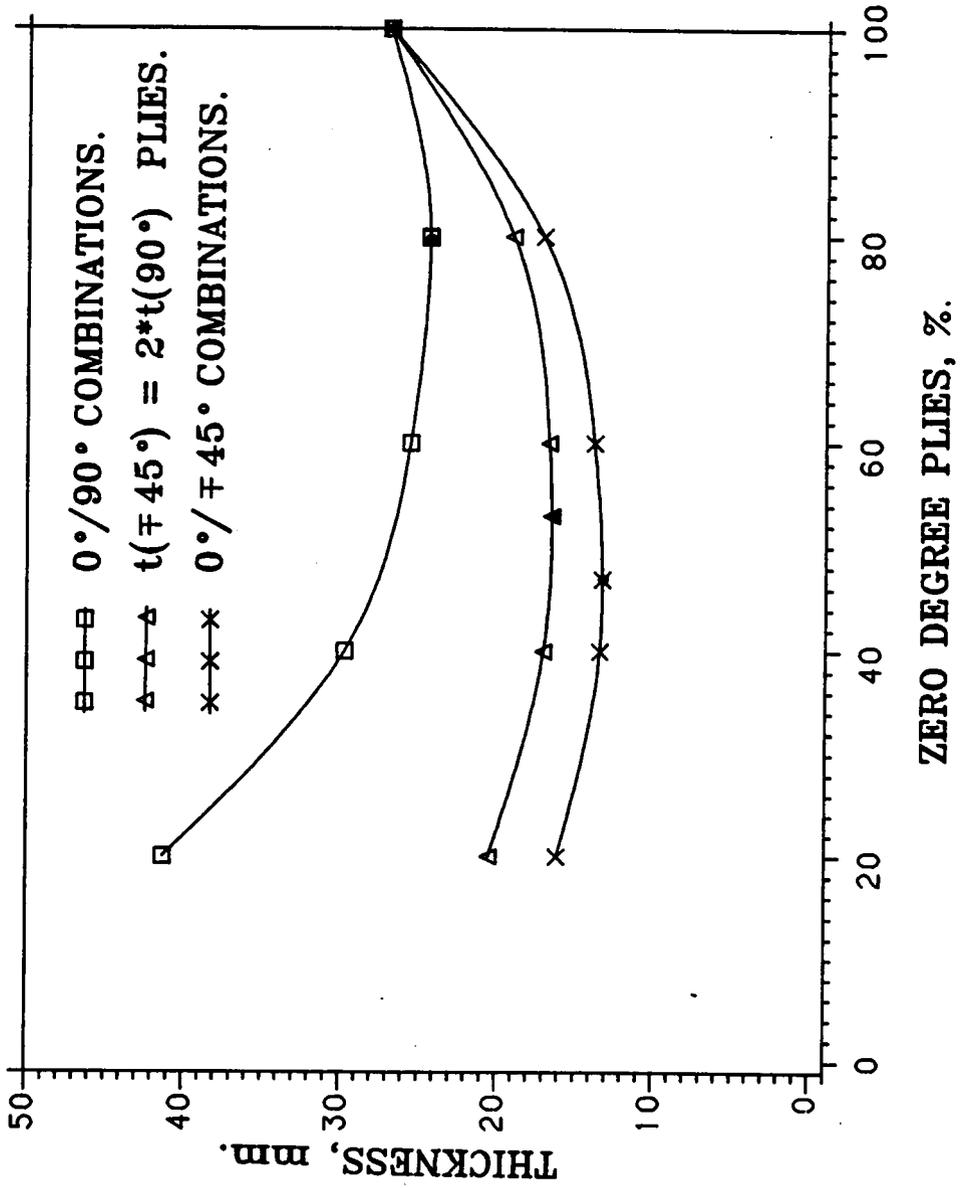
Figure 39: Unstiffened plate designs under compression,
(P=500 kN, W=127 mm, 2a/W=0.4, L/W=3.0).
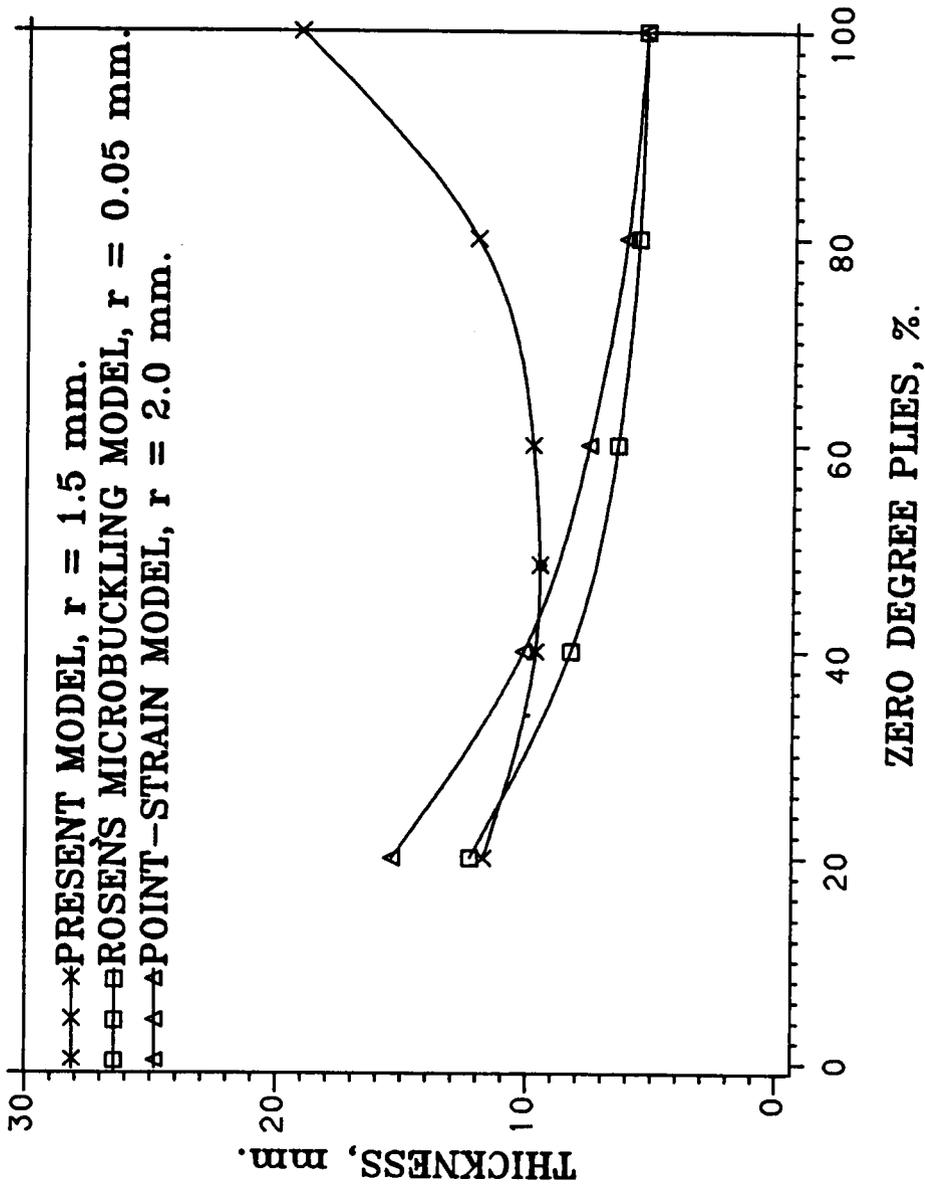
Figure 40: Comparison of different models for unstiffened (0°/±45°) plates under compression (P=500 kN, 2a/W = 0.2).
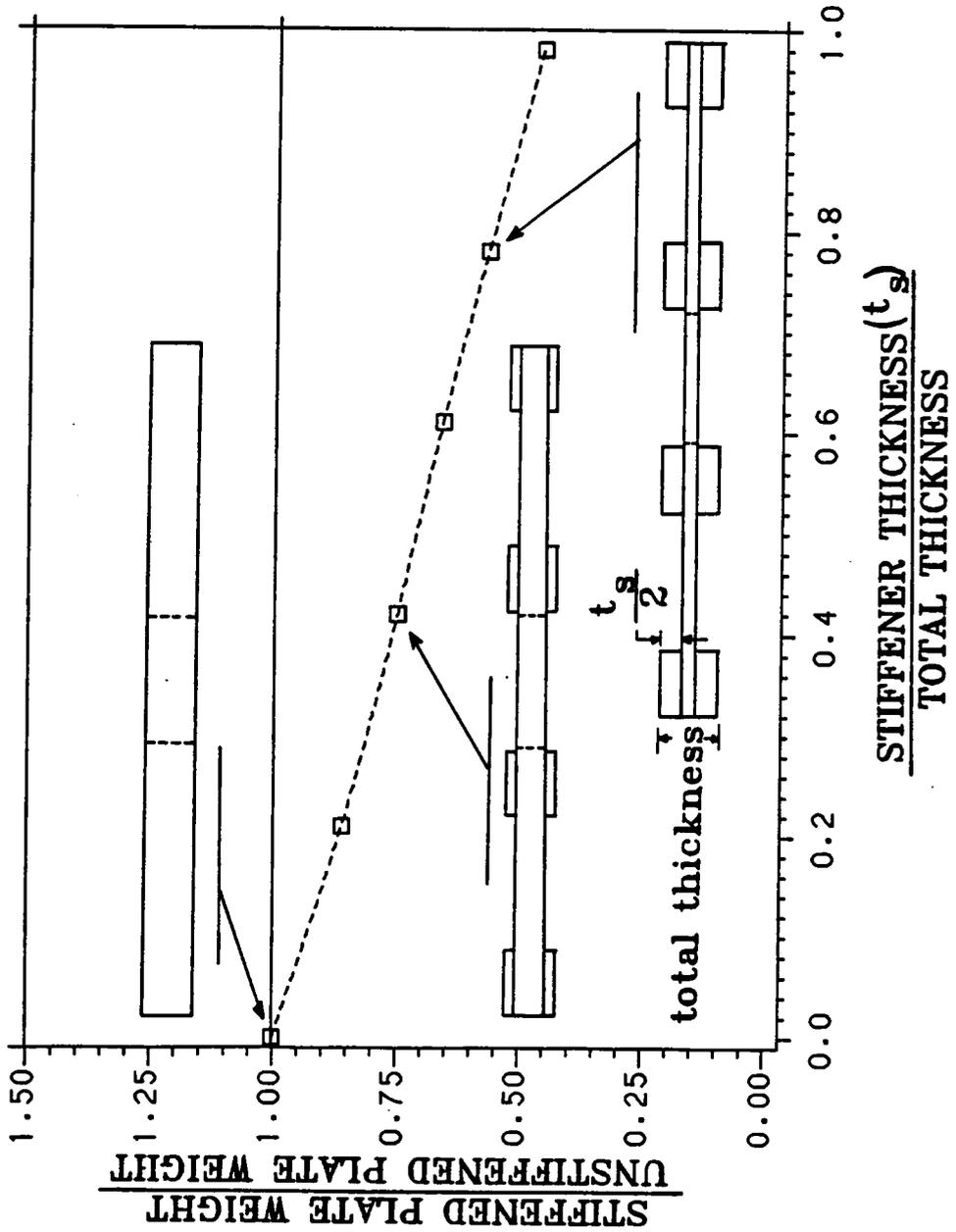
Figure 41: Weight saving due to stiffeners for compression plates, (P=500 kN, b=12.7 mm, e=25.4 mm).
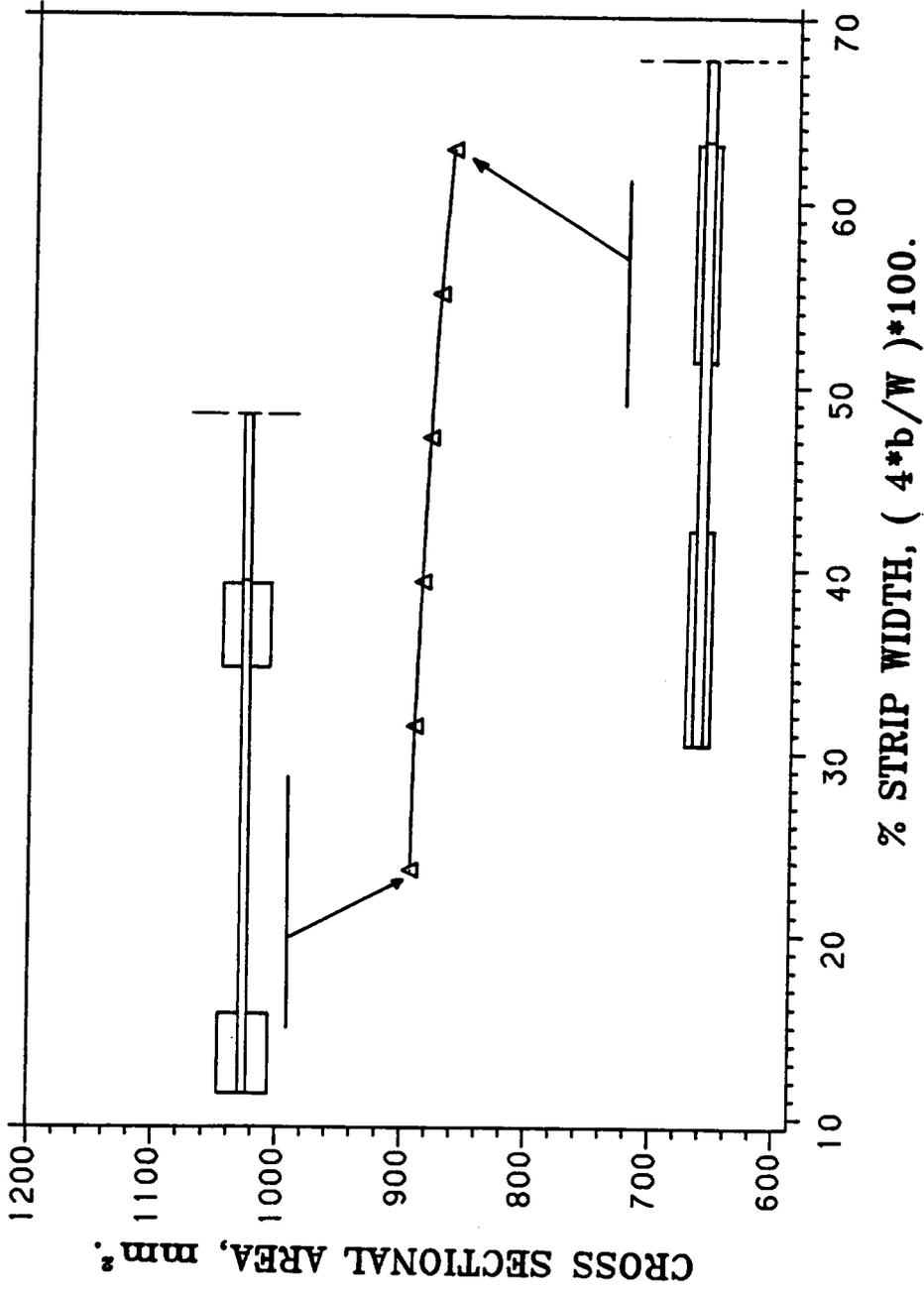
Figure 42: Plates with four stiffening strips under compression, (P=500 kN, W=255 mm, L/W=1.6).
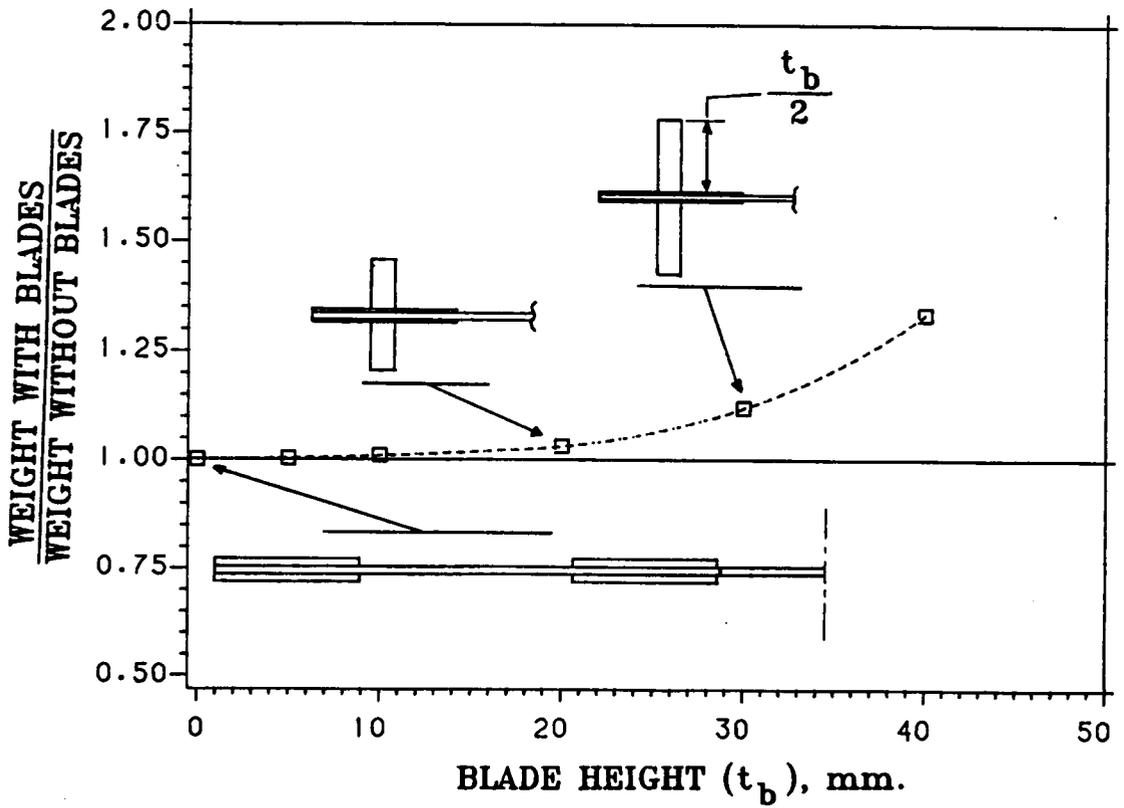
Figure 43: Weight penalty due to blade stiffeners under cmpression, (P=500 kN, b=5 mm, d=30 mm, e=75 mm).

Automated Design of Composite Plates
for
Improved Damage Tolerance

by

Zafer Gürdal
Committee Chairman: Raphael T. Haftka
Aerospace and Ocean Engineering

(ABSTRACT)

An automated procedure for designing minimum-weight composite plates subject to a local damage constraint under tensile and compressive loadings has been developed. A strain based criterion was used to obtain fracture toughness of cracked plates under tension. Results of an experimental investigation of the effects of simulated through-the-thickness cracks on the buckling, postbuckling, and failure characteristics of composite flat plates are presented. A model for kinking failure of fibers at the crack tip was developed for compression loadings. A finite element program based on linear elastic fracture mechanics for calculating stress intensity factor (SIF) was incorporated in the design cycle. A general purpose mathematical optimization algorithm was used for the weight minimization. Analytical sensitivity derivatives of the SIF, obtained by employing the adjoint variable technique, were used to enhance the computational efficiency of the procedure. Design results for both unstiffened and stiffened plates are presented.